



**MONASH** University

# Correlation between Photophysical and Structural-Properties in Guanidinium-Iodide Treated Perovskite Solar Cells

Mostafa Rabie Shlaly Bahr Othman

B. Engineering (Honours)

A thesis submitted for the degree of Master at Monash University in 2021.

Department of Materials Science and Engineering

## **Copyright notice**

© Mostafa Othman (2021)

I certify that I have made all reasonable efforts to secure copyright permissions for third-party content included in this thesis and have not knowingly added copyright content to my work without the owner's permission.

## Abstract

The use of guanidinium iodide (GAI) additive has been widely employed as an interface engineering technique. It is thought to passivate surface defects and grain boundaries to improve both device performance and stability. Despite the significant advancements reported so far via GAI-treated perovskite solar cells (PSCs), there still exists a lack of understanding of the relationships between structural and photophysical properties. Herein, we investigate the impact of employing a GAI surface treatment on the triple-cation  $\text{Cs}_{0.07}\text{FA}_{0.79}\text{MA}_{0.14}\text{Pb}(\text{I}_{0.83}\text{Br}_{0.17})_3$  (CsMAFA) perovskite formulation. A detailed X-ray diffraction (XRD) analysis suggests that GAI reacts with the CsMAFA perovskite lattice forming mixed GAFA phases. By tuning the content of GAI, we demonstrate a PSC with superior optoelectronic properties and performance. Furthermore, confocal photoluminescence (PL) imaging for the optimized GAI concentration shows the homogenization of the luminescence intensities and resolving the micro-scale PL heterogeneities for CsMAFA perovskite. We also find that high concentrations of GAI are detrimental to PSC performance. The results show that controlling the concentration of surface treatment agents is important for the homogenization of perovskite optoelectronic properties and hence eliminating performance losses and instabilities.

**Declaration**

This thesis is an original work of my research and contains no material which has been accepted for the award of any other degree or diploma at any university or equivalent institution and that, to the best of my knowledge and belief, this thesis contains no material previously published or written by another person, except where due reference is made in the text of the thesis.

Signature:

Print Name: MOSTAFA OTHMAN

Date:

## Acknowledgements

First and foremost, I would like to express my deepest gratitude to my supervisor Prof. Joanne Etheridge for giving me the opportunity to work on such a challenging topic; perovskite solar cells and more importantly, for being amazingly supportive mentor during my time at Monash. Jo's inexhaustible enthusiasm for science has given me the motivation and courage to persevere through this incredible journey. Her neat approach to research and ability to identify the important problems and solutions sparked the passion and devotion needed to finish this project. At the same time, Jo was always there to answer my questions, give me advice and support me in different aspects of life. I thank Jo as well for her crucial role in helping me to successfully get a Marie Skłodowska-Curie fellowship to start my PhD studies at EPFL. I couldn't hope for a better mentor and I am eternally indebted to her. Also, I would like to thank Prof. Udo Bach for being involved in my research project and I am very grateful for all his valuable inputs and discussions in our group meetings.

I am sincerely thankful to Dr. Tian Zhang and Dr. David McMeekin for being great friends and co-supervisors. They offered me insightful scientific feedback and contributions during the course of my study. We had exciting discussions on countless scientific and less scientific topics. I also thank them for painstakingly proofreading my manuscript.

I would like to thank Dr. Sebastian Fürer for being a great friend personally and a mentor professionally. I have learned a lot about the chemistry side of solar cells from Seb, not to mention, he is just simply an optimistic and cheerful person to spend time with. I also would like to thank Dr. Rebecca Milhuisen for teaching me spectroscopic techniques, her pancakes and sense of humour.

I would like to thank all the past and present renewable energy lab members for creating a dynamic environment and our everlasting friendships.

Further, I would like to thank all the members of Monash centre for Electron Microscopy specifically Dr. Xi-Ya Fang and Dr. Zhou (Ben) Xu for the scanning electron microscopy training which had been essential in conducting the research presented in this thesis. I would like to thank Dr. Weilun Li for all his valuable time to help with the structural data analysis. I wish to thank Prof. Laure Bourgeois for her criticism and review of my work during my confirmation. I owe special thanks to Catherine Brown for her excellent administrative support and timely help on many occasions.

I would like to thank Prof. Nadia Rafaat from Cairo university and my past colleagues at Schneider Electric who introduced me to the world of research and development, materials science and solar cells. This early exposure aroused my curiosity for years to come, which ultimately led me to the world of perovskite solar cells.

I would like to thank my MIT supervisor Prof. Lindley Winslow for supervising my first research project and her recommendations. Her sheer excitement for science has been a constant source of inspiration.

I would like to thank Dr. Michael Goodwin and Dr. Jessica Zheng from the Australian Astronomical Observatory, who gave me hands-on sophisticated software packages and taught me how to write scientific reports during my undergrad internship. I learned a lot about science and inter-personal relations from Michael and Jessica.

Further, I would like to thank the Flexible Electronics Lab members at CSIRO, specifically Dr. Dechan Angmo for being a great mentor and friend. Special thanks to Dechan for always keeping up my spirits high whenever needed. I wish to thank her for all our interesting discussions during our roll-to-roll experiments, coffee breaks and lunch times. Thank you to the team leader Dr. Mei Gao for her unwavering support and help during my time at CSIRO.

I would like to thank my family for all the love and support even when separated by oceans and continents. The support you have given me has been absolutely tremendous for all my studies, in many ways.

Finally, I would like to thank the Australian government for financially supporting my academic journey so far twice; first was during my undergraduate internship at the Australian Astronomical Observatory and second, during my master's study at Monash university. This research was supported by an Australian Government Research Training Program (RTP) Scholarship

## **Table of Contents**

<b>Abbreviations .....</b>	<b>XIV</b>
<b>1. Motivation and Aim .....</b>	<b>1</b>
<b>2. Introduction .....</b>	<b>3</b>
2.1. Perovskite crystal for photovoltaics .....	3
2.2. Perovskite Solar Cell Device Architectures.....	4
2.3. Working Principles of Perovskite Solar Cells .....	5
2.4. Measuring Device Performance in Perovskite Solar Cells .....	6
2.5. Ionic Motion and J-V Hysteresis in Perovskite Solar Cells.....	7
2.6. Structure-Property Relationships in Photoactive Perovskites using Electron Microscopy ....	8
2.7. Assessment of the perovskite radiative quality using confocal photoluminescence (PL)....	9
<b>3. Literature review.....</b>	<b>11</b>
3.1. Crystal Structure of 2D Perovskites.....	11
3.2. Optoelectronic Properties of 2D Perovskites .....	12
3.3. 2D/3D Perovskite Solar Cells .....	13
3.4. Suppressed ion migration in low dimensional Perovskites.....	26
<b>4. Research aims .....</b>	<b>35</b>
<b>5. Methodology .....</b>	<b>36</b>
5.1. Device and materials fabrication methods.....	36
5.2. Device characterizations .....	37
5.2.1 Current-Voltage (J-V) Characteristics .....	37
5.2.2 Ultra-violet visible (UV-Vis) spectra.....	37
5.2.3 Steady-state photoluminescence (PL) and time-resolved PL measurements .....	37
5.2.4 Contact Angle measurements .....	38
5.2.5 X-ray diffraction analysis (XRD) .....	38
5.2.6 Scanning electron microscopy (SEM) micrographs .....	38
5.2.7 Confocal PL spectroscopy and imaging measurements.....	38
<b>6. Results and Discussion .....</b>	<b>39</b>
6.1. Structural analysis of the GAI-treated PSCs .....	39
6.2. The impact of GAI treatment on the photophysical properties of the perovskite films.....	44
6.3. Opto-electronic and morphological characterization of the perovskite films .....	46
6.4. Resulting device performance of the GAI-treated PSCs.....	48
6.5. The detrimental effect of excess GAI on the device performance .....	51
6.6. Hydrophobic nature of the perovskite films .....	51
<b>7. Conclusion and Future Outlook.....</b>	<b>53</b>

<b>8. References .....</b>	<b>54</b>
----------------------------	-----------



## **Table of Figures**

<b>Figure 1.</b> Historic correlation between global temperatures and CO <sub>2</sub> levels. (Figure from ref. <sup>5</sup> ) .....	1
<b>Figure 2.</b> Crystal structure of the cubic perovskite compound with the general formula ABX <sub>3</sub> . (The representation of the structure is adapted from <a href="https://chemicalstructure.net">https://chemicalstructure.net</a> ) .....	3
<b>Figure 3.</b> The famous NREL chart showing the most-updated power conversion efficiencies of perovskite solar cells. (The picture adapted from <a href="https://www.nrel.gov/pv/cell-efficiency.html">https://www.nrel.gov/pv/cell-efficiency.html</a> ).....	4
<b>Figure 4.</b> a) Cross-section SEM image and b) Schematic diagram of a PSC on a ‘planar’ architecture and a mesoporous scaffold. Adapted with permission from ref. <sup>37</sup> . Copyright © 2016 American Chemical Society.....	5
<b>Figure 5.</b> Typical JV curve of a working solar cell device under illumination. ....	6
<b>Figure 6.</b> Current density-voltage curves of a PSC showing hysteretic behavior between the forward scan (from J <sub>sc</sub> to V <sub>oc</sub> ) and reverse scan (from V <sub>oc</sub> to J <sub>sc</sub> ) directions. Reprinted with permission from ref. <sup>42</sup> . Copyright © 2014 American Chemical Society....	7
<b>Figure 7.</b> Overview of the different types of signals generated by an impinging high energy electron beam. Electrons are marked with solid arrows and photons are marked with dashed arrows. Reprinted with permission from reference <sup>44</sup> . Copyright © 2017 WILEY-YCH Verlag GmbH & Co. KGaA, Weinheim. ....	9
<b>Figure 8.</b> Basic setup of the confocal PL imaging. (The picture is adapted from <a href="https://www.laser2000.co.uk/applications/confocal-microscopy">https://www.laser2000.co.uk/applications/confocal-microscopy</a> ).....	10
<b>Figure 9.</b> a) Crystal structures of typical 2-dimensional organic-inorganic perovskites for n=1. b) Band alignment diagram of a 2-dimensional perovskite material possessing multiple quantum wells. Reprinted with permission from ref. <sup>48</sup> . Copyright © 2018 WILEY-VCH Verlag GmbH & Co. KGaA, Weinheim.....	11
<b>Figure 10.</b> Tolerance factor of APbI <sub>3</sub> as a function of the A cation. Tolerance factors between 0.8 and 1.0 (dotted lines) allow for the photoactive black phase (solid circles) to be formed, whilst tolerance factors outside this region results in the formation of non-photoactive phases (open circles) that are not ideal for solar cell applications. Adapted with permission from ref. <sup>51</sup> . Copyright © 2017, American Association for the Advancement of Science. ....	12
<b>Figure 11.</b> Illustration of the 2D crystal structure, mixed-dimensional 2D/3D perovskites, and 3D perovskites. Adapted with permission from ref. <sup>58</sup> . Copyright © 2016 WILEY-VCH Verlag GmbH & Co. KGaA Weinheim. ....	13

**Figure 12.** Chemical structures of various reported ammonium cations used for the formation of 2D/3D perovskite films in solar cells. Reprinted with permission from ref.<sup>48</sup>. Copyright © 2018 WILEY-VCH Verlag GmbH & Co. KGaA, Weinheim..... 14

**Figure 13.** a) Structure of the 2D/3D Perovskite,  $(\text{PEA})_2(\text{MA})_2[\text{Pb}_3\text{I}_{10}]$  and 3D Perovskite,  $\text{MAPbI}_3$ . Reproduced with permission.<sup>59</sup> Copyright 2014, Wiley-VCH. b) Unit cell structure of  $(\text{PEA})_2(\text{MA})_{n-1}\text{Pb}_{n+1}\text{I}_{3n+1}$  Perovskites and the corresponding PCEs. Reproduced with permission.<sup>60</sup> Copyright © 2016, American Chemical Society..... 14

**Figure 14.** a) Crystal structures and corresponding XRD patterns of thin films versus bulk materials of  $\text{BA}_2\text{PbI}_4$  and  $\text{MAPbI}_3$  perovskites. b) XRD patterns of thin films versus bulk materials of  $(\text{BA})_2(\text{MA})\text{Pb}_2\text{I}_7$ ,  $(\text{BA})_2(\text{MA})_2\text{Pb}_3\text{I}_{10}$ , and  $(\text{BA})_2(\text{MA})_3\text{Pb}_4\text{I}_{13}$  perovskites in their preferred crystal growth orientation. Reprinted with permission from ref.<sup>61</sup>. Copyright © 2015, American Chemical society. .... 16

**Figure 15.** a) Schematic of the MP treatment method with FAI and iBAI. b) Current density-voltage curves of the non-treated and MP-treated PSCs measured under AM1.5G irradiation. Statistical distributions of c) PCE, d)  $V_{\text{OC}}$ , e)  $J_{\text{SC}}$ , and f) FF of PSCs with the various MP passivation compositions. Adapted with permission from ref.<sup>63</sup>. Copyright © 2018 WILEY-VCH Verlag GmbH & Co. KGaA, Weinheim. .... 17

**Figure 16.** a) Current density-voltage curves of champion devices for MP50 based and reference cells measured at a scan speed of 140 mV/sec under AM1.5G irradiation (inset: stabilized PCEs). b) Hysteresis analysis of MP50 and reference PSCs at different scan speeds. c) PCEs measured under 75% RH condition over 38 days. Adapted with permission from ref.<sup>63</sup>. Copyright © 2018 WILEY-VCH Verlag GmbH & Co. KGaA, Weinheim. .... 18

**Figure 17.** Average CPD values as a function of bias voltage applied to the tip for MP50 treated and reference samples measured under dark conditions. Spatial CPD maps of the b) reference and c) MP50-treated samples. Adapted with permission from ref.<sup>63</sup>. Copyright © 2018 WILEY-VCH Verlag GmbH & Co. KGaA, Weinheim..... 18

**Figure 18.** a) Current density-voltage curves for champion  $\text{FAPbI}_3(\text{AVAI})_x$  PSCs under AM1.5G irradiation. b) IPCE and integrated  $J_{\text{SC}}$  of  $\alpha\text{-FAPbI}_3$  and  $\text{FAPbI}_3(\text{AVAI})_{0.25}$  PSCs. Reprinted with permission from ref.<sup>64</sup>. Copyright 2019, American Chemical Society. ... 19

**Figure 19.** Normalized PCE of optimized devices retaining 90% of the initial efficiency after 300 h of continuous white light exposure at maximum power point under AM1.5G irradiation. Reprinted with permission from ref.<sup>64</sup>. Copyright 2019, American Chemical Society. .... 19

**Figure 20.** a-f) SEM images of post-annealed  $\text{BA}_x(\text{FA}_{0.83}\text{Cs}_{0.17})_{1-x}\text{Pb}(\text{I}_{0.6}\text{Br}_{0.4})_3$  perovskite films with different BA content concentrations (insets: 2D-XRD images of respective films, where reflections at  $q_z \approx 1$  and  $2 \text{ \AA}^{-1}$  are assigned to the 3D perovskite (100) and (200),

respectively. White arrows highlight diffraction peaks arising for low BA contents, and red arrows highlight diffraction peaks arising for high BA contents. Enlarged SEM images of g)  $x = 0.03$ , h)  $x = 0.09$  and i)  $x = 0.16$  films. Adapted with permission from ref.<sup>65</sup> Copyright © 2017, Nature Publishing Group. .... 20

**Figure 21.** a) Current density-voltage curves for PSCs using the wide-bandgap  $\text{FA}_{0.83}\text{Cs}_{0.17}\text{Pb}(\text{I}_{0.6}\text{Br}_{0.4})_3$  ( $x = 0$ ) and  $\text{BA}_{0.09}(\text{FA}_{0.83}\text{Cs}_{0.17})_{0.91}\text{Pb}(\text{I}_{0.6}\text{Br}_{0.4})_3$  ( $x = 0.09$ ) perovskite active layers under AM1.5G irradiation. b) Stabilized power output of champion cells at the maximum power point for 60 s. c) Current density-voltage curve of the champion PSC using a low-bandgap  $\text{BA}_{0.05}(\text{FA}_{0.83}\text{Cs}_{0.17})_{0.95}\text{Pb}(\text{I}_{0.8}\text{Br}_{0.2})_3$  perovskite active layer under AM1.5G irradiation (inset: corresponding stabilized power output). d) PCE histogram of  $\text{BA}_{0.05}(\text{FA}_{0.83}\text{Cs}_{0.17})_{0.95}\text{Pb}(\text{I}_{0.8}\text{Br}_{0.2})_3$  PSCs. Adapted with permission from ref.<sup>65</sup> Copyright © 2017, Nature Publishing Group. .... 21

**Figure 22.** Stability curves of a) – e) non-encapsulated and f) – j) encapsulated PSCs using  $\text{FA}_{0.83}\text{Cs}_{0.17}\text{Pb}(\text{I}_{0.6}\text{Br}_{0.4})_3$  (navy blue lines; pristine) and  $\text{BA}_{0.09}(\text{FA}_{0.83}\text{Cs}_{0.17})_{0.91}\text{Pb}(\text{I}_{0.6}\text{Br}_{0.4})_3$  (red lines; BA/FA/Cs) perovskite layers aged under AM1.5G 76 mW/cm<sup>2</sup> and 45 RH% at open-circuit. An exponential decay over the first ~100 h is followed by an approximate linear decay. a), f), b) and g) are normalized and averaged over eight devices, whilst c), h), d), i), e) and j) are shown for champion devices. Adapted with permission from ref.<sup>65</sup> Copyright © 2017, Nature Publishing Group..... 22

**Figure 23.** Current density-voltage curves of HTM-free a) PSC and b) a 10 x 10 cm<sup>2</sup> solar module employing 2D/3D perovskite with 3%AVAI measured under AM1.5G irradiation (inset: device statistics and picture of devices). c) Stability test of module under AM 1.5 G conditions at 55 °C and short circuit conditions (inset: photovoltaic parameters of the PSC and solar module represented in a) and b). Reproduced under the terms of the CC-BY license<sup>66</sup>. Copyright 2017, The authors, published by Nature communications..... 23

**Figure 24.** a) Device architecture of spiro-OMeTAD-free and spiro-OMeTAD-containing PSCs. b) Current density-voltage curve of spiro-OMeTAD-containing PSC employing a 2D/3D perovskite with 3%  $\text{HOOC}(\text{CH}_2)_4\text{NH}_3\text{I}$  measured under AM1.5G irradiation (inset: device statistics and photo of PSC). c) Stability curves of the spiro-OMeTAD-containing PSC compared with the spiro-OMeTAD-free mixed 2D/3D PSC at maximum power point under AM 1.5G illumination measured in an inert Ar atmosphere at 45 °C (inset: champion device parameters). Reproduced under the terms of the CC-BY license<sup>66</sup>. Copyright 2017, The authors, published by Nature communications. .... 23

**Figure 25.** a) Device architecture of PSCs incorporating Gua cations. b) Statistical data box plots of  $J_{\text{sc}}$ ,  $V_{\text{oc}}$ , FF and PCEs (obtained across 17 cells per condition) of PSCs prepared with  $\text{MA}_{1-x}\text{Gua}_x\text{PbI}_3$  as a function of  $x$ . c) IPCE spectra of  $\text{MA}_{1-x}\text{Gua}_x\text{PbI}_3$  for  $x = 0.14$ , 0.17 and 0.25,  $\text{MAPbI}_3$  (0%) and those incorporating 50% Gua, all measured under AM1.5G irradiation. Reproduced under the terms of the CC-BY license<sup>67</sup>. Copyright 2017, The authors, published by Nature Energy. .... 24

**Figure 26.** a) Current density-voltage curve measured under AM1.5G irradiation and b) EQE spectrum of the champion cell prepared with mixed MA/Gua perovskite containing 14% Gua. c) Maximum power point tracking under 1 Sun AM1.5G illumination measured in air for PSC containing  $\text{MA}_{1-x}\text{Gua}_x\text{PbI}_3$  ( $x = 0.14$ ). d) normalized PCE of  $\text{MA}_{1-x}\text{Gua}_x\text{PbI}_3$  PSCs ( $x = 0, 0.125, 0.15, 0.25$ ) at 60 °C under continuous light illumination and maximum power point tracking in an inert Ar atmosphere. Reproduced under the terms of the CC-BY license<sup>67</sup>. Copyright 2017, The authors, published by Nature Energy. .... 25

**Figure 27.** a) Schematic of the temperature-dependent electrical conductivity measurements showing b)  $\text{MAPbI}_3$  and c)  $(\text{BA})_2(\text{MA})_3\text{PbI}_{13}$  perovskite films. Reprinted with permission from ref.<sup>70</sup> Copyright © 2017 American Chemical Society. .... 26

**Figure 28.** a) Schematic of iodine ion migration throughout the 3D perovskite device compared to suppressed migration in the 2.5D perovskite device. b)  $\text{Au}_2\text{I}^-$  – depth profile comparison between fresh and 60 h aged 3D PSCs. c)  $\text{Au}_2\text{I}^-$  – depth profile comparison between fresh and 60 h aged 2.5D PSCs. Reprinted with permission from ref.<sup>71</sup> Copyright © 2019 American Chemical Society ..... 27

**Figure 29.** a) Device architecture of B-ACI and LDRP PSCs. Current-density voltage curves of B-ACI and LDRP PSCs with b)  $(\text{BEA})_{0.5}\text{MA}_3\text{PbI}_{10}$  and  $(\text{BA})_2\text{MA}_2\text{PbI}_{10}$  photoactive layers and c)  $(\text{BEA})_{0.5}\text{Cs}_{0.15}(\text{FA}_{0.83}\text{MA}_{0.17})_{2.85}\text{PbI}_3(\text{I}_{0.83}\text{Br}_{0.17})_{10}$  and  $(\text{BA})_2\text{Cs}_{0.1}(\text{FA}_{0.83}\text{MA}_{0.17})_{1.9}\text{PbI}_3(\text{I}_{0.83}\text{Br}_{0.17})_{10}$  photoactive layers, measured under AM1.5G irradiation. Normalized PCE decay of B-ACI and LDRP PSCs under d) ambient atmospheric conditions, e) constant illumination in the glove-box, f) constant temperature of 85 °C, and g) 85% relative humidity in a humidity chamber. Reprinted with permission from ref.<sup>72</sup> Copyright © 2019 WILEY-YCH Verlag GmbH & Co. KGaA, Weinheim..... 28

**Figure 30.** a) Schematic of mesoscopic PSC architecture. Current density-voltage curves of b) BA ( $n = 4$ ) and Gly ( $n = 4, 6$ , and 8) under reverse scan directions and c) BA ( $n = 4$ ) and Gly ( $n = 4$ ) PSCs under reverse and forward scan directions measured under AM1.5G irradiation. d) Steady-state measurement of the PCE at the maximum power point, e) IPCE spectra, f) PCE distributions, g)  $V_{oc}$  h)  $J_{sc}$ , and i) FF distributions of BA ( $n = 4$ ) and Gly ( $n = 4$ ) PSCs. Adapted with permission from ref.<sup>73</sup> Copyright © 2020 WILEY-YCH Verlag GmbH & Co. KGaA, Weinheim ..... 29

**Figure 31.** a) Schematic of PSC architecture employing an LDP capping layer. b) Current density-voltage curves and c) IPCE spectra of unmodified and LDP-modified PSCs measured under AM1.5G irradiation. Current-density voltage curves of devices employing d) BBA, e) CBA and f) FBA LDP capping layers, and g) compiled PCE histograms fitted with gaussian distributions. h) Box plots showing statistical variation of the  $V_{oc}$  across 30 devices. Stabilized i) photocurrent density and j) PCE at maximum power point over time of each unmodified or LDP-modified PSC. Adapted with permission from ref.<sup>74</sup>. Copyright © 2020 Elsevier Ltd. All rights reserved. .... 30

**Figure 32.** a) Normalized PCE variation of unsealed PSCs exposed to 45 ± 5% RH and measured under AM1.5G irradiation. b) Water contact angles measurements of pristine 3D perovskite film and those modified by FBAI, CBAI and BBAI. c) XRD patterns of 3D and BBA-based perovskite films before and after aging in 45±5% RH. Normalized PCE variation of unsealed PSCs when exposed to the relative humidity of d) 15 ± 5% RH and e) 75 ± 5% RH. f) Normalized PCE variation of unsealed PSCs when exposed to 85 °C. UV–vis absorption spectra of g) 3D and h) BBA-based films before and after aging at 85 °C. Adapted with permission from ref.<sup>74</sup>. Copyright © 2020 Elsevier Ltd. All rights reserved. .... 31

**Figure 33.** a) Current density-voltage curves measured under AM1.5G irradiation and b) IPCE spectra of the optimized devices based on (PEA)<sub>2</sub>MA<sub>4</sub>Pb<sub>5</sub>l<sub>16</sub> and (4FPEA)<sub>2</sub>(MA)<sub>4</sub>Pb<sub>5</sub>l<sub>16</sub> perovskites. c) Stabilized photocurrent output of the champion (4FPEA)<sub>2</sub>(MA)<sub>4</sub>Pb<sub>5</sub>l<sub>16</sub> device and d) PCE histograms fitted with gaussian distributions. Reprinted with permission from ref.<sup>75</sup>. Copyright © 2019 WILEY-YCH Verlag GmbH & Co. KGaA, Weinheim. .... 32

**Figure 34.** a) X-ray diffraction patterns of (PEA)<sub>2</sub>MA<sub>4</sub>Pb<sub>5</sub>l<sub>16</sub> and (4FPEA)<sub>2</sub>MA<sub>4</sub>Pb<sub>5</sub>l<sub>16</sub> films. b) Schematic illustration of the (111) and (202) orientations of (4FPEA)<sub>2</sub>MA<sub>4</sub>Pb<sub>5</sub>l<sub>16</sub> perovskite crystal. 2D GIWAXs of c) (PEA)<sub>2</sub>MA<sub>4</sub>Pb<sub>5</sub>l<sub>16</sub> and d) (4FPEA)<sub>2</sub>(MA)<sub>4</sub>Pb<sub>5</sub>l<sub>16</sub>. e) Polar angle spectrum at the peak of (002). Reprinted with permission from ref.<sup>75</sup>. Copyright © 2019 WILEY-YCH Verlag GmbH & Co. KGaA, Weinheim. .... 33

**Figure 35.** a) Stability tests of unsealed devices based on (PEA)<sub>2</sub>MA<sub>4</sub>Pb<sub>5</sub>l<sub>16</sub> and (4FPEA)<sub>2</sub>MA<sub>4</sub>Pb<sub>5</sub>l<sub>16</sub> stored under air atmosphere with a humidity of 60 ± 5% (inset: contact angle measurements). b) XRD patterns of perovskite films stored in air over 60 days. c) Thermal stability of devices upon 55 °C annealing under an inert N<sub>2</sub> atmosphere. Reprinted with permission from ref.<sup>75</sup>. Copyright © 2019 WILEY-YCH Verlag GmbH & Co. KGaA, Weinheim. .... 33

**Figure 36.** a) Schematic diagram of the perovskite film fabrication, b) XRD patterns for the CsMAFA and GAI-treated films, c) XRD spectra for the different FAPbI<sub>3</sub> and GA<sub>2</sub>PbI<sub>4</sub> compositions, d) XRD spectra for Pb-halides, e) XRD spectra for GAPb(I<sub>x</sub>Br<sub>100-x</sub>)<sub>3</sub> and f) FWHM of the 001 perovskite peak at 14.1°. .... 41

**Figure 37.** Zoomed-in XRD patterns for the 001 and 002 perovskite peaks. .... 44

**Figure 38.** Confocal PL mapping for the reference and GAI-10 films marked with Au fiducial markers as shown in the corresponding SEM images: a & b) Fluorescence and SEM micrograph of the CsMAFA film, d & e) Fluorescence and SEM micrograph of the GAI-10 film c & f) Normalized PL spectra for the films before and after each fluorescence mapping. The laser excitation wavelength is 488 nm and the emission range is between 510 to 900 nm. .... 45

<b>Figure 39.</b> Time-dependent confocal PL spectra of the perovskite films: a) CsMAFA and b) GAI-10. The arrow highlights the rise of a segregated PL peak for the CsMAFA film. ....	46
<b>Figure 40.</b> Characterization of the perovskite films: a) UV-Vis absorption (the arrow highlights the reduced absorption intensity for higher GAI concentrations), b) Steady-state PL spectra, c) TRPL decay curves of the perovskite films. ....	47
<b>Figure 41.</b> SEM micrographs of the perovskite films: a) CsMAFA, b) CsMAFA/IPA, c) GAI-2, d) GAI-10, e) GAI-20, f) GAI-30 and g) GAI-40. ....	48
<b>Figure 42.</b> a) Schematic illustration of the employed planar device architecture, b) Hysteresis indices as a function of GAI concentrations, Statistical distribution of photovoltaic parameters: b) $V_{OC}$ , c) $J_{SC}$ , d) FF, and e) PCE for the devices made with CsMAFA perovskite and those modified with GAI. ....	49
<b>Figure 43.</b> J-V curves at a scan rate of 0.1 V/s for all the devices featuring the hysteresis behavior: a) CsMAFA, b) GAI-2, c) GAI-10, d) GAI-20, e) GAI-30 and f) GAI-40. ....	50
<b>Figure 44.</b> Cross-sectional SEM images for the fully assembled devices based on CsMAFA and GAI-treated films: a) CsMAFA, b) GAI-2, c) GAI-10, d) GAI-20, e) GAI-30 and f) GAI-40. ....	50
<b>Figure 45.</b> Photovoltaic properties of the resulting IPA washed devices: a) $V_{OC}$ , b) $J_{SC}$ , c) FF, and d) PCE. ....	51
<b>Figure 46.</b> Contact-angle measurements for the different perovskite films: a) CsMAFA, b) GAI-2, c) GAI-10, d) GAI-20, e) GAI-30 and f) GAI-40. ....	52

## Abbreviations

<b>4-FPEA</b>	4-fluoro-phenylethyl ammonium
<b>Å</b>	Angstrom
<b>A</b>	Ampere
<b>Ar</b>	Argon
<b>Au</b>	Gold
<b>AVAI</b>	Ammonium valeric acid iodide
<b>AzPbI<sub>3</sub></b>	Azetidinium lead iodide
<b>BA</b>	Butylammonium
<b>BEA</b>	1,4-butanediamine
<b>BSEs</b>	Back scattered electrons
<b>ACN</b>	Acetonitrile
<b>CB</b>	Conduction band
<b>CBZ</b>	Chlorobenzene
<b>CH(NH<sub>2</sub>)<sub>2</sub><sup>+</sup></b>	Formamidinium
<b>CH<sub>3</sub>NH<sub>3</sub><sup>+</sup></b>	Methylammonium
<b>CH<sub>3</sub>NH<sub>3</sub>PbI<sub>3</sub></b>	Methylammonium lead tri-iodide
<b>CH<sub>6</sub>IN<sub>3</sub></b>	Guanidinium iodide compound
<b>CsI</b>	Cesium iodide
<b>DMF</b>	N,N-dimethylformamide
<b>DMSO</b>	Dimethyl sulfoxide
<b>DSSCs</b>	Dye-sensitized solar cells
<b>EM</b>	Electron microscope
<b>ETL</b>	Electron transport layer
<b>FAI</b>	Formamidinium iodide
<b>FF</b>	Fill factor
<b>FTO</b>	Fluorine-doped tin oxide
<b>FWHM</b>	Full-width at half maximum
<b>GAI</b>	Guanidinium iodide

<b>HI</b>	Hysteresis index
<b>HOOCCH<sub>2</sub>NH<sub>3</sub><sup>+</sup></b>	Glycine cation
<b>HTL</b>	Hole transport layer
<b>HTM</b>	Hole transport material
<b>IPA</b>	Iso-propanol
<b>IPCE</b>	Incident-photon-to-current-efficiency
<b>ITO</b>	Indium-doped tin oxide
<b>J<sub>mpp</sub></b>	Short-circuit current density at maximum power point
<b>J<sub>sc</sub></b>	Short-circuit current density
<b>J-V</b>	Current-voltage
<b>KPFM</b>	Kelvin-probe force microscopy
<b>MABr</b>	Methylammonium bromide
<b>MQW</b>	Multiple-quantum well
<b>—NH<sub>2</sub></b>	Amino group
<b>NMAI</b>	1-naphthylammonium iodide
<b>OIHPs</b>	Organic-inorganic hybrid perovskites
<b>PbBr<sub>2</sub></b>	Lead bromide
<b>PbI<sub>2</sub></b>	Lead iodide
<b>PCE</b>	Power conversion efficiency
<b>PEA</b>	Phenylethyl ammonium
<b>P<sub>in</sub></b>	Incident (radiant) power
<b>PL</b>	Photoluminescence
<b>PLQY</b>	Photoluminescence quantum yield
<b>P<sub>max</sub></b>	Maximum power
<b>PSCs</b>	Perovskite solar cells
<b>RH</b>	Relative-humidity
<b>SEM</b>	Scanning electron microscope
<b>SEs</b>	Secondary electrons
<b>TEM</b>	Transmission electron microscope
<b>TF</b>	Tolerance factor



<b>TLD</b>	Through-lens detector
<b>TOF-SIMs</b>	Time-of-flight secondary ion-mass spectroscopy
<b>TRPL</b>	Time-resolved photoluminescence
<b>UV</b>	Ultra-violet
<b>UV-vis</b>	Ultraviolet-visible
<b>V</b>	Voltage
<b>V<sub>mpp</sub></b>	Open-circuit voltage at maximum power point
<b>V<sub>oc</sub></b>	Open-circuit voltage
<b>XRD</b>	X-ray diffraction
<b>η</b>	Power conversion efficiency

## 1. Motivation and Aim

One of the most pressing challenges facing humanity in the 21<sup>st</sup> century is to stop global warming, which can otherwise lead to far-reaching and catastrophic environmental consequences. Global warming is caused by burning of fossil fuels that release greenhouse gasses (mainly CO<sub>2</sub>, N<sub>2</sub>O and NH<sub>4</sub>) into the atmosphere, which trap the sun's heat reflected by the Earth's surface.<sup>1</sup> As a result, global Earth's temperatures are continuing to increase at an unprecedented pace leading to the rise of sea levels, melting ice poles, dying coral reefs and huge storms that destroy cities.<sup>1,2</sup> Nowadays, it is generally accepted within the scientific community that CO<sub>2</sub> is the main greenhouse gas which is most responsible for global warming.<sup>3</sup> Furthermore, there has been a strong correlation between global temperatures and atmospheric CO<sub>2</sub> emissions (**Figure 1**).<sup>4</sup>

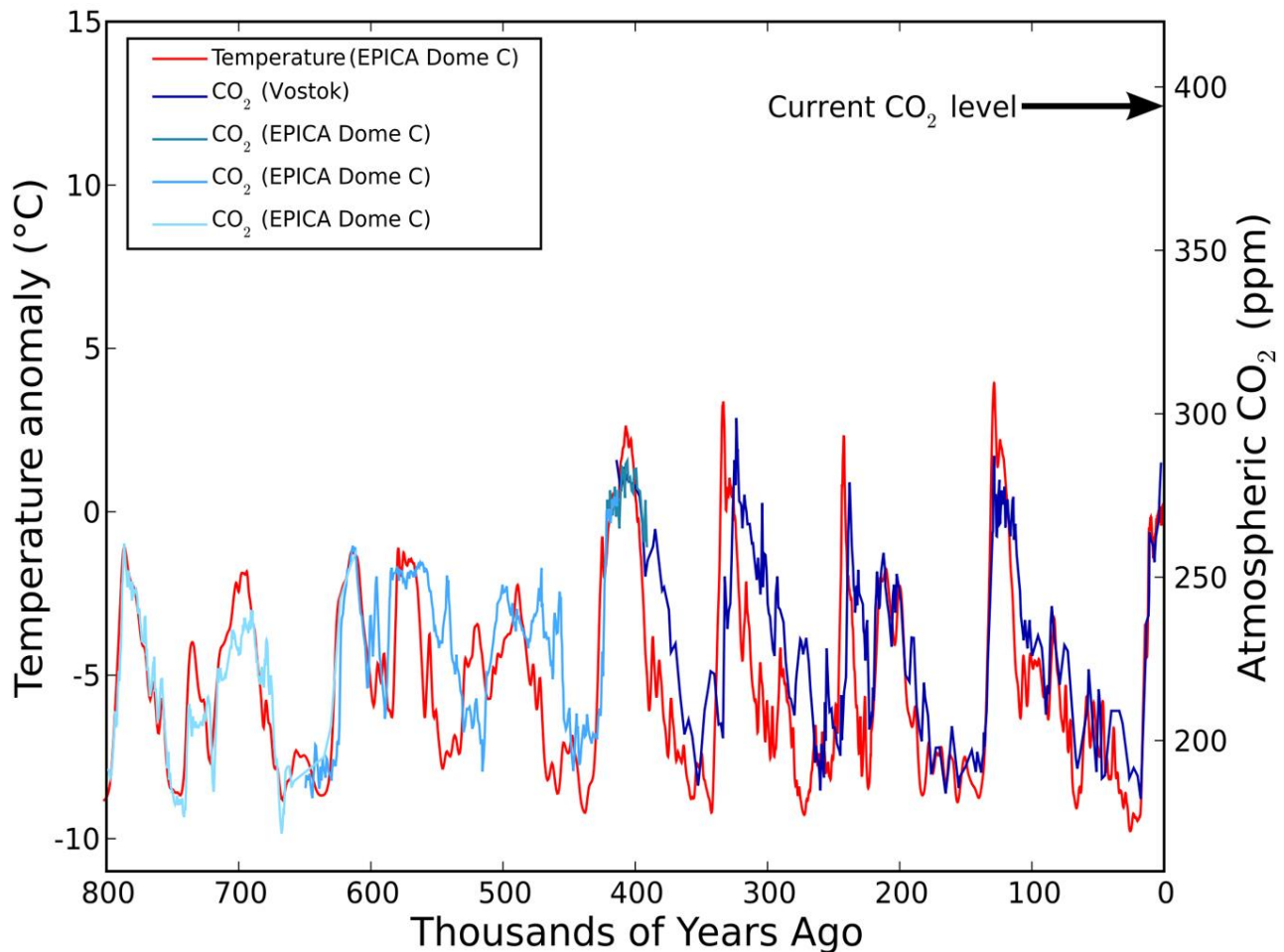


**Figure 1.** Historic correlation between global temperatures and CO<sub>2</sub> levels. (Figure from ref.<sup>5</sup>)

Consequently, the transition towards clean and cheap renewable energy resources has become paramount for society to continue its energy consumption unhindered. Solar

energy is considered the most abundant renewable energy resource as an alternative to fossil fuels for energy generation.<sup>6,7</sup> Photovoltaic devices are the most promising candidates to convert solar irradiation into electricity by directly converting photons to electrical power. Thin film materials specifically organic-inorganic hybrid perovskites (OIHPs) are very attractive class of materials for photoactive layers in solar cells. These materials are abundant, cheap to produce, low-temperature processed and they have strong light absorption, tunable band-gap and some tolerance to defects.<sup>8–13</sup> These unique set of favorable properties have helped to bring the solar cell power conversion efficiency (PCE) on a lab-scale up to 25.5% for single-junction solar cells, rivalling most of the established photovoltaic technologies in just over a decade.<sup>14</sup> However, for any solar cell technology to be commercialized, long-term operational stability has to be addressed alongside high PCE. Perovskite films suffer from intrinsic degradation factors when subjected to ultra-violet (UV) light<sup>15</sup>, reverse electrical bias<sup>16</sup>, oxygen<sup>17</sup>, moisture<sup>18</sup> and high temperatures ( $\geq 80$  °C).<sup>19,20</sup> This poses serious questions as to whether perovskite solar cells can achieve the stabilities that make them suitable for mass production especially for solar panels, where the standard lifetime of 25 – 30 years is required to make an inexpensive module worth the cost of installation, maintenance and replacement.

The aim of the work described in this thesis is to improve the performance of PSCs through a post-treatment passivation strategy. I applied guanidinium iodide (GAI) as a surface treatment on top of the triple-cation perovskite  $\text{Cs}_{0.07}\text{FA}_{0.79}\text{MA}_{0.14}\text{Pb}(\text{I}_{0.83}\text{Br}_{0.17})_3$  at different concentrations. Low-concentrations of GAI treatment resulted in upgrading the device performance, however, high-GAI concentrations led to poor device performance. To understand the possible underpinning reasons for the resulting device performance, x-ray diffraction (XRD), scanning electron microscopy (SEM), steady-state photoluminescence (PL), time-resolved PL and confocal PL studies were conducted. Finally, it was concluded that managing the structure and composition of surface treatment-agents is vital for achieving optimal device output.

## 2. Introduction

### 2.1. Perovskite crystal for photovoltaics

Organic-inorganic metal halide perovskites solar cells (PSCs) have emerged rapidly as one of the most promising light harvesting photovoltaic layers due to their low-cost, solution processability and exceptional optoelectronic properties such as strong light absorption<sup>9</sup>, long charge carrier diffusion length<sup>21</sup>, high carrier mobility<sup>22</sup> and certain defect-tolerance property.<sup>23–26</sup>

Perovskites are based on the formation of a number of positive and negative ions to make up the basic cubic  $ABX_3$  crystal structure (**Figure 2**).<sup>27</sup> In the case of PSCs, the A-cation can be occupied by organic  $CH_3NH_3^+$  (Methylammonium),  $CH(NH_2)_2^+$  (Formamidinium) or inorganic  $Cs^+$  or  $Rb^+$  cations. The B-site is a divalent metal cation occupied in most cases by  $Pb^{+2}$  or  $Sn^{+2}$ , while the X-site can be occupied by halides such as  $Cl^-$ ,  $I^-$ ,  $Br^-$  or pseudo-halide such as  $SCN^-$ .

The archetypical PSC, methylammonium lead tri-iodide ( $CH_3NH_3PbI_3$ ), has emerged as the primary material of interest, combining direct bandgap characterized by 1.55 eV which corresponds to an absorption onset at the edge of the visible spectrum (800nm).<sup>27</sup> This bandgap lies close to the optimum range (1.1-1.4 eV) for reaching maximum Shockley-Queisser limit efficiency, allowing PSCs to theoretically reach 31% PCE.

Furthermore,  $CH_3NH_3PbI_3$  is characterized by a low trap density and weak exciton binding energy (30 mV), which means that photogenerated carriers can be separated very rapidly at room temperature.<sup>28</sup> Finally, the material shows highly balanced electrons and holes diffusion lengths (0.1- 1  $\mu m$ )<sup>21</sup> and sufficiently high charge carrier mobilities.<sup>22</sup> This means that the charges can be efficiently diffused and collected by the electrodes before recombination. These favourable optoelectronic properties make perovskite materials very attractive for photoactive layers in photovoltaics.

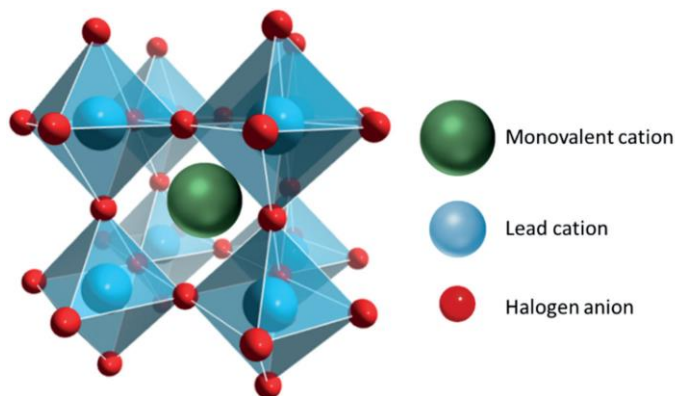


**Figure 2.** Crystal structure of the cubic perovskite compound with the general formula  $ABX_3$ . (The representation of the structure is adapted from <https://chemicalstructure.net>)

## 2.2. Perovskite Solar Cell Device Architectures

The early representations of PSCs were based on a dye-sensitized solar cells (DSSCs) architecture using  $\text{CH}_3\text{NH}_3\text{PbI}_3$  as a sensitizer on thick mesoporous  $\text{TiO}_2$  scaffolds.<sup>29</sup> This architecture yielded a low PCE of 3.8% back in 2009 since it was coupled with liquid electrolyte.<sup>12</sup> Later, it was realized that perovskites can efficiently extract electrons and holes alike making it a promising semiconductor material for solar cells.<sup>30</sup> The breakthrough came when a solid state architecture based on Spiro-OMeTAD as a hole transport material (HTM) was realized achieving 9% PCE in 2012.<sup>31</sup> From there on, PSCs experienced impressive development reaching 25.5% as of now for single-junction solar cells, rivalling most established photovoltaic technologies (**Figure 3**).<sup>14</sup>

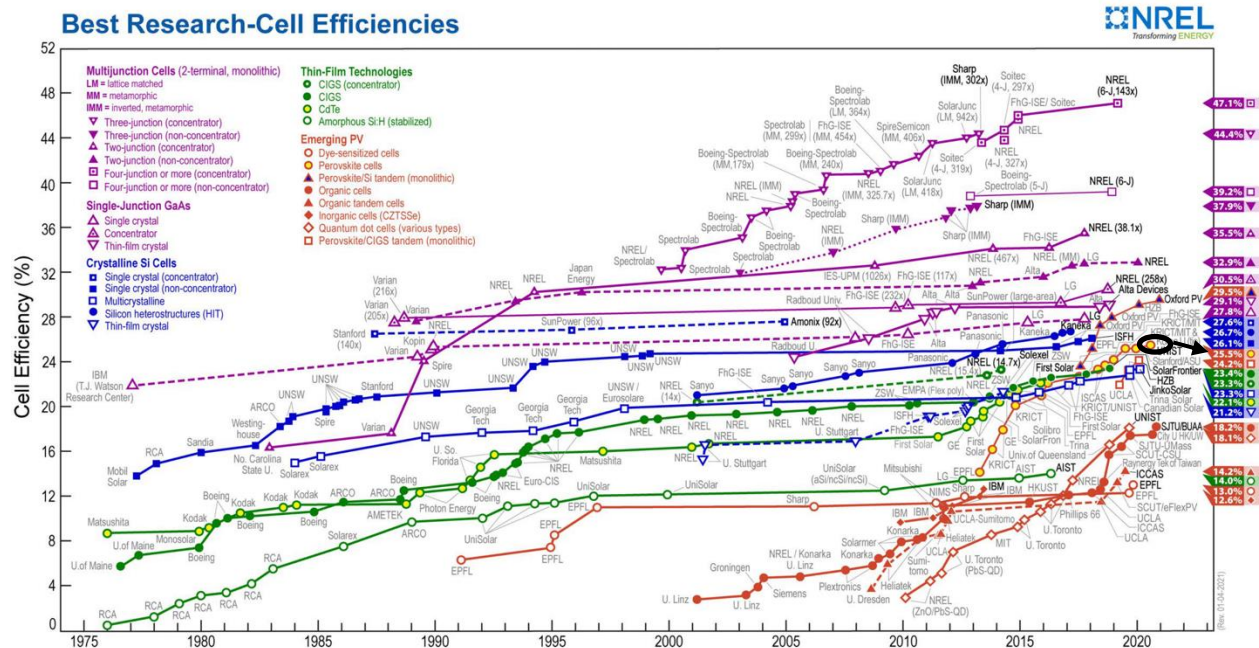


**Figure 3.** The famous NREL chart showing the most-updated power conversion efficiencies of perovskite solar cells. (The picture adapted from <https://www.nrel.gov/pv/cell-efficiency.html>).

PSCs are usually between 500 nm to 1  $\mu\text{m}$  thick and are sandwiched between hole and electron charge transport layers (ETL and HTL respectively). The perovskite solar cell architecture could involve either n-i-p “planar” or p-i-n “inverted” type structure, where the perovskite acts as an intrinsic semiconductor. PSCs are typically placed between a metal electrode (Ag, Au and  $\text{MoO}_x$ ) and a transparent one such as ITO or FTO (Indium or Fluorine doped-tin oxide).

A mesoporous scaffold is often deposited on top of the ETL to improve charge extraction and interface energetics (energy level alignments). However, planar devices have been established with performance close to that of their scaffold-based counterparts (**Figure 4**).<sup>32,33</sup> Up till now, planar architectures outperform inverted ones due to the large open-

circuit voltage ( $V_{oc}$ ) losses in the latter.<sup>34,35</sup> However, ‘inverted’ architectures began to achieve high efficiency with enhanced  $V_{oc}$  due to the incorporation of 2D large bulky organic cations on top of the 3D perovskite film which act as a passivation layer for surface defects and grain boundaries.<sup>36</sup>

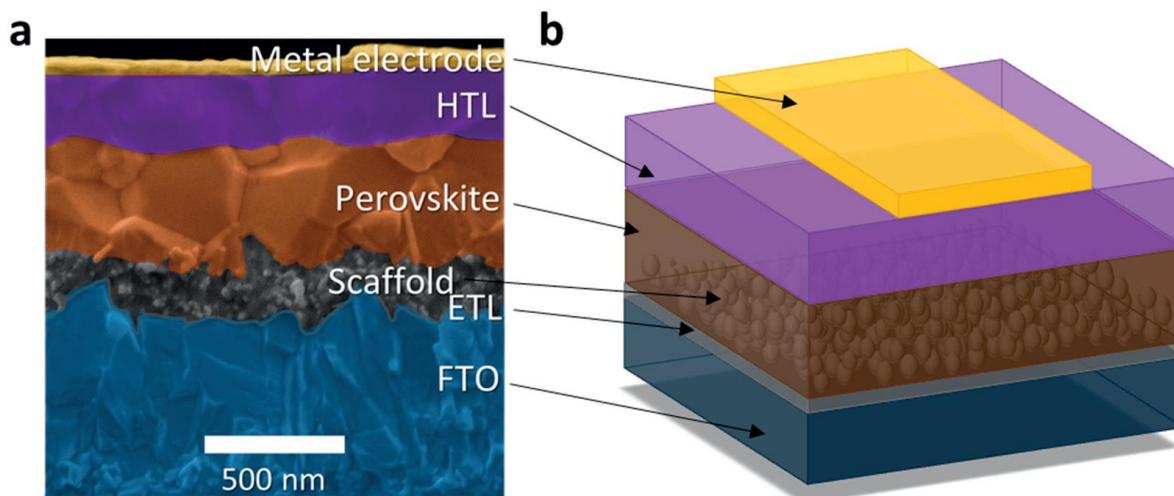


**Figure 4.** a) Cross-section SEM image and b) Schematic diagram of a PSC on a ‘planar’ architecture and a mesoporous scaffold. Adapted with permission from ref.<sup>37</sup>. Copyright © 2016 American Chemical Society.

### 2.3. Working Principles of Perovskite Solar Cells

Perovskites perform in a similar manner to traditional semiconductors such as Si and CdTe. Once the light illuminates the FTO side of the PSC, the incident photons excite the perovskite material generating electron-hole pairs. Due to the low exciton binding energy, charges dissociate readily and are free to move across the device. The electrons separated from the holes are injected into the conduction band (CB) of the ETL, before migrating to the anode. Meanwhile, photogenerated holes are transferred to the HTL and then, are collected at the cathode (metal electrode).

Charge recombination occurs in the bulk, interfaces, and grain boundaries of the perovskite absorber layer.<sup>38–40</sup> This results in non-radiative losses which reduce the device performance and should be impeded. On the other hand, photogenerated carriers can recombine radiatively leading to re-emission of a photon in the so-called process ‘radiative recombination’. A solar cell, where radiative recombination is dominant, usually has high photoluminescence quantum yield (PLQY).<sup>41</sup> The latter property is essential for the highest photovoltaic device performances at the Shockley-Queisser limit, in which all non-radiative recombination is eliminated.



## 2.4. Measuring Device Performance in Perovskite Solar Cells

One of the most important characterization tools for solar cells is the current-voltage (J-V) measurement, which provides the ability to assess the PCE, as illustrated in **Figure 5**. The J-V measurements are performed under standard 1-sun intensity (1000 W/m<sup>2</sup> at AM1.5G spectrum). The  $V_{OC}$  determined as the measured potential when the current density equals 0 mA/cm<sup>2</sup> at open-circuit condition, while the short-circuit current density ( $J_{SC}$ ) is evaluated by monitoring the current density at short-circuit condition when the voltage equals to 0 V.

Moreover, the maximum power ( $P_{max}$ ) point is the product of the photocurrent and voltage at their maximum values ( $J_{MPP}$  and  $V_{MPP}$ ). The power conversion efficiency ( $\eta$ ) of a device is defined by the ratio of maximum power to the radiant (incident) power ( $P_{in}$ ) as in the following equation (1.1):

$$PCE (\eta) = \frac{P_{max}}{P_{in}} = \frac{J_{SC} V_{OC} FF}{P_{in}} \quad (1.1)$$

The fill factor (FF) is a device parameter used to estimate the deviation of the solar cell from the theoretical maximum power point condition and is defined by equation (1.2) as the ratio of the  $P_{max}$  to the  $J_{SC}$  and  $V_{OC}$  values (**measure of the quality of the solar cell and to evaluate qualitatively the resistive losses in the device**):

$$FF = \frac{P_{max}}{J_{SC} V_{OC}} = \frac{J_{MPP} V_{MPP}}{J_{SC} V_{OC}} \quad (1.2)$$

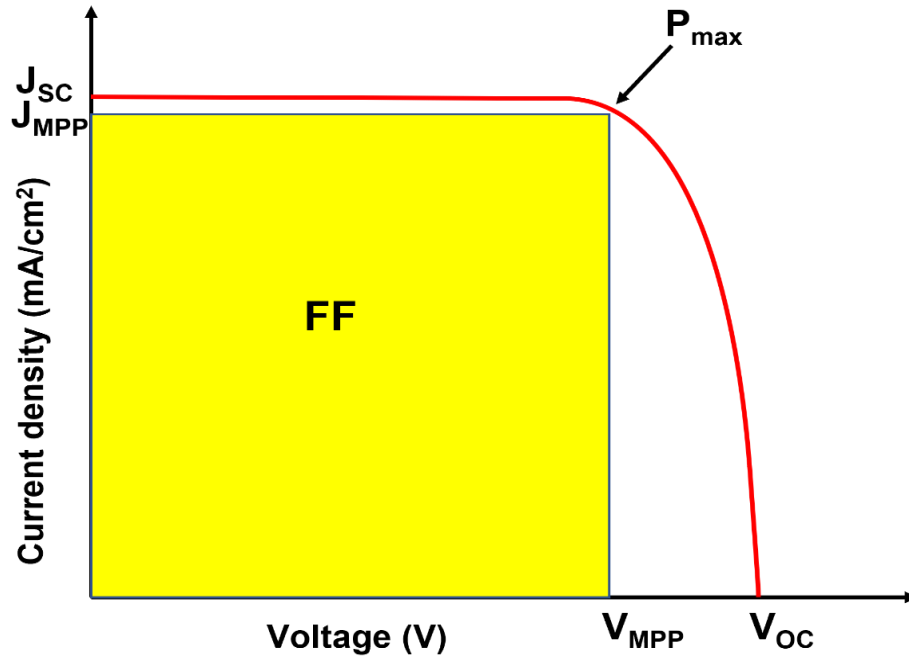


**Figure 5.** Typical JV curve of a working solar cell device under illumination.

## 2.5. Ionic Motion and J-V Hysteresis in Perovskite Solar Cells

Normally, the way of extracting PCE from a solar cell is independent of J-V scan direction as long as the measured device is under quasi-steady state conditions. To fulfil this, the device needs to be under equilibrium during its measurement at each potential. However, this is not always the case for PSCs. In **Figure 6**, Snaith et al. was the first to show that the result of the PCE measurement is different depending on J-V scan direction (open- to short-circuit condition & vice versa).<sup>42</sup> To clarify, differences in the shape of the J-V measurement curves, typically arises from ion-migration in solar cells due to the ionic nature of perovskite materials.<sup>43</sup>

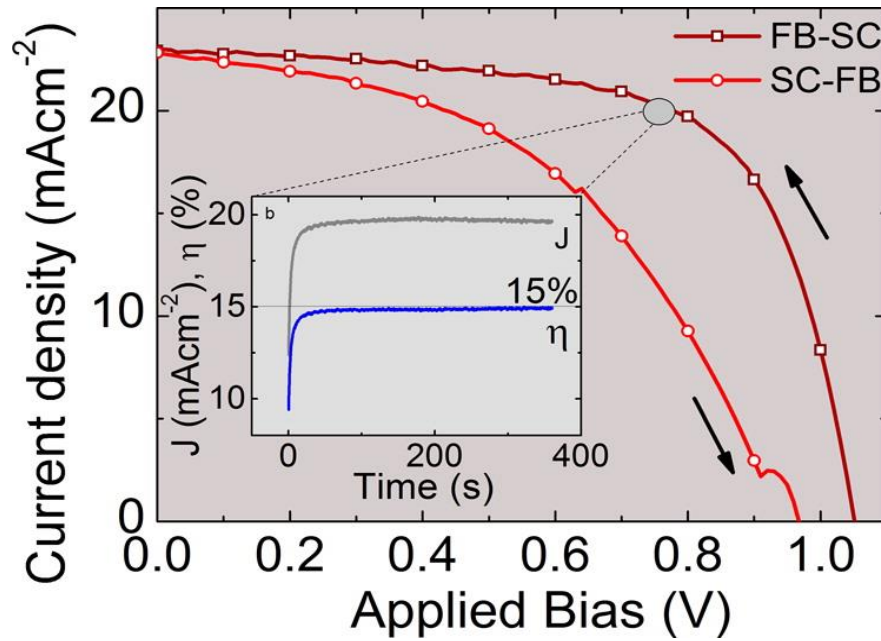


**Figure 6.** Current density-voltage curves of a PSC showing hysteric behavior between the forward scan (from  $J_{sc}$  to  $V_{oc}$ ) and reverse scan (from  $V_{oc}$  to  $J_{sc}$ ) directions. Reprinted with permission from ref.<sup>42</sup>. Copyright © 2014 American Chemical Society.

The term hysteresis index (HI) has been introduced to quantify the J-V discrepancy in perovskite solar cells as defined in equation (1.3) and equation (1.4):

$$HI = \frac{FF_{rev} - FF_{for}}{FF_{rev}} \quad (1.3)$$

$$HI = \frac{PCE_{rev} - PCE_{for}}{PCE_{rev}} \quad (1.4)$$



## 2.6. Structure-Property Relationships in Photoactive Perovskites using Electron Microscopy

Electron Microscopy (EM) is a powerful characterization tool that could be used to probe the microstructure of perovskite films. There are two main types of electron microscopy techniques: scanning electron microscopy (SEM) and transmission electron microscopy (TEM).

Perovskite films are fragile under external stimulus due to weakly bonded organic components. Therefore, they can be very sensitive to electron beams and this can cause damage of the sample if exposed to high electron dose.<sup>44</sup> Low dose operating conditions must be employed in order to obtain data that corresponds to the undamaged structure. Furthermore, appropriate choice of suitable electron microscopy analytical techniques is essential for unveiling the microstructure of perovskite solar cells. SEMs typically operate in an energy range up to 30 kV, whereas TEMs operate between 30 kV and 1500 kV. Furthermore, it is possible to obtain different types of signals to probe structural, chemical and electronic features. SEMs usually probe image surface morphology and sub-surface structures down to 1 nm. TEMs are commonly used on thin specimens typically <100 nm with electron beam energy in the 100–300 kV range, providing information about the internal crystal structures. When the electron beam interacts with the specimen, it produces a wide range of signals from the specimen, some of which are summarized in **Figure 7**. In SEM, the signals most commonly used are “secondary electrons” and ‘backscattered electrons’. The incoming electron beam interacts with the specimen, including the atomic outer-shell electrons to release “secondary electrons” (SEs). SEs images mainly show the surface structure (topography) of the specimen. Higher energy electrons are scattered back throughout the surface and are named backscattered electrons (BSEs). Elements with higher atomic number tend to generate higher intensity signals while elements with lower atomic number display lower intensity signals and this contrast gives some information about the elemental distribution across the film.

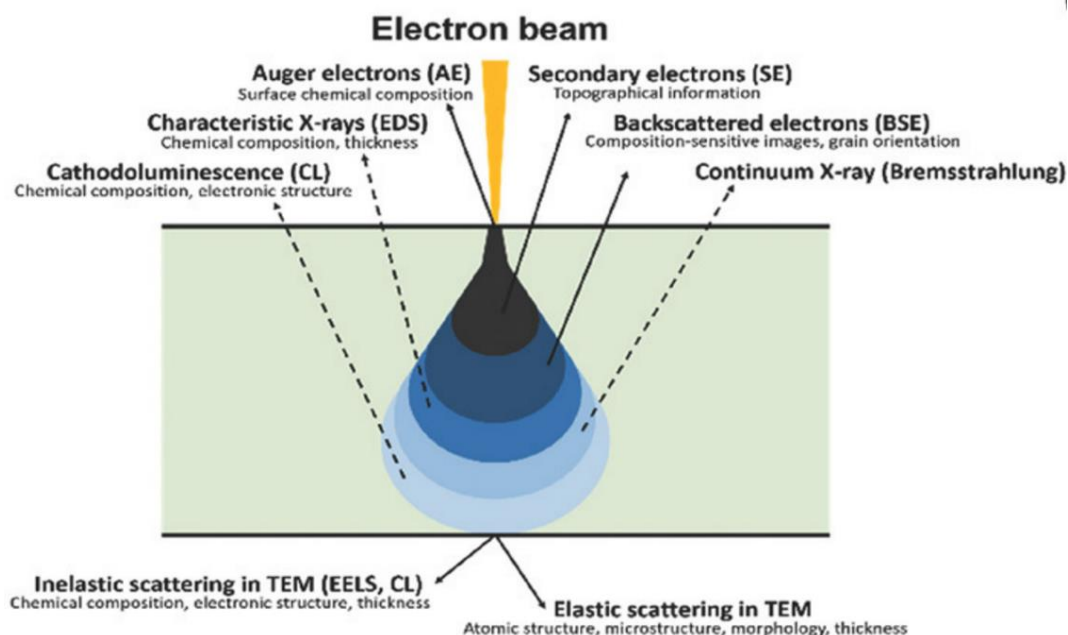


**Figure 7.** Overview of the different types of signals generated by an impinging high energy electron beam. Electrons are marked with solid arrows and photons are marked with dashed arrows. Reprinted with permission from reference<sup>44</sup>. Copyright © 2017 WILEY-YCH Verlag GmbH & Co. KGaA, Weinheim.

## 2.7. Assessment of the perovskite radiative quality using confocal photoluminescence (PL)

Confocal photoluminescence (PL) spectroscopy is a well-established technique for the characterization of semiconductor materials in general and halide perovskite films in particular. It could provide valuable information on the charge carrier recombination kinetics which include radiative and non-radiative recombination, and quantify interface losses in perovskite solar cells. In addition, confocal PL imaging is a powerful technique for mapping microscopic PL inhomogeneities as well as studying indirectly charge carrier dynamics which are relevant for device operation. Confocal PL imaging is achieved by focusing the light beam of a certain excitation wavelength into the plane of interest. A general sketch of the setup is shown in **Figure 8**. The system consists of two pinholes: one is located in front of the laser beam to collimate the incident light path and the other lies in front of the detector (photomultiplier tube) which focuses the reflected light from the sample. The detector is then connected to a computer which reconstructs the image pixel by pixel, one at a time by scanning all over the sample to produce the final image. In this thesis, confocal PL imaging would be used to map the luminescence intensities of the 3D perovskite film and optimized guanidinium iodide surface treatment with the goal of the homogenization of the 3D perovskite luminescence intensity.

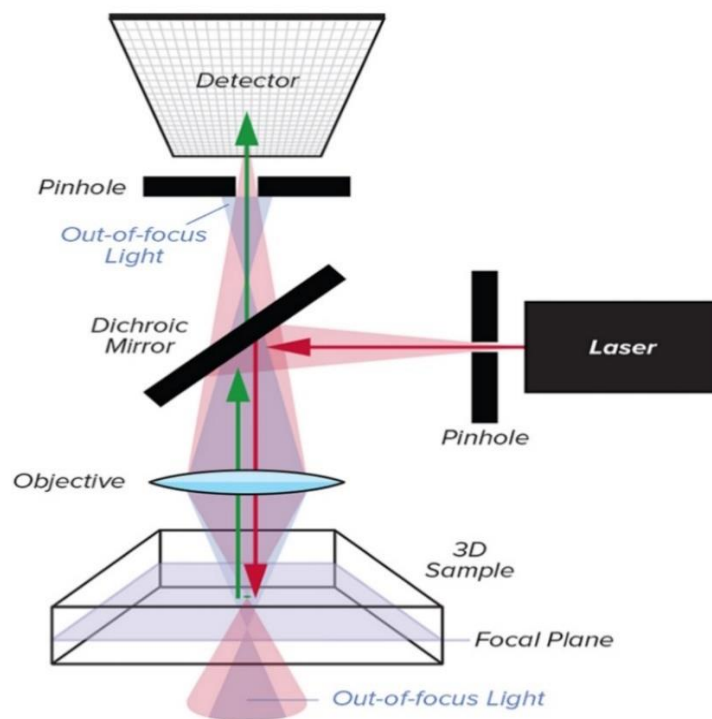


**Figure 8.** Basic setup of the confocal PL imaging. (The picture is adapted from <https://www.laser2000.co.uk/applications/confocal-microscopy>).

### 3. Literature review

#### 3.1. Crystal Structure of 2D Perovskites

So called “2D perovskites” were discovered by Ruddlesden and Popper in 1957 through the compound ‘K<sub>2</sub>NiF<sub>4</sub>’.<sup>45</sup> 2D layered perovskites are formed by incorporating large bulky organic cations which cut the octahedral metallic layers, disrupting the 3D perovskite structure.<sup>46</sup> They usually possess the general formula R<sub>2</sub>A<sub>n-1</sub>B<sub>n</sub>X<sub>3n+1</sub>, where R is a large organic cation which functions as a spacer between the inorganic sheet, and n determines the number of inorganic sheets that are being held together (**Figure 9**).<sup>47</sup>

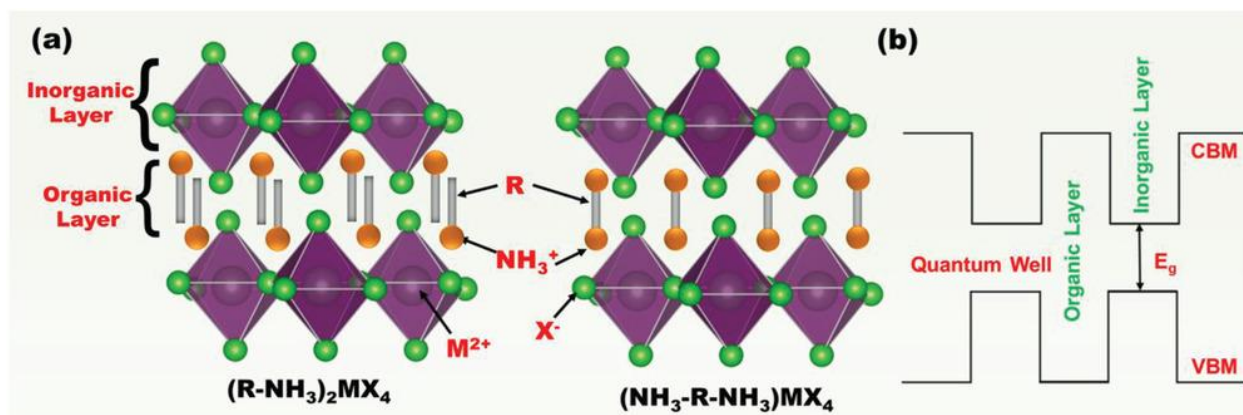


**Figure 9.** a) Crystal structures of typical 2-dimensional organic-inorganic perovskites for n=1. b) Band alignment diagram of a 2-dimensional perovskite material possessing multiple quantum wells. Reprinted with permission from ref.<sup>48</sup>. Copyright © 2018 WILEY-VCH Verlag GmbH & Co. KGaA, Weinheim.

Controlling the A/R ratio, the n value could be adjusted as n=1 (2D), n: from 2 to 5 (quasi-2D) and n > 5 (3D).<sup>49</sup> The 3D to 2D structural transition is controlled by the size of the organic cation, in particular when it exceeds the critical size of Goldschmidt's tolerance factor (TF). Goldschmidt's TF is an empirical formula used to account for the distortion in the perovskite crystal structure and can also provide a guide to predict the transition from 3D to 2D structures (**Figure 10**). The TF depends on the size of the ionic radii of the A, B, and X sites of the perovskite structure as given in equation (1.5):

$$TF = \frac{(R_A + R_X)}{\sqrt{2} (R_B + R_X)} \quad (1.5)$$

where R<sub>A</sub>, R<sub>B</sub>, and R<sub>X</sub> are the ionic radii of the A, B and X atoms. For hybrid halide perovskites, the “ionic” radii must account for metal-halide bonding.<sup>50</sup> Many of the 3D perovskites lie in the range of 0.8 < TF < 1. When the tolerance factor is above 1, it results in crystal structure distortions into face-shared octahedral, leading to the formation of low-dimensional perovskites.

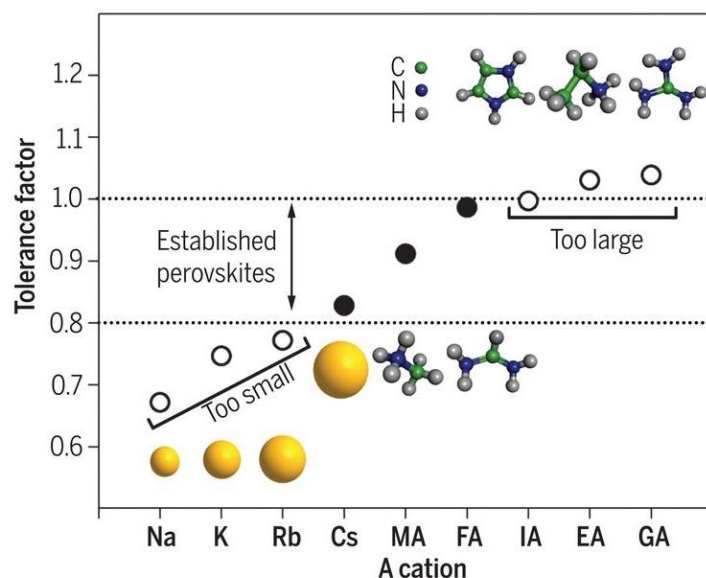


**Figure 10.** Tolerance factor of  $\text{APbI}_3$  as a function of the A cation. Tolerance factors between 0.8 and 1.0 (dotted lines) allow for the photoactive black phase (solid circles) to be formed, whilst tolerance factors outside this region results in the formation of non-photoactive phases (open circles) that are not ideal for solar cell applications. Adapted with permission from ref.<sup>51</sup>. Copyright © 2017, American Association for the Advancement of Science.

When the A-site cation is too large to be well accommodated within the octahedral structure, the 3D perovskite structure becomes energetically unstable, which induces a phase transition toward a layered structure. This phase transition is often termed as ‘2D perovskite’. 2D perovskites exhibit tuneable optical properties and offer improved stability under ambient conditions. They have attracted much interest to overcome stability issues of the 3D counterparts despite their optoelectronic property limitations in terms of larger exciton binding energy, indirect and larger band-gap structures.<sup>52</sup>

### 3.2. Optoelectronic Properties of 2D Perovskites

2D perovskites are composed of organic and inorganic sheets leading to the formation of a layered structure. The specific arrangements of alternating organic-inorganic layers generate a crystallographically ordered 2D multiple-pseudo quantum-well (MQW) electronic structure.

2D perovskites with alternating layers of organic and inorganic layers show appealing properties since the bandgap of the organic material is generally higher than the inorganic counterpart. This leads to the formation of multiple-quantum well structures (**Figure 9b**) which enables them to function in light emission applications.<sup>53–55</sup> Furthermore, organic spacers possess more robust chemical stability compared to 3D counterparts.<sup>56</sup> However,

the higher bandgap of pure 2D perovskites ( $>2.3$  eV) makes them undesirable for photovoltaic applications. One approach to overcome the high bandgap value is to mix the 2D and 3D precursors together (**Figure 11**) or by engineering a layer by layer deposition method to obtain a 2D/3D bilayer structure. Furthermore, when deposited on top of the 3D perovskite, the top 2D perovskite layers can act as a surface passivation layer to reduce the surface charge recombination, ultimately improving the device  $V_{oc}$  and PCE.<sup>57</sup>

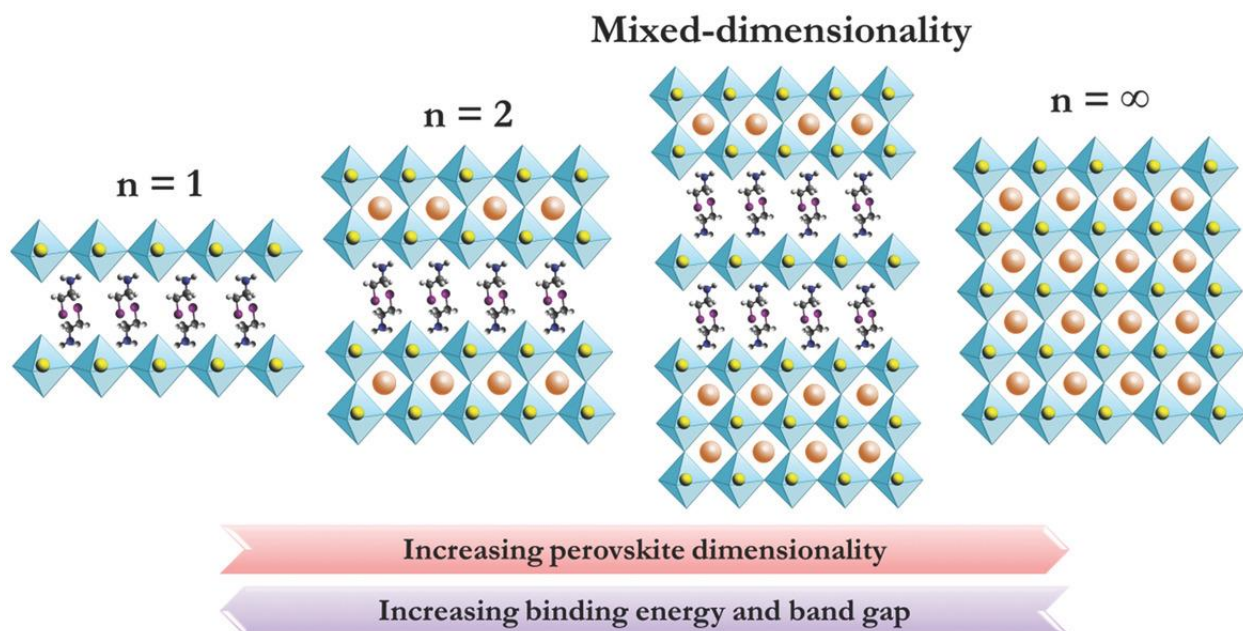


**Figure 11.** Illustration of the 2D crystal structure, mixed-dimensional 2D/3D perovskites, and 3D perovskites. Adapted with permission from ref.<sup>58</sup>. Copyright © 2016 WILEY-VCH Verlag GmbH & Co. KGaA Weinheim.

### 3.3. 2D/3D Perovskite Solar Cells

Thanks to the superior robustness of 2D perovskites, 2D/3D architectures have attracted growing interests as a route towards stable and efficient devices. **Figure 12** shows the chemical structure of the ammonium organic cations that are commonly used at the A-site in 2D Perovskites.<sup>48</sup> In 2014, Smith et al. were the first to introduce a 2D/3D perovskite as an absorber layer for perovskite solar cells.<sup>59</sup> In their work, MA and Phenylethylammonium (PEA) cations were mixed to obtain a Ruddlesden-Popper structure composed of  $(\text{PEA})_2(\text{MA})_2\text{Pb}_3\text{I}_{10}$  for  $n=3$ . It exhibited a wide bandgap of 2.10 eV compared to 1.63 eV for the 3D  $\text{MAPbI}_3$ . The crystal structure of  $(\text{PEA})_2(\text{MA})_2[\text{Pb}_3\text{I}_{10}]$  is shown in **Figure 13a**, where the 3D perovskite is sliced by PEA to form a 2D/3D layered structure. The PSCs were made in a planar architecture using compact  $\text{TiO}_2$  layer and Spiro-OMeTAD as an electron transporting and hole transporting layers, respectively. Gold (Au) was evaporated on top of the HTL as an electrode for the device.



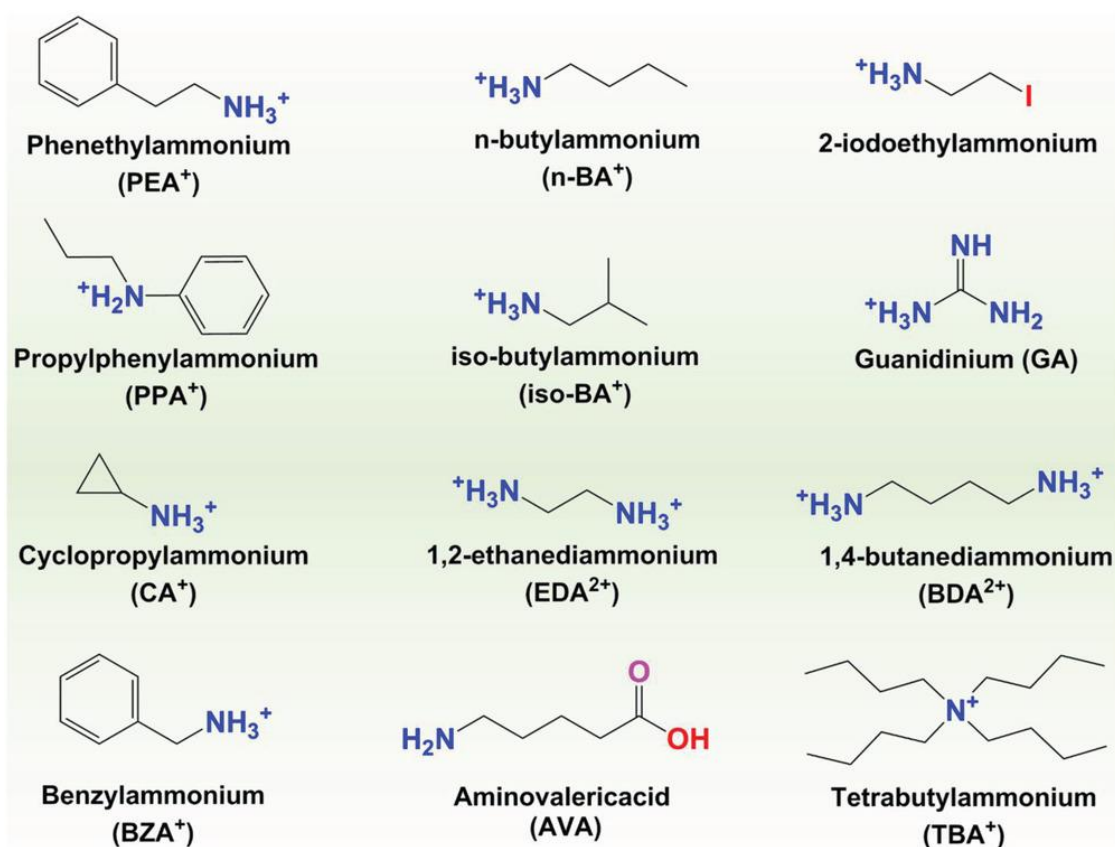


**Figure 12.** Chemical structures of various reported ammonium cations used for the formation of 2D/3D perovskite films in solar cells. Reprinted with permission from ref.<sup>48</sup>. Copyright © 2018 WILEY-VCH Verlag GmbH & Co. KGaA, Weinheim.

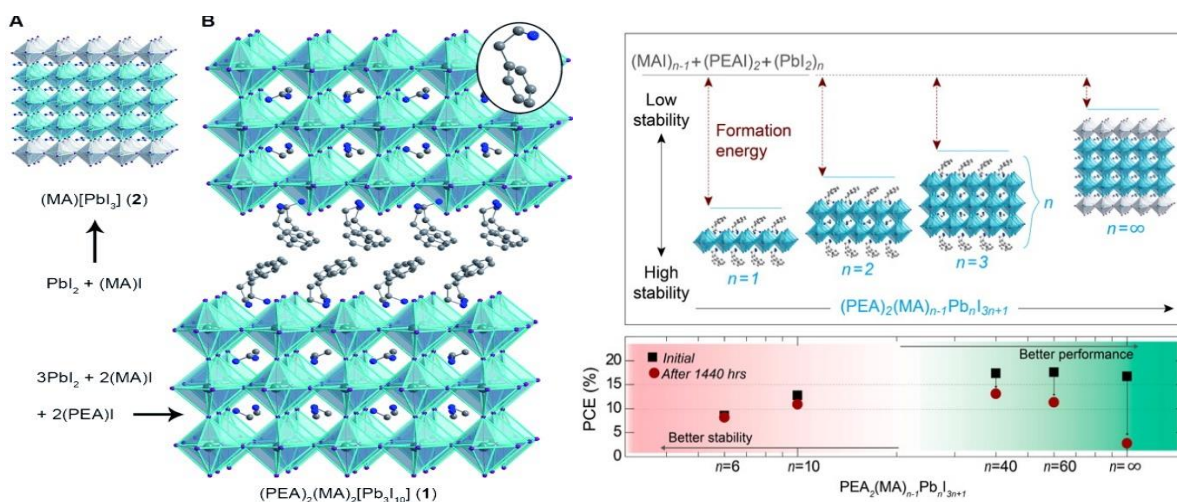


**Figure 13.** a) Structure of the 2D/3D Perovskite, (PEA)<sub>2</sub>(MA)<sub>2</sub>[Pb<sub>3</sub>I<sub>10</sub>] and 3D Perovskite, MAPbI<sub>3</sub>. Reproduced with permission.<sup>59</sup> Copyright 2014, Wiley-VCH. b) Unit cell structure of (PEA)<sub>2</sub>(MA)<sub>n-1</sub>Pb<sub>n</sub>I<sub>3n+1</sub> Perovskites and the corresponding PCEs. Reproduced with permission.<sup>60</sup> Copyright © 2016, American Chemical Society.

The overall PCE was lower,  $\eta = 4.73\%$  under standard AM 1.5G conditions. However, a higher open-circuit voltage of 1.18 V was achieved. In addition, the authors obtained an enhanced stability device, exhibiting stability of over 46 days of air exposure at a humidity level (RH) of 52%. On the other side, MAPbI<sub>3</sub> was damaged, turning from brown to yellow after 46 days under the same conditions.

Furthermore, Quan et al. investigated both PCEs and stability of the higher members (n-layers) of mixed dimensional (PEA)<sub>2</sub>(MA)<sub>n-1</sub>[Pb<sub>n</sub>I<sub>3n+1</sub>] perovskites.<sup>60</sup> PEA-based perovskites with bulkier organic moieties strengthened the Van Der Waals interactions between the inorganic layers. This leads to higher formation energy and enhancement in the stability of the perovskites.

The stability of these perovskite films was studied by X-ray diffraction (XRD) and time-resolved photoluminescence (TRPL) techniques. These experimental techniques demonstrated the improved stability of the quasi-2D perovskites compared to the 3D equivalents and they showed that perovskites with lower n values (i.e., close to 2D) are the most stable (**Figure 13b**). The champion perovskite device was obtained at n=60, which demonstrated a PCE of 15.3% with negligible hysteresis under AM 1.5G conditions. However, these performances fell down to 11.3% PCE after 60 days of storage under low humid atmosphere. This is the first study to suggest a compromise of 'n' value in terms of a high PCE and stable devices, thus opening room for accelerating the optimization of 2D/3D mixed dimensional perovskite and exploration of other types of organic cations to further improve the device performance.

Cao et al. studied the structure and optical properties relationship when they introduced n-butylammonium (BA) cation by the general formula (BA)<sub>2</sub>(MA)<sub>n-1</sub>Pb<sub>n</sub>I<sub>3n+1</sub>, where n= 1,2,3, and 4.<sup>61</sup> They addressed the (001) preferential orientation that corresponds to the denser atomic plane of the 2D perovskite. XRD results of (BA)<sub>2</sub>PbI<sub>4</sub> show clearly the growth direction along the (00l) atomic planes (**Figure 14a**). Another preferential growth along (111) and (202) was obtained that corresponds to the vertical (perpendicular) plane of the substrate and this promotes more the charge transport improving the charge-carrier collection efficiency (**Figure 14b**). They found out that the perpendicular growth exhibits excellent surface coverage leading to the formation of a uniform, dense and well-packed film. Promoting out of plane growth during crystallization enhances the electron collection efficiency and hole transfer dynamics.<sup>62</sup>



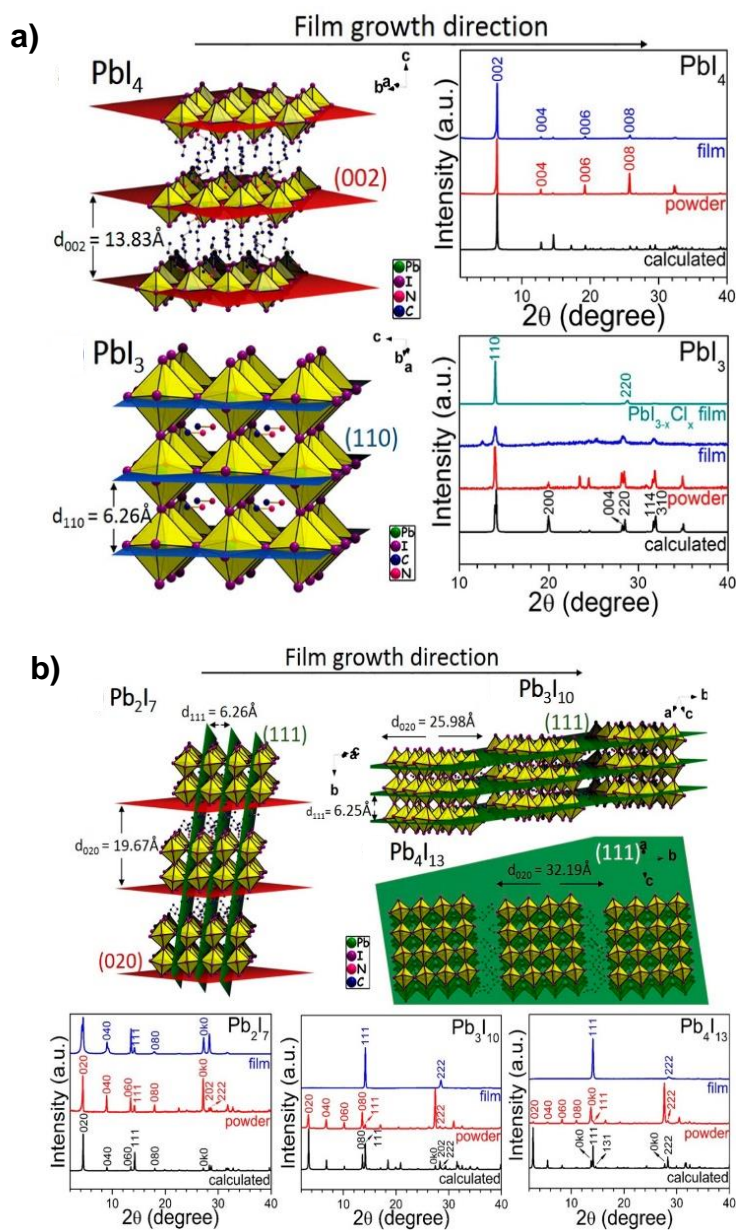


**Figure 14.** a) Crystal structures and corresponding XRD patterns of thin films versus bulk materials of  $\text{BA}_2\text{PbI}_4$  and  $\text{MAPbI}_3$  perovskites. b) XRD patterns of thin films versus bulk materials of  $(\text{BA})_2(\text{MA})\text{Pb}_2\text{I}_7$ ,  $(\text{BA})_2(\text{MA})_2\text{Pb}_3\text{I}_{10}$ , and  $(\text{BA})_2(\text{MA})_3\text{Pb}_4\text{I}_{13}$  perovskites in their preferred crystal growth orientation. Reprinted with permission from ref.<sup>61</sup>. Copyright © 2015, American Chemical society.

Cho et al. reported the use of a mixed passivation (MP) treatment comprising a thin layer of bulky organic ammonium iodide (iso-butylammonium iodide, iBAI) and formamidinium iodide (FAI) between the 3D perovskite and HTL.<sup>63</sup> Using this mixed passivation treatment, the champion mixed-halide PSC (MP50, 50% iBAI and 50% FAI molar ratios)

achieves a stabilized PCE of 21.7% in a reverse scan (**Figure 15**). Without encapsulation, the devices show excellent moisture stability, sustaining over 87% of the original performance after 38 storage days in ambient environment under  $75 \pm 20\%$  relative humidity (**Figure 16**). It was demonstrated by Kelvin probe force microscopy (KPFM), MP treatment of the perovskite/HTL interface significantly suppresses hysteresis by the inactivation of the interfacial trap sites and the formation of an interfacial energetic barrier to reduce ionic transport. This work shows that FAI/iBAI as an efficient and promising passivation treatment for perovskite/selective-contact interfaces (**Figure 17**).

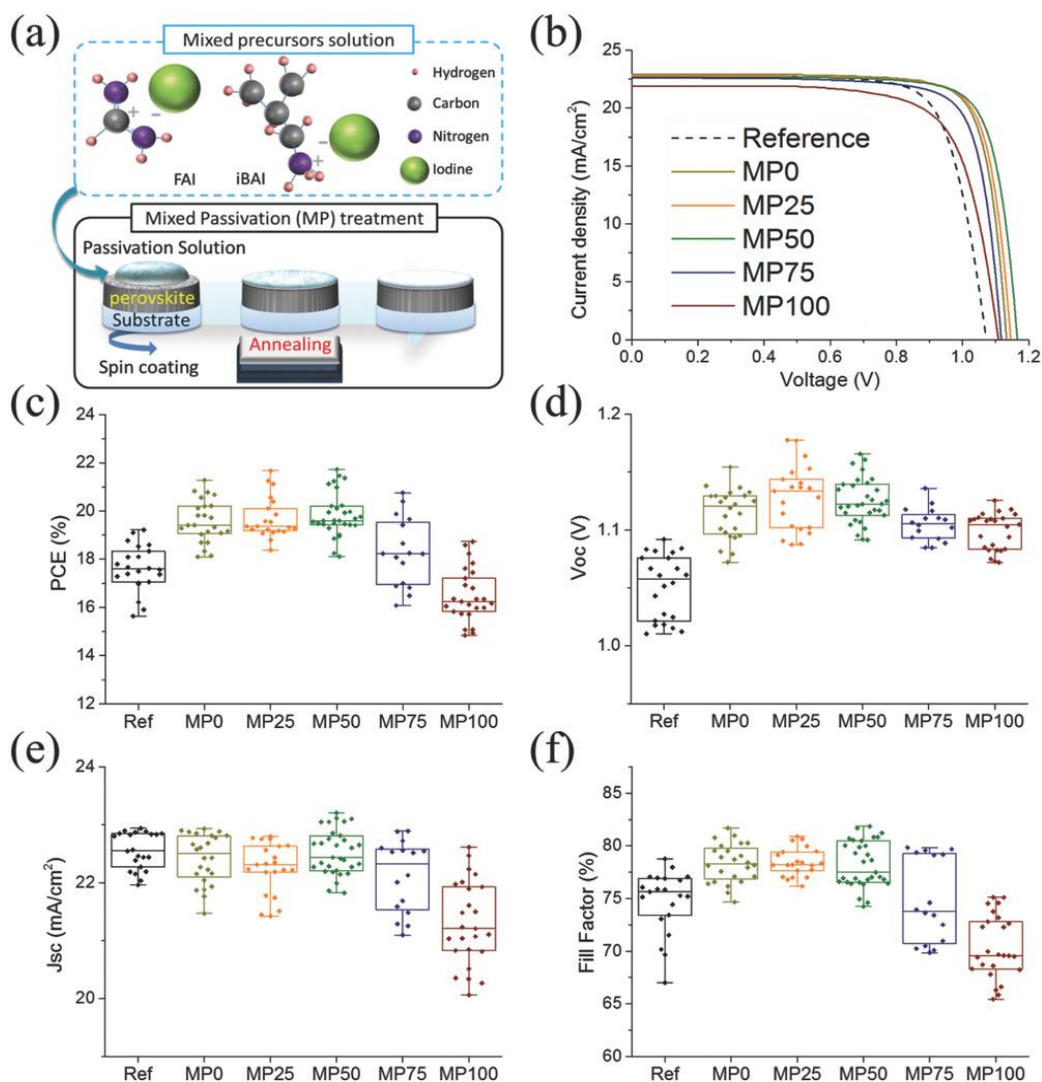


**Figure 15.** a) Schematic of the MP treatment method with FAI and iBAI. b) Current density-voltage curves of the non-treated and MP-treated PSCs measured under AM1.5G irradiation. Statistical distributions of c) PCE, d)  $V_{oc}$ , e)  $J_{sc}$ , and f) FF of PSCs with the various MP passivation compositions. Adapted with permission from ref.<sup>63</sup>. Copyright © 2018 WILEY-VCH Verlag GmbH & Co. KGaA, Weinheim.

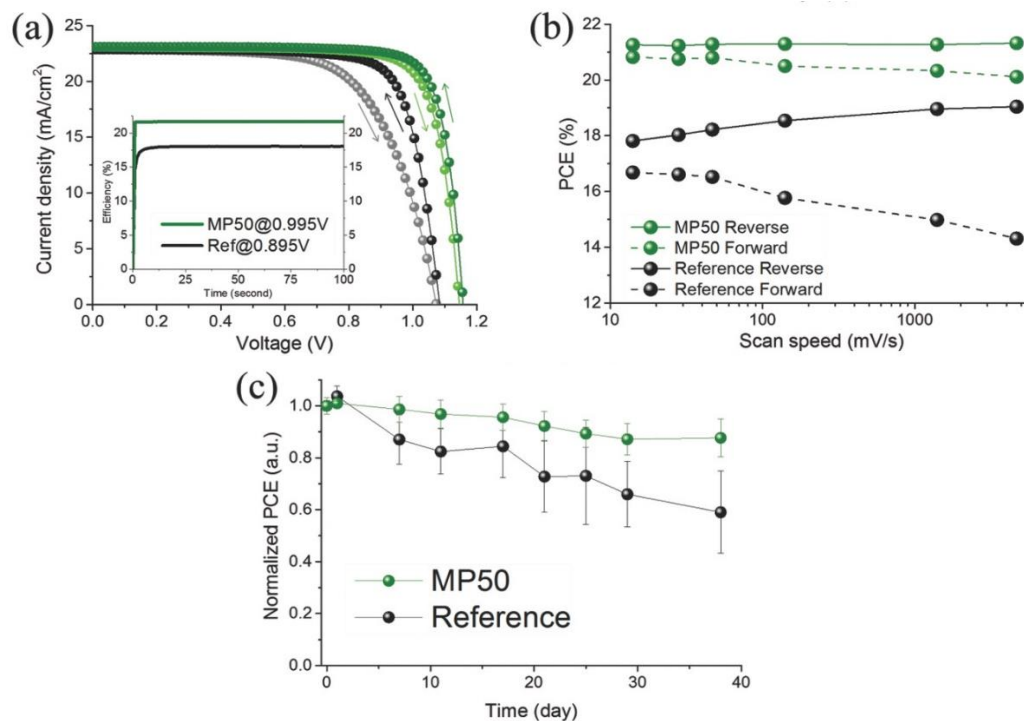


**Figure 16.** a) Current density-voltage curves of champion devices for MP50 based and reference cells measured at a scan speed of 140 mV/sec under AM1.5G irradiation (inset: stabilized PCEs). b) Hysteresis analysis of MP50 and reference PSCs at different scan speeds. c) PCEs measured under 75% RH condition over 38 days. Adapted with permission from ref.<sup>63</sup>. Copyright © 2018 WILEY-VCH Verlag GmbH & Co. KGaA, Weinheim.

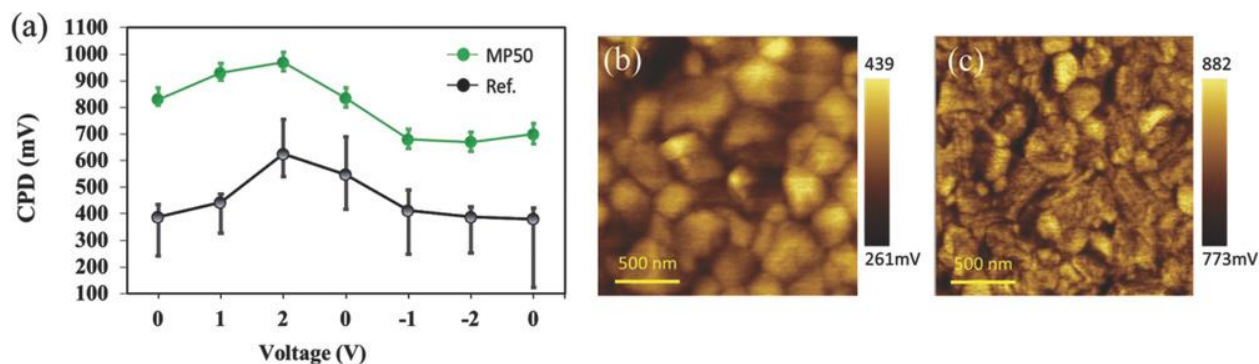


**Figure 17.** Average CPD values as a function of bias voltage applied to the tip for MP50 treated and reference samples measured under dark conditions. Spatial CPD maps of the b) reference and c) MP50-treated samples. Adapted with permission from ref.<sup>63</sup>. Copyright © 2018 WILEY-VCH Verlag GmbH & Co. KGaA, Weinheim.

Alanazi and co-workers reported the use of a large bi-functional bulky organic cation 5-ammonium valeric acid iodide (AVAI) to FAPbI<sub>3</sub> as a 2D/3D perovskite structure to

stabilize FAPbI<sub>3</sub> at room temperature.<sup>64</sup> The optimized AVA-based mesoscopic heterojunction PSC (25% molar ratio) yields a high PCE of 18.94 % (**Figure 18**). The optimized devices retain 90% of the initial efficiency after 300 h under continuous white light illumination at maximum power point conditions (**Figure 19**).

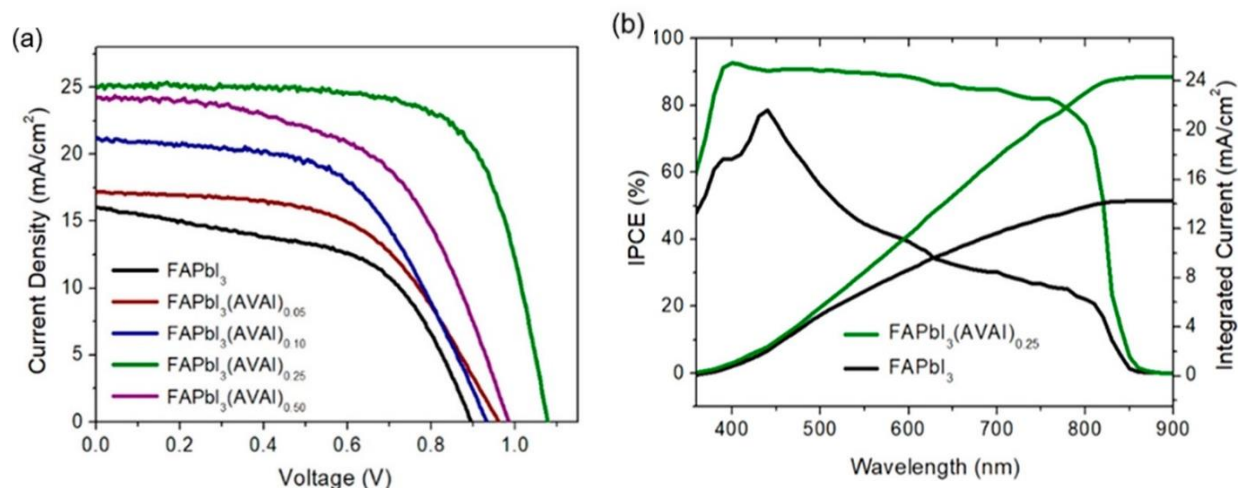


**Figure 18.** a) Current density-voltage curves for champion FAPbI<sub>3</sub>(AVAI)<sub>x</sub> PSCs under AM1.5G irradiation. b) IPCE and integrated J<sub>SC</sub> of α-FAPbI<sub>3</sub> and FAPbI<sub>3</sub>(AVAI)<sub>0.25</sub> PSCs. Reprinted with permission from ref.<sup>64</sup>. Copyright 2019, American Chemical Society.

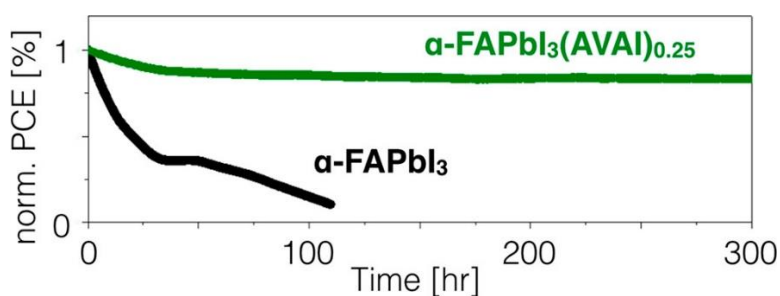


**Figure 19.** Normalized PCE of optimized devices retaining 90% of the initial efficiency after 300 h of continuous white light exposure at maximum power point under AM1.5G irradiation. Reprinted with permission from ref.<sup>64</sup>. Copyright 2019, American Chemical Society.

Wang et al. introduced 2D Ruddlesden-Popper layered n-butylammonium cations into a mixed-cation lead mixed-halide FA<sub>0.83</sub>Cs<sub>0.17</sub>Pb(I<sub>0.6</sub>Br<sub>0.4</sub>)<sub>3</sub> 3D perovskite composition.<sup>65</sup> Using scanning electron microscopy, they observed the formation of 2D perovskite platelets, slicing the highly oriented 3D perovskite structure, which resulted in passivating surface defects and suppressing non-radiative charge carrier recombination (**Figure 20**). Solar cells with an optimal BA content exhibit an average stabilized power conversion efficiency of 17.5 ± 1.3% with a 1.61 eV bandgap perovskite



[BA<sub>0.09</sub>(FA<sub>0.83</sub>Cs<sub>0.17</sub>)<sub>0.91</sub>Pb(I<sub>0.6</sub>Br<sub>0.4</sub>)<sub>3</sub>] and  $15.8 \pm 0.8\%$  with a 1.72 eV bandgap perovskite [BA<sub>0.05</sub>(FA<sub>0.83</sub>Cs<sub>0.17</sub>)<sub>0.91</sub>Pb(I<sub>0.8</sub>Br<sub>0.2</sub>)<sub>3</sub>] (**Figure 21**). The cells showed stabilized performance under simulated sunlight in which they maintained 80% of their ‘post burn-in’ efficiency after 1000h air exposure and closer to 4000h when encapsulated (**Figure 22**).

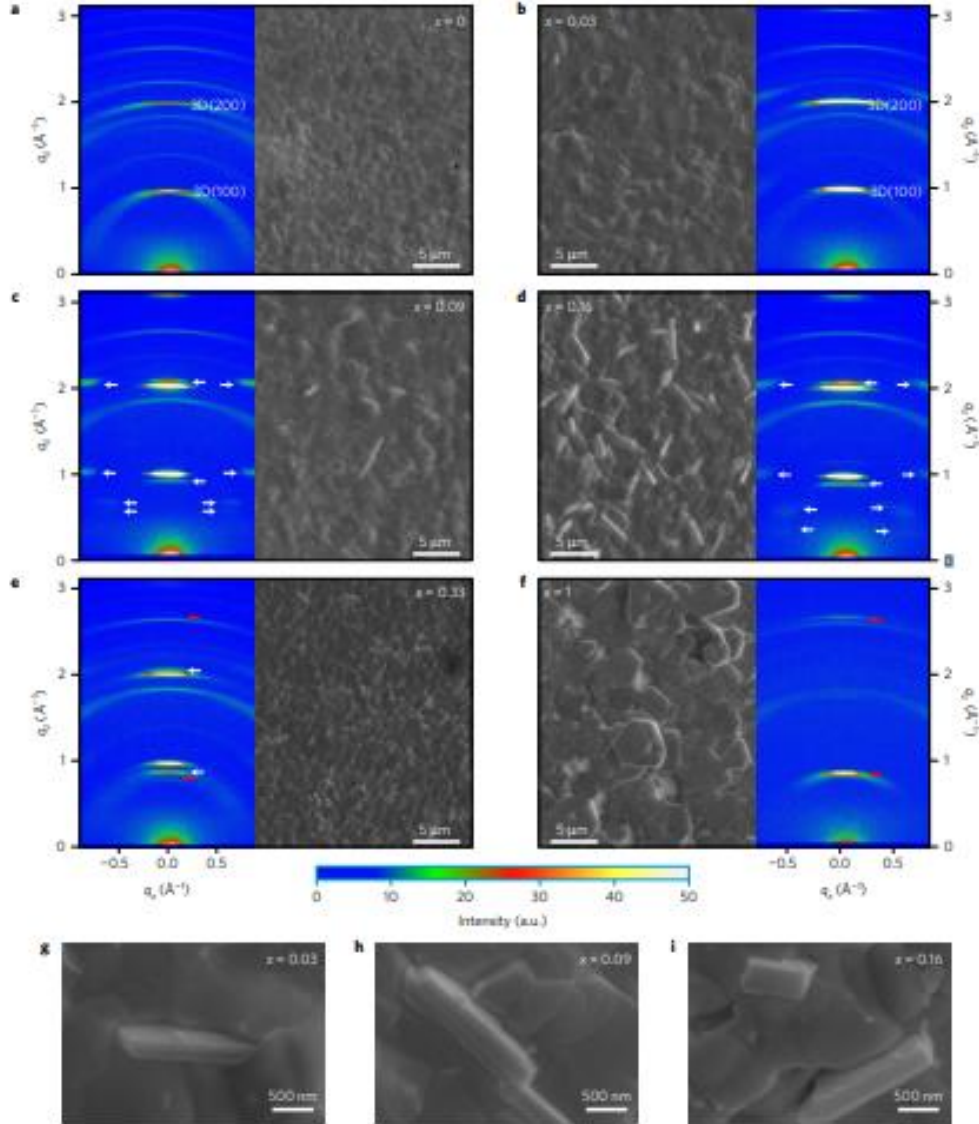


**Figure 20.** a-f) SEM images of post-annealed BA<sub>x</sub>(FA<sub>0.83</sub>Cs<sub>0.17</sub>)<sub>1-x</sub>Pb(I<sub>0.6</sub>Br<sub>0.4</sub>)<sub>3</sub> perovskite films with different BA content concentrations (insets: 2D-XRD images of respective films, where reflections at  $q_z \approx 1$  and  $2 \text{ \AA}^{-1}$  are assigned to the 3D perovskite (100) and (200), respectively. White arrows highlight diffraction peaks arising for low BA contents, and red arrows highlight diffraction peaks arising for high BA contents. Enlarged SEM images of g)  $x = 0.03$ , h)  $x = 0.09$  and i)  $x = 0.16$  films. Adapted with permission from ref.<sup>65</sup> Copyright © 2017, Nature Publishing Group.

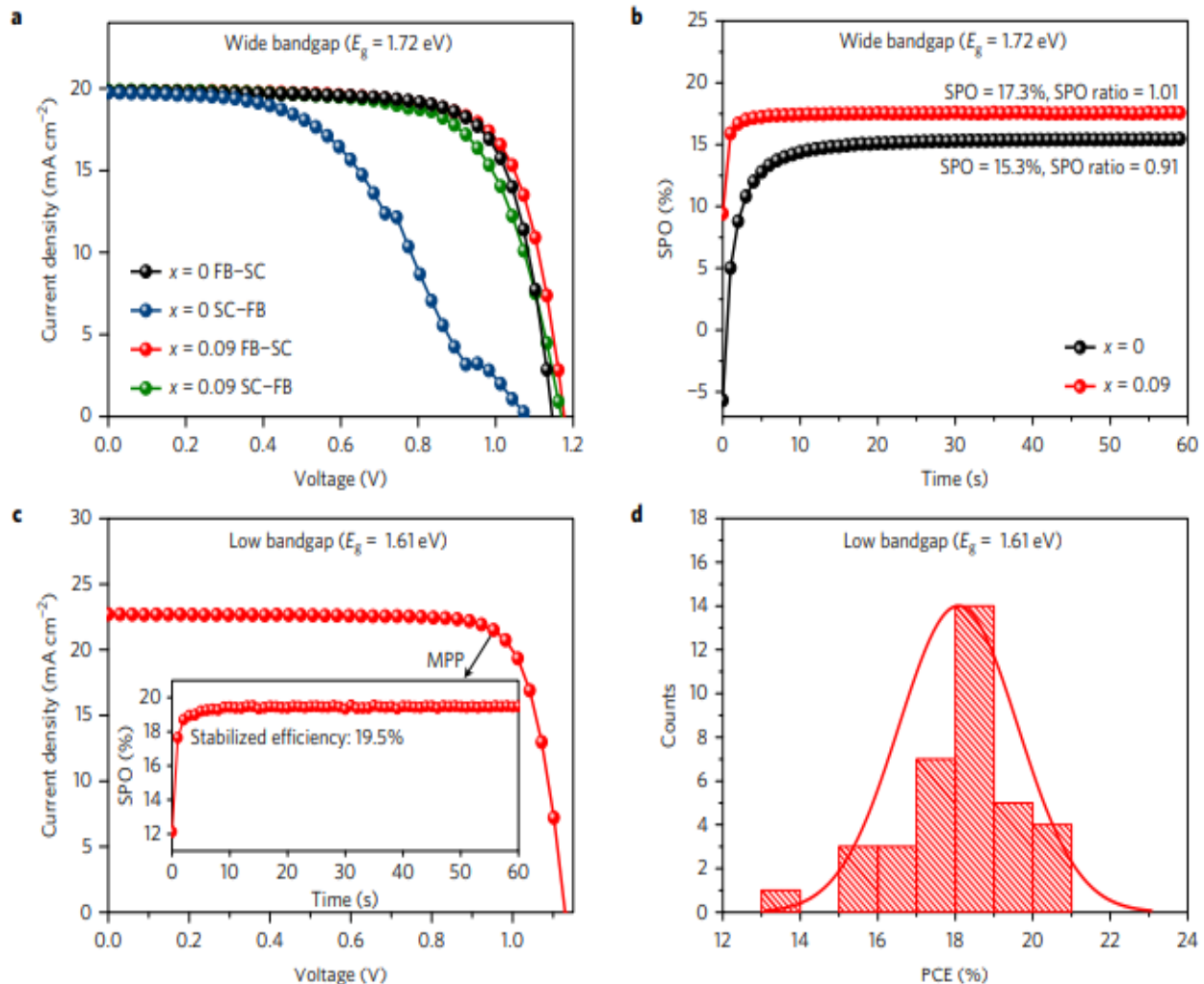


**Figure 21.** a) Current density-voltage curves for PSCs using the wide-bandgap  $\text{FA}_{0.83}\text{Cs}_{0.17}\text{Pb}(\text{I}_{0.6}\text{Br}_{0.4})_3$  ( $x = 0$ ) and  $\text{BA}_{0.09}(\text{FA}_{0.83}\text{Cs}_{0.17})_{0.91}\text{Pb}(\text{I}_{0.6}\text{Br}_{0.4})_3$  ( $x = 0.09$ ) perovskite active layers under AM1.5G irradiation. b) Stabilized power output of champion cells at the maximum power point for 60 s. c) Current density-voltage curve of the champion PSC using a low-bandgap  $\text{BA}_{0.05}(\text{FA}_{0.83}\text{Cs}_{0.17})_{0.95}\text{Pb}(\text{I}_{0.8}\text{Br}_{0.2})_3$  perovskite active layer under AM1.5G irradiation (inset: corresponding stabilized power output). d) PCE histogram of  $\text{BA}_{0.05}(\text{FA}_{0.83}\text{Cs}_{0.17})_{0.95}\text{Pb}(\text{I}_{0.8}\text{Br}_{0.2})_3$  PSCs. Adapted with permission from ref.<sup>65</sup> Copyright © 2017, Nature Publishing Group.

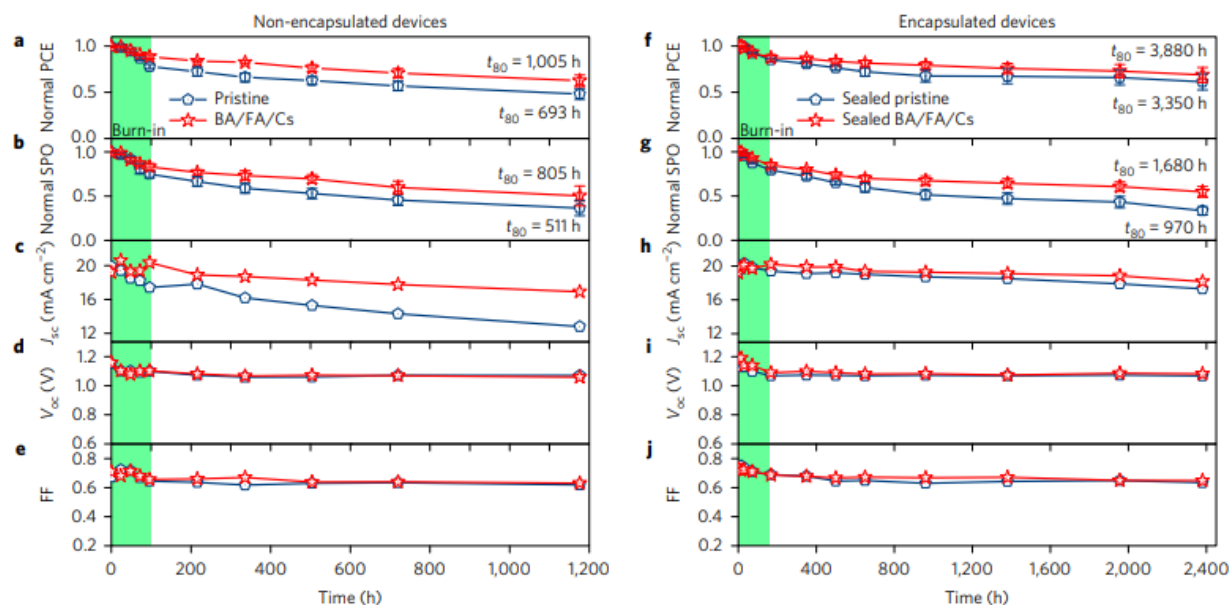


**Figure 22.** Stability curves of a) – e) non-encapsulated and f) – j) encapsulated PSCs using  $\text{FA}_{0.83}\text{Cs}_{0.17}\text{Pb}(\text{I}_{0.6}\text{Br}_{0.4})_3$  (navy blue lines; pristine) and  $\text{BA}_{0.09}(\text{FA}_{0.83}\text{Cs}_{0.17})_{0.91}\text{Pb}(\text{I}_{0.6}\text{Br}_{0.4})_3$  (red lines; BA/FA/Cs) perovskite layers aged under AM1.5G 76 mW/cm<sup>2</sup> and 45 RH% at open-circuit. An exponential decay over the first ~100 h is followed by an approximate linear decay. a), f), b) and g) are normalized and averaged over eight devices, whilst c), h), d), i), e) and j) are shown for champion devices. Adapted with permission from ref.<sup>65</sup> Copyright © 2017, Nature Publishing Group.

Grancini et al. were the first to achieve a 1-year stable 2D/3D PSC by engineering a multidimensional junction of  $(\text{HOOC}(\text{CH}_2)_4\text{NH}_3)_2\text{PbI}_4/\text{CH}_3\text{NH}_3\text{PbI}_3$ .<sup>66</sup> The optimal 2D/3D (3% AVAI molar ratio) forms a passivated interface that showed 12.9% PCE in a carbon-based architecture, (**Figure 23**) and 14.6% in standard mesoporous devices structures (**Figure 24**). For the mesoporous architecture, the 2D/3D PCE maintained up to 60% of the initial efficiency value after 300h of continuous illumination under Argon (Ar) atmosphere at 45°C (**Figure 24c**). While for printable HTM-free architecture, the module retained exceptional stability by maintaining a PCE of 11.2% over 10,000 h (1 year) at a stabilized temperature of 55°C under AM 1.5G at short-circuit conditions without any losses (**Figure 24c**). This innovative and stable perovskite architecture reveals the paramount role of 2D perovskite in engineering stable devices and paves the way for large scale commercialization of PSCs.

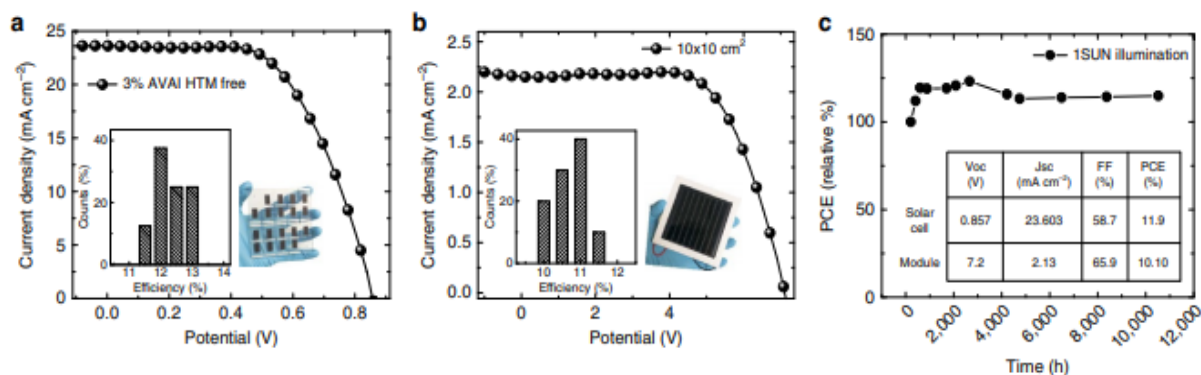


**Figure 23.** Current density-voltage curves of HTM-free a) PSC and b) a 10 x 10 cm<sup>2</sup> solar module employing 2D/3D perovskite with 3%AVAI measured under AM1.5G irradiation (inset: device statistics and picture of devices). c) Stability test of module under AM 1.5 G conditions at 55 °C and short circuit conditions (inset: photovoltaic parameters of the PSC and solar module represented in a) and b). Reproduced under the terms of the CC-BY license<sup>66</sup>. Copyright 2017, The authors, published by Nature communications.

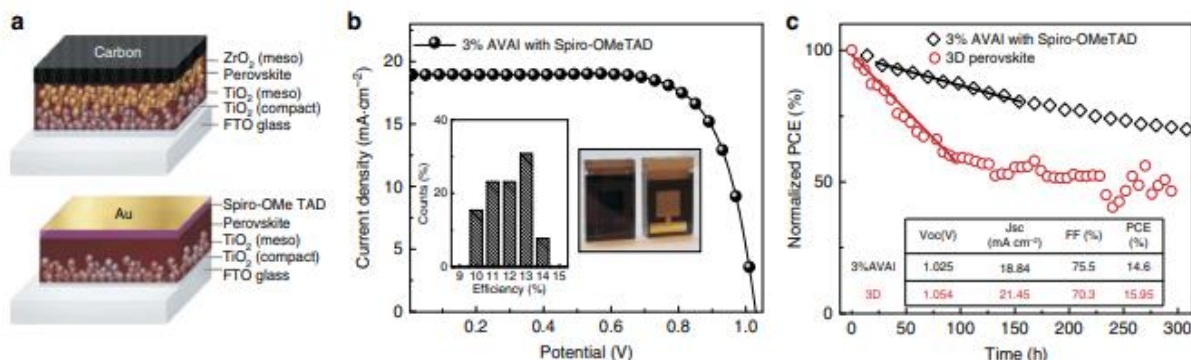


**Figure 24.** a) Device architecture of spiro-OMeTAD-free and spiro-OMeTAD-containing PSCs. b) Current density-voltage curve of spiro-OMeTAD-containing PSC employing a 2D/3D perovskite with 3% HOOC(CH<sub>2</sub>)<sub>4</sub>NH<sub>3</sub>I measured under AM1.5G irradiation (inset: device statistics and photo of PSC). c) Stability curves of the spiro-OMeTAD-containing PSC compared with the spiro-OMeTAD-free mixed 2D/3D PSC at maximum power point under AM 1.5G illumination measured in an inert Ar atmosphere at 45 °C (inset: champion device parameters). Reproduced under the terms of the CC-BY license<sup>66</sup>. Copyright 2017, The authors, published by Nature communications.

Furthermore, Jodlowski et al. reported the incorporation of a large bulky organic cation Guanidinium (CH<sub>6</sub>N<sub>3</sub><sup>+</sup>, Gua) into MAPbI<sub>3</sub> perovskite crystal structure.<sup>67</sup> It was demonstrated when GAI cation is combined with methylammonium in a mixed MA<sub>1-x</sub>Gua<sub>x</sub>PbI<sub>3</sub> (0 < x < 0.25); x refers to molar ratios, 2D/3D perovskite is formed with enhanced thermal and environmental stability. With this approach, solar cells delivered average power conversion efficiencies of 19.2 ± 0.4% (**Figure 25**) and stabilized performance for



over 1,000 h under continuous white light illumination at maximum power point conditions at an argon atmosphere (**Figure 26**). This study opens the way for the exploration of organic cations that are beyond the limit of the tolerance factor to achieve highly efficient and stabilized perovskite solar cells.

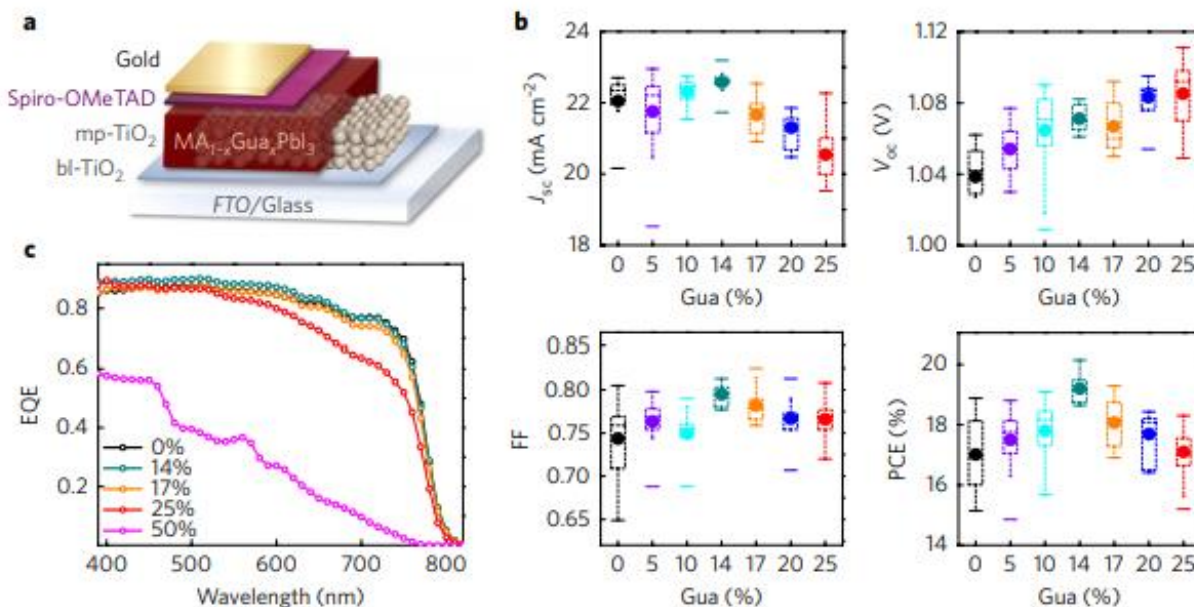


**Figure 25.** a) Device architecture of PSCs incorporating Gua cations. b) Statistical data box plots of J<sub>sc</sub>, V<sub>oc</sub>, FF and PCEs (obtained across 17 cells per condition) of PSCs prepared with MA<sub>1-x</sub>Gua<sub>x</sub>PbI<sub>3</sub> as a function of x. c) IPCE spectra of MA<sub>1-x</sub>Gua<sub>x</sub>PbI<sub>3</sub> for x = 0.14, 0.17 and 0.25, MAPbI<sub>3</sub> (0%) and those incorporating 50% Gua, all measured under AM1.5G irradiation. Reproduced under the terms of the CC-BY license<sup>67</sup>. Copyright 2017, The authors, published by Nature Energy.

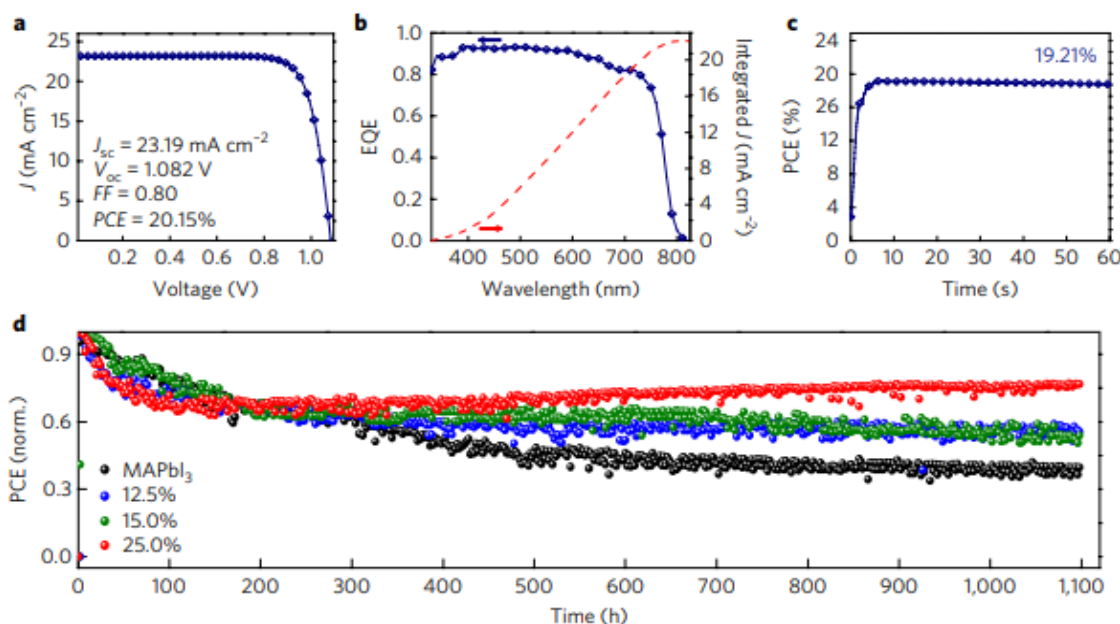


**Figure 26.** a) Current density-voltage curve measured under AM1.5G irradiation and b) EQE spectrum of the champion cell prepared with mixed MA/Gua perovskite containing 14% Gua. c) Maximum power point tracking under 1 Sun AM1.5G illumination measured in air for PSC containing  $\text{MA}_{1-x}\text{Gua}_x\text{PbI}_3$  ( $x = 0.14$ ). d) normalized PCE of  $\text{MA}_{1-x}\text{Gua}_x\text{PbI}_3$  PSCs ( $x = 0, 0.125, 0.15, 0.25$ ) at 60 °C under continuous light illumination and maximum power point tracking in an inert Ar atmosphere. Reproduced under the terms of the CC-BY license<sup>67</sup>. Copyright 2017, The authors, published by Nature Energy.

Ma et al. reported a thin layer of cyclopropyl ammonium over the 3D  $\text{MAPbI}_3\text{Cl}_{3-x}$  which provided a hydrophobic nature to the 2D/3D perovskite.<sup>68</sup> In a humidity test environment  $63 \pm 5\%$ , the 3D perovskite degraded completely only after 8 days while the 2D/3D one exhibited robust moisture stability for 40 days. The 2D/3D retained 54% of its initial efficiency (13.86% PCE) after 220 hours, whereas the 3D degraded within only 50 hours (13.12% PCE).

Following the same approach, Lin et al. fabricated a 2D/3D stacking structure by depositing n-butylammonium (BA) on top of the 3D  $\text{MAPbI}_3$  perovskite layer.<sup>69</sup> Compared to the 3D device (17.28%), the BA-treated devices achieved a higher PCE of 19.56% owing to the significant improvement in  $V_{oc}$  (1.1V). The 3D film degraded to 69.8% of its original efficiency after continuous heating for 100 h while the modified BA-treated devices retained 96.5% under the same aging conditions.

### 3.4. Suppressed ion migration in low dimensional Perovskites

The low dimensional perovskite has been studied to reveal suppressed ion migration comparing to 3D perovskite. Lin et al. investigated the ionic motion in 3D MAPbI<sub>3</sub> and 2D (BA<sub>2</sub>)(MA)<sub>3</sub>Pb<sub>4</sub>I<sub>13</sub> Ruddlesden-Popper phase perovskite (**Figure 27a**).<sup>70</sup> They conducted temperature-dependent electrical conductivity measurement to measure the activation energy of ion-migration in both perovskite structures. The temperature-dependent measurement was conducted under both dark and light 'under 0.25 sun illumination' conditions. As a comparison, 3D MAPbI<sub>3</sub> shows the activation energy for ion-conduction was fitted to be 0.03 eV under light condition and increased to 0.19 eV at dark condition. The ionic conductivity began to dominate over the electronic conductivity at high temperature, 260 K and was reduced below that temperature (**Figure 27b**). However, in 2D (BA)<sub>2</sub>(MA)<sub>3</sub>Pb<sub>4</sub>I<sub>13</sub> film, there was no sign of ionic conductivity when the temperature was increased in both dark and light conditions. These results indicate that ion migration was suppressed in 2D perovskites and it was suggested that this is due to the presence of the large bulky organic spacers which act as ion-scavengers (**Figure 27c**).

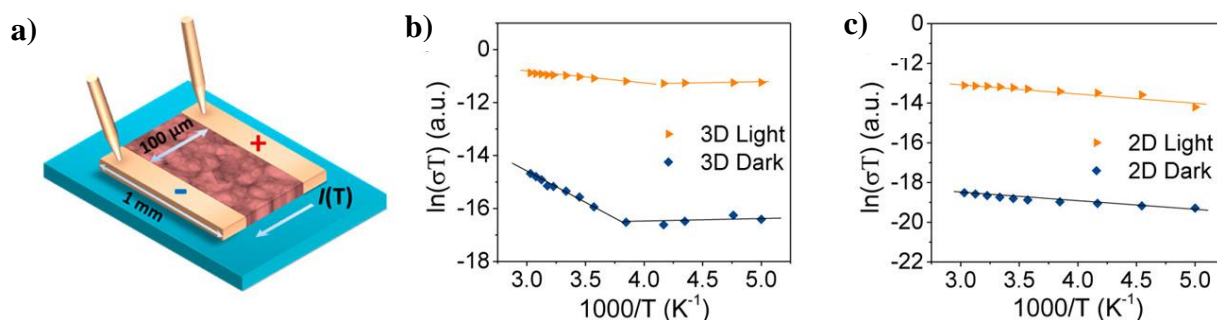


**Figure 27.** a) Schematic of the temperature-dependent electrical conductivity measurements showing b) MAPbI<sub>3</sub> and c) (BA)<sub>2</sub>(MA)<sub>3</sub>Pb<sub>4</sub>I<sub>13</sub> perovskite films. Reprinted with permission from ref.<sup>70</sup> Copyright © 2017 American Chemical Society.

Similarly, Huang et al. investigated iodine ion-migration in 3D Cs<sub>0.05</sub>FA<sub>0.8</sub>MA<sub>0.15</sub>PbI<sub>2.88</sub>Br<sub>0.04</sub>Cl<sub>0.08</sub> perovskite and 2.5D perovskite formed by substituting the organic site-A cation by ALA ligand molecule.<sup>71</sup> Using time-of-flight secondary ion mass spectroscopy (TOF-SIMS), the pristine film showed a higher rate of iodine ions migrating from the perovskite bulk to the spiro-OMeTAD HTM layer while the 2.5D device showed suppressed ion-migration with a significant reduced rate of migrating ions (**Figure 28**). By suppressing ion migration, the 2D perovskite exhibits outstanding device stability and negligible hysteresis.

Li and co-workers managed to achieve hysteresis-free devices by incorporating 1,4-Butanediamine (BEA)-low dimensional perovskite into two different perovskite structures which are (BEA)<sub>0.5</sub>MA<sub>3</sub>Pb<sub>3</sub>I<sub>10</sub> and (BEA)<sub>0.5</sub>Cs<sub>0.15</sub>(FA<sub>0.83</sub>MA<sub>0.17</sub>)<sub>2.85</sub>Pb<sub>3</sub>(I<sub>0.83</sub>Br<sub>0.17</sub>)<sub>10</sub> films.<sup>72</sup>

PSCs prepared by mixing MA with BEA exhibited a PCE of 14.86% with negligible hysteresis (**Figure 29b**). The perovskite with mixed cations BEA, Cs, FA and MA at the A-site achieved a record PCE of 17.39% showing no hysteresis in J-V curves (**Figure 29c**). Furthermore,  $(\text{BEA})_{0.5}(\text{Cs})_{0.15}(\text{FA})_{0.83}(\text{MA})_{0.17}\text{Pb}_3(\text{I})_{0.83}(\text{Br})_{0.17}\text{I}_{10}$  maintained 90% of their initial power conversion efficiency in ambient atmosphere after 2400h (**Figure 29d**) and showed no significant degradation under continuous illumination at room temperature (**Figure 29e**).

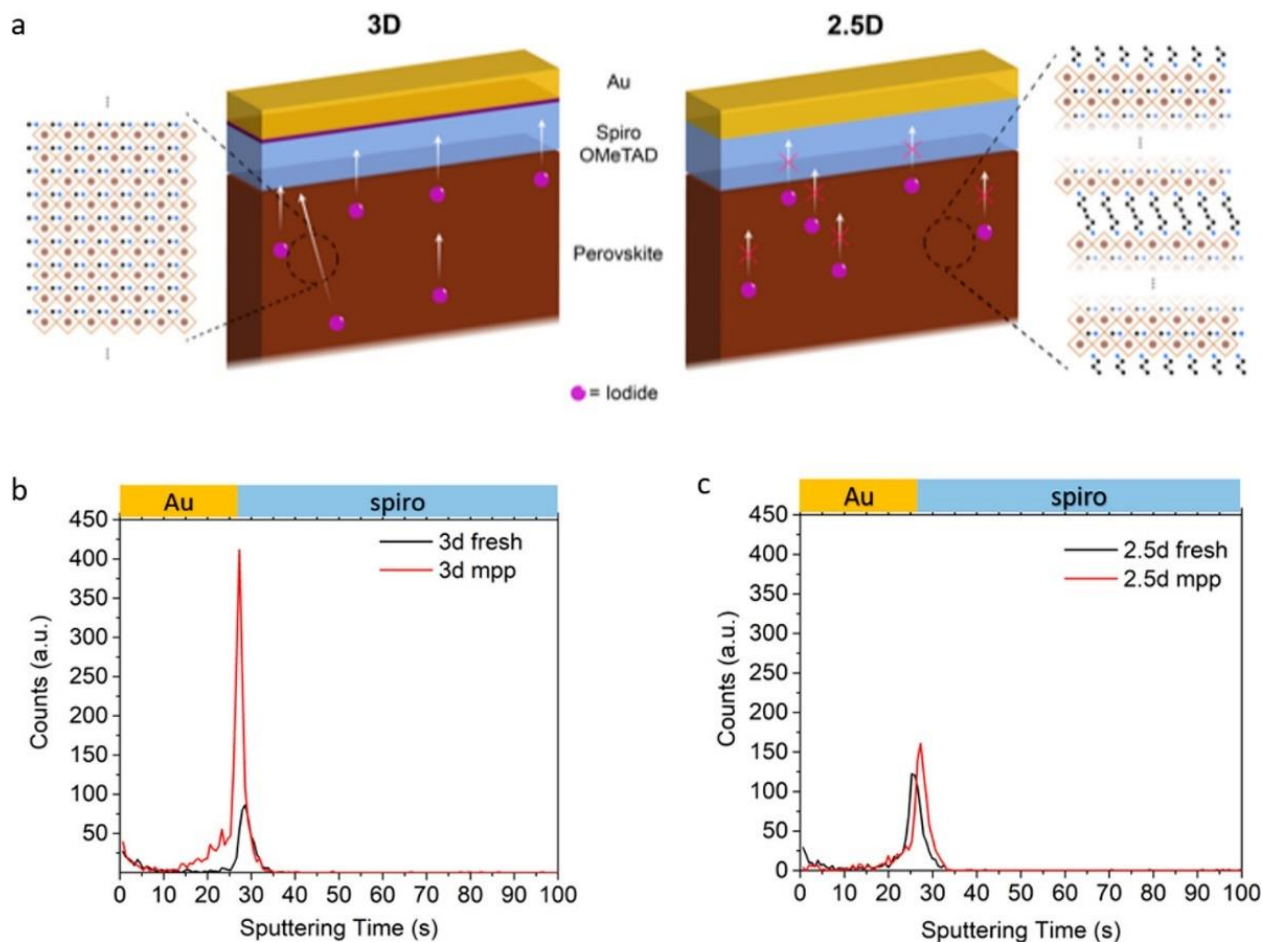


**Figure 28.** a) Schematic of iodine ion migration throughout the 3D perovskite device compared to suppressed migration in the 2.5D perovskite device. b)  $\text{Au}_{2f}^-$  – depth profile comparison between fresh and 60 h aged 3D PSCs. c)  $\text{Au}_{2f}^-$  – depth profile comparison between fresh and 60 h aged 2.5D PSCs. Reprinted with permission from ref.<sup>71</sup> Copyright © 2019 American Chemical Society



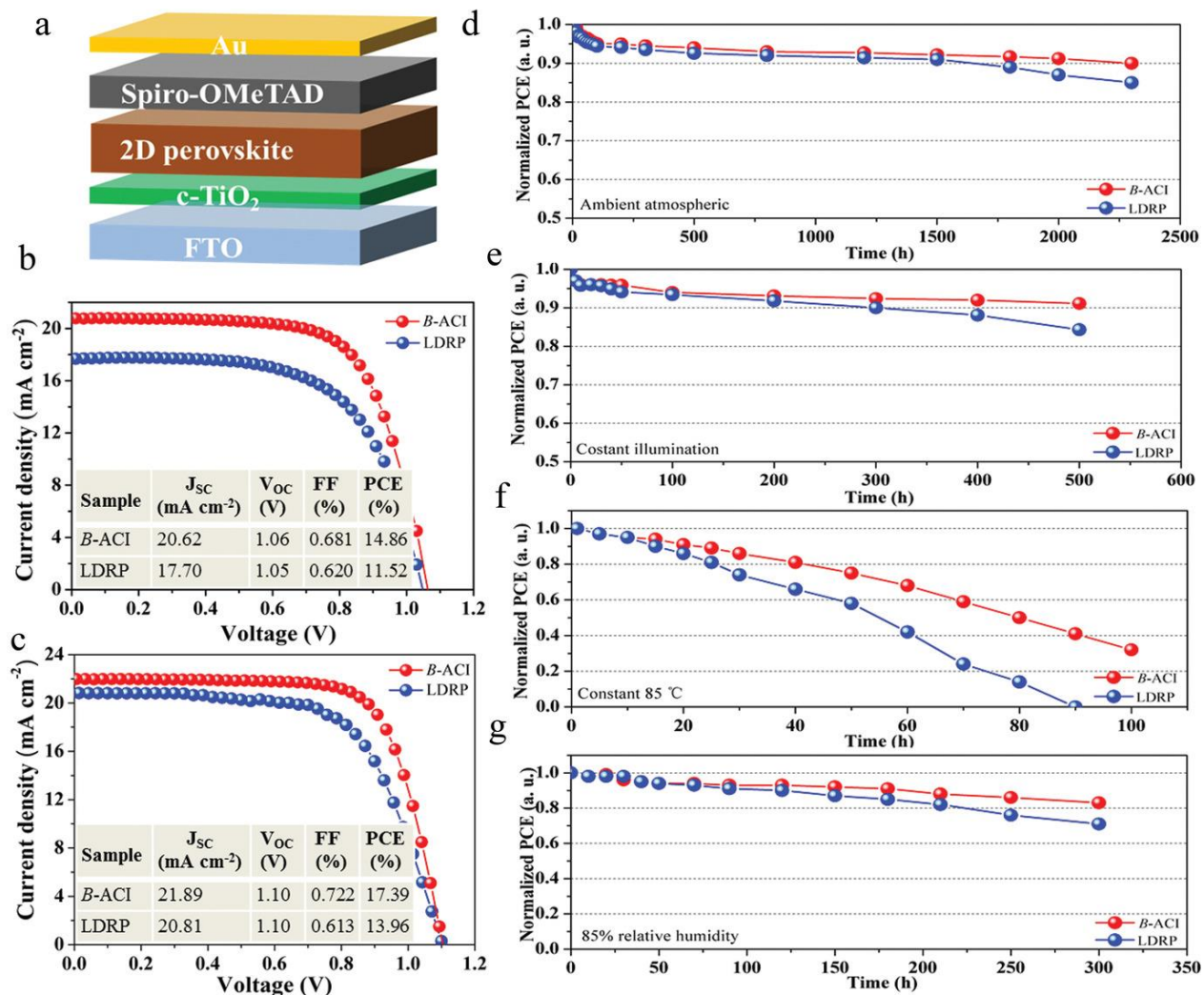


**Figure 29.** a) Device architecture of B-ACI and LDRP PSCs. Current-density voltage curves of B-ACI and LDRP PSCs with b) (BEA)<sub>0.5</sub>MA<sub>3</sub>Pb<sub>3</sub>I<sub>10</sub> and (BA)<sub>2</sub>MA<sub>2</sub>Pb<sub>3</sub>I<sub>10</sub> photoactive layers and c) (BEA)<sub>0.5</sub>Cs<sub>0.15</sub>(FA<sub>0.83</sub>MA<sub>0.17</sub>)<sub>2.85</sub>Pb<sub>3</sub>(I<sub>0.83</sub>Br<sub>0.17</sub>)<sub>10</sub> and (BA)<sub>2</sub>Cs<sub>0.1</sub>(FA<sub>0.83</sub>MA<sub>0.17</sub>)<sub>1.9</sub>Pb<sub>3</sub>(I<sub>0.83</sub>Br<sub>0.17</sub>)<sub>10</sub> photoactive layers, measured under AM1.5G irradiation. Normalized PCE decay of B-ACI and LDRP PSCs under d) ambient atmospheric conditions, e) constant illumination in the glove-box, f) constant temperature of 85 °C, and g) 85% relative humidity in a humidity chamber. Reprinted with permission from ref.<sup>72</sup> Copyright © 2019 WILEY-YCH Verlag GmbH & Co. KGaA, Weinheim.

Zheng and Co-workers employed a novel organic cation HOOCCCH<sub>2</sub>NH<sub>3</sub><sup>+</sup> (Glycine cation, simplified as Gly<sup>+</sup>) into (Cs<sub>0.05</sub>FA<sub>0.95</sub>PbI<sub>3</sub>)<sub>0.9</sub>(FAPbBr<sub>3</sub>)<sub>0.1</sub> 3D perovskite to form low-dimensional Ruddlesden Popper phase perovskites.<sup>73</sup> They were formed based on the general formula [Gly<sub>2</sub>(Cs<sub>0.05</sub>FA<sub>0.95</sub>)<sub>n-1</sub>Pb<sub>n</sub>I<sub>3n-1</sub>Cl<sub>2</sub>]<sub>0.9</sub>(FAPbBr<sub>3</sub>)<sub>0.1</sub> at different n values (n=4, 6 and 8) and the [BA<sub>2</sub>(Cs<sub>0.05</sub>FA<sub>0.95</sub>)<sub>3</sub>Pb<sub>4</sub>I<sub>13</sub>]<sub>0.9</sub>(FAPbBr<sub>3</sub>)<sub>0.1</sub> (BA, n = 4) for comparison. Gly-based Ruddlesden popper phase low dimensional perovskite showed high PCE values

of 18.06 for  $n=8$  devices and 15.61% for  $n=4$  devices with negligible hysteresis (**Figure 30b and c**). Furthermore, unencapsulated Gly-based devices showed better long-term stability at MPP conditions compared to BA-devices (**Figure 30d**).

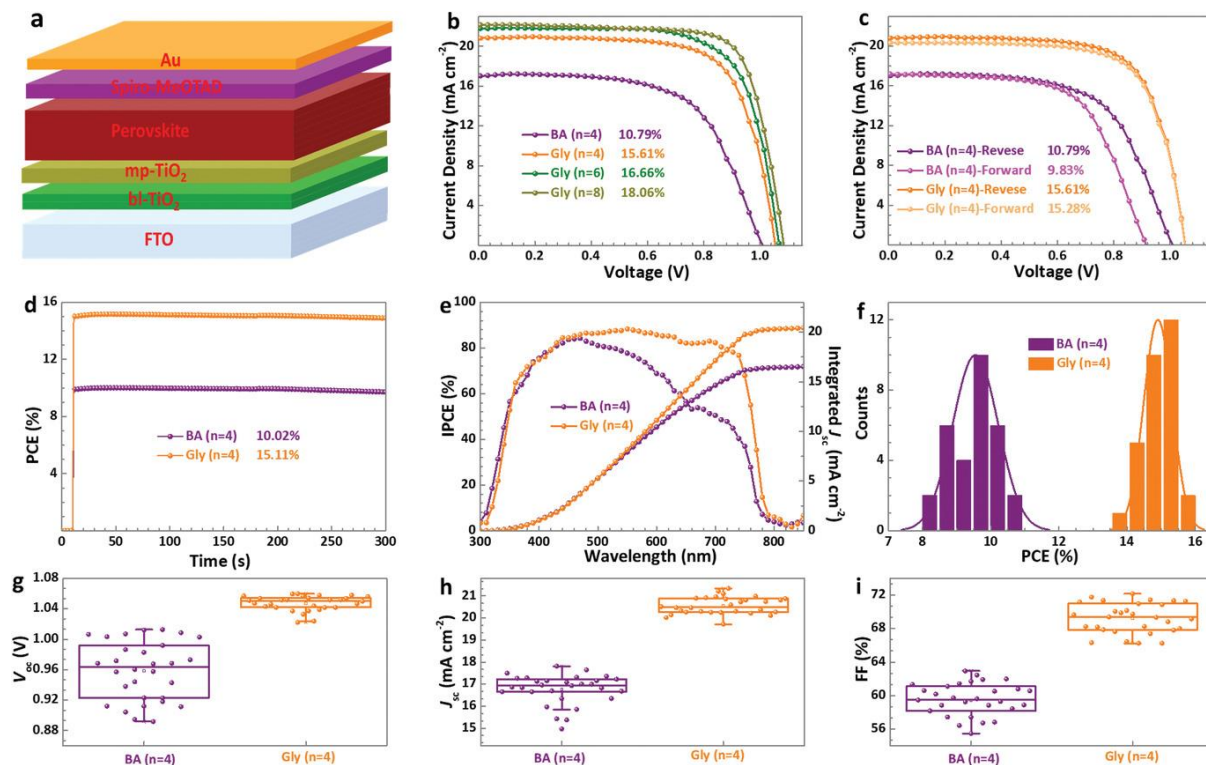


**Figure 30.** a) Schematic of mesoscopic PSC architecture. Current density-voltage curves of b) BA ( $n = 4$ ) and Gly ( $n = 4, 6$ , and  $8$ ) under reverse scan directions and c) BA ( $n = 4$ ) and Gly ( $n = 4$ ) PSCs under reverse and forward scan directions measured under AM1.5G irradiation. d) Steady-state measurement of the PCE at the maximum power point, e) IPCE spectra, f) PCE distributions, g) V<sub>oc</sub> h) J<sub>sc</sub>, and i) FF distributions of BA ( $n = 4$ ) and Gly ( $n = 4$ ) PSCs. Adapted with permission from ref.<sup>73</sup> Copyright © 2020 WILEY-YCH Verlag GmbH & Co. KGaA, Weinheim

Liu and co-workers designed halogenated low-dimensional benzylammonium organic cations as a capping layer on top of the 3D Cs<sub>0.05</sub>FA<sub>0.95</sub>PbI<sub>2.7</sub>Br<sub>0.3</sub> to passivate surface defects, suppress non-radiative losses and improve charge extraction to the hole transport layer leading to significantly reduced voltage losses.<sup>74</sup> All of the devices

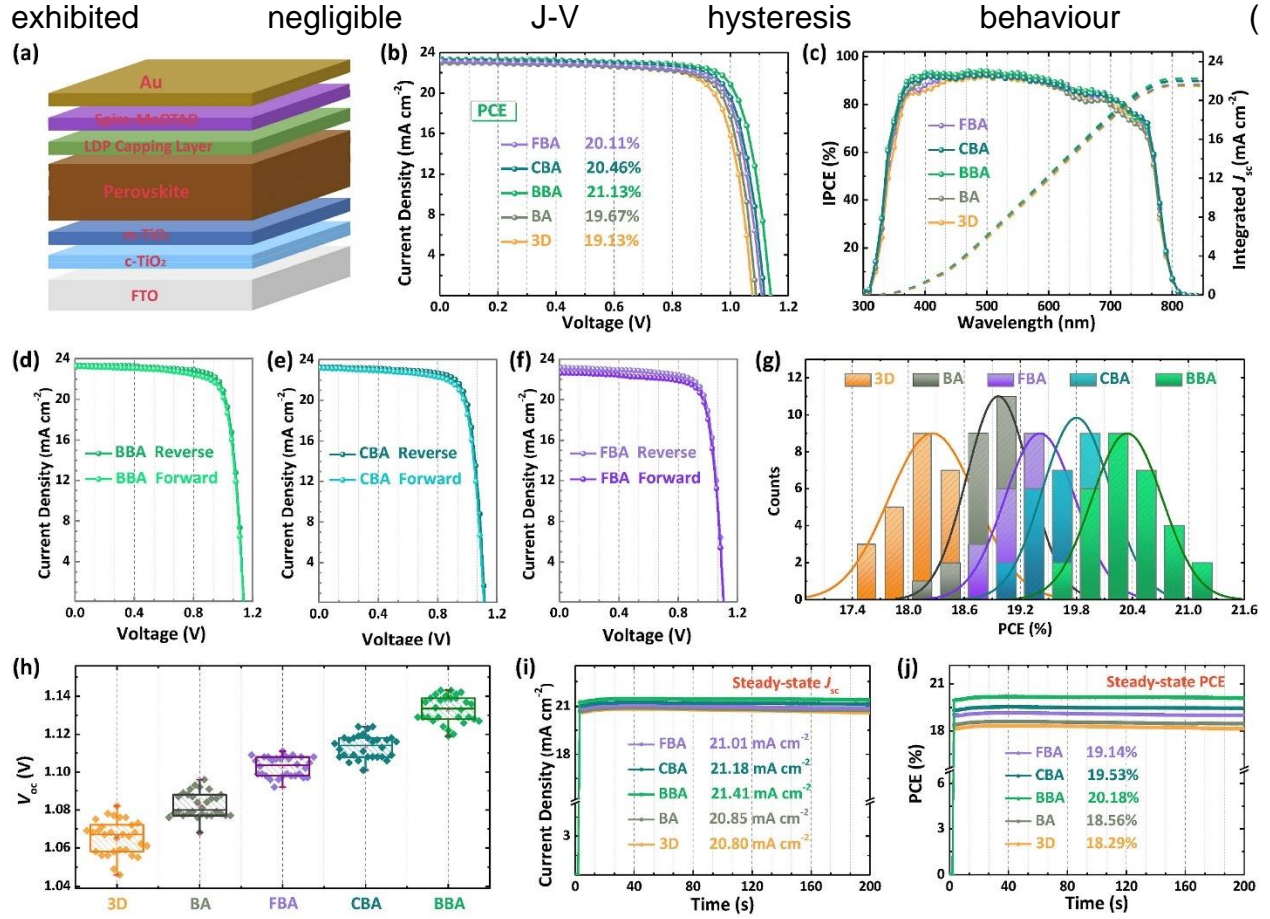


**Figure 31).** The optimal 4-bromobenzylammonium-based devices achieved remarkable PCE of 21.13% and enhanced open-circuit voltage of 1.14 V. The treated devices showed excellent long-term stability when exposed to moisture, heat and UV irradiation (**Figure 32**). This work provides insights about the importance of tuning the chemical properties of introduced cations for high performance and stabilized perovskite devices.



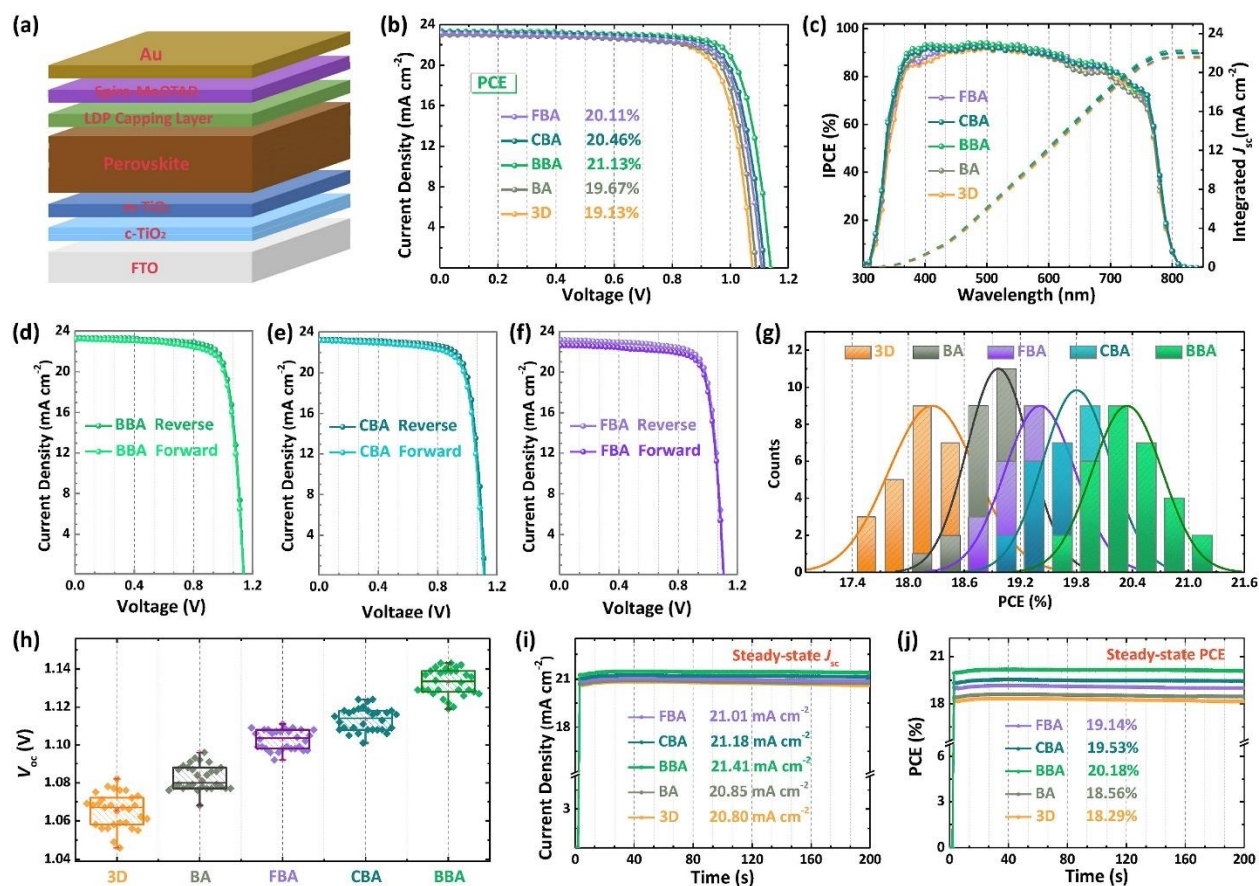


**Figure 31.** a) Schematic of PSC architecture employing an LDP capping layer. b) Current density-voltage curves and c) IPCE spectra of unmodified and LDP-modified PSCs measured under AM1.5G irradiation. Current-density voltage curves of devices employing d) BBA, e) CBA and f) FBA LDP capping layers, and g) compiled PCE histograms fitted with gaussian distributions. h) Box plots showing statistical variation of the  $V_{oc}$  across 30 devices. Stabilized i) photocurrent density and j) PCE at maximum power point over time of each unmodified or LDP-modified PSC. Adapted with permission from ref.<sup>74</sup>. Copyright © 2020 Elsevier Ltd. All rights reserved.



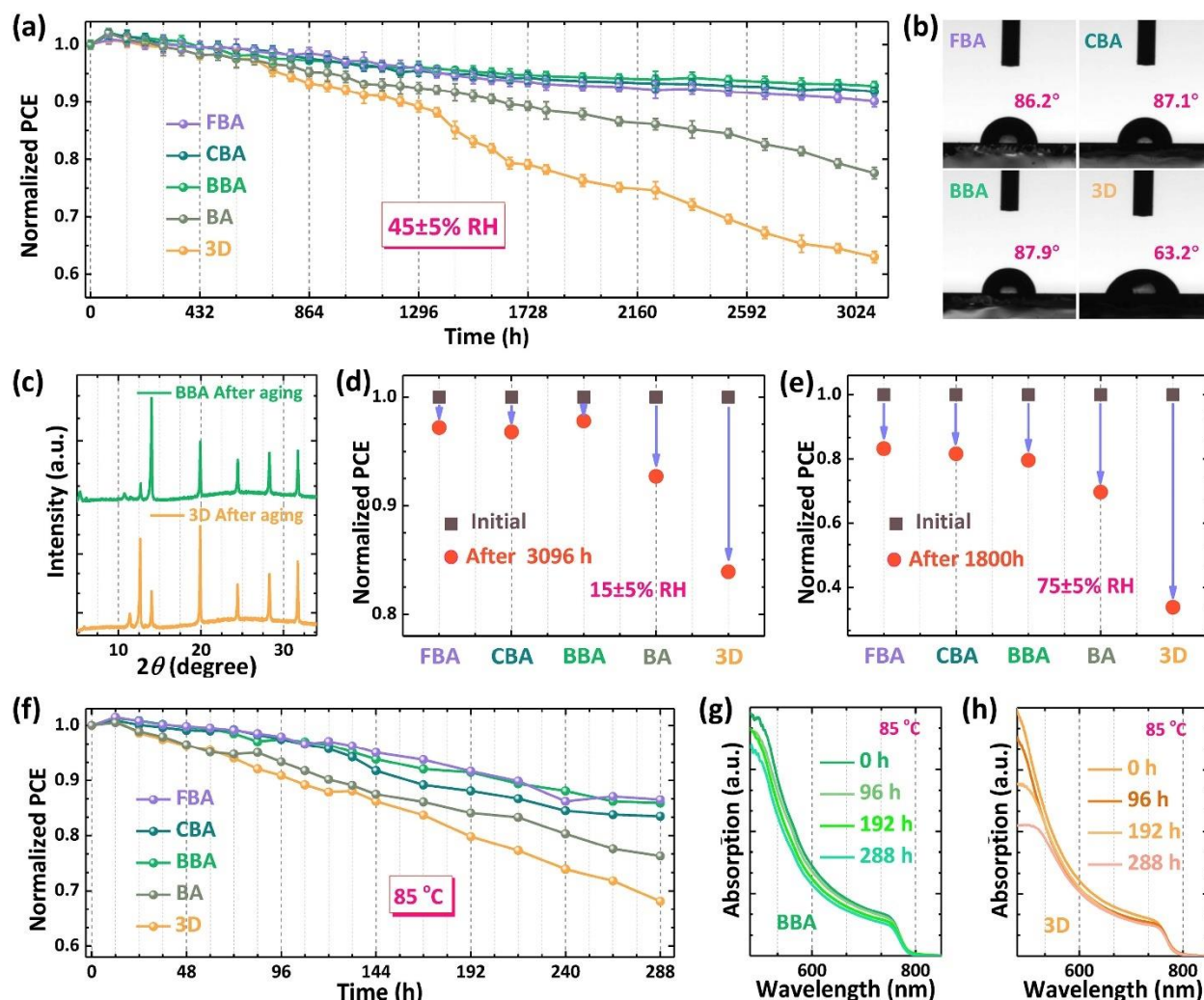


**Figure 32.** a) Normalized PCE variation of unsealed PSCs exposed to 45 ± 5% RH and measured under AM1.5G irradiation. b) Water contact angles measurements of pristine 3D perovskite film and those modified by FBAI, CBAI and BBAI. c) XRD patterns of 3D and BBA-based perovskite films before and after aging in 45 ± 5% RH. Normalized PCE variation of unsealed PSCs when exposed to the relative humidity of d) 15 ± 5% RH and e) 75 ± 5% RH. f) Normalized PCE variation of unsealed PSCs when exposed to 85 °C. UV-vis absorption spectra of g) 3D and h) BBA-based films before and after aging at 85 °C. Adapted with permission from ref.<sup>74</sup>. Copyright © 2020 Elsevier Ltd. All rights reserved.

Following the direction of modifying organic spacers, Shi et al. introduced the fluorination of the organic spacer PEA cation to fabricate quasi-2D  $(\text{PEA})_2(\text{MA})_{n-1}\text{Pb}_{n+1}\text{I}_{3n+1}$  based-perovskite solar cells.<sup>75</sup> The optimal device  $(4\text{FPEA})_2(\text{MA})_4\text{Pb}_5\text{I}_{16}$  ( $n=5$ ) exhibited outstanding PCE of 17.3% with negligible hysteresis, a  $V_{\text{oc}}$  of 1.16V,  $J_{\text{sc}}$  of 19  $\text{mA}/\text{cm}^2$  and a FF of 79% (**Figure 33a**). The 4-fluoro-phenethylammonium (4FPEA) organic spacer optimized the film morphology, enhanced the crystallinity, and promoted

preferential growth along the vertical direction which resulted in reduced trap densities and enabled more efficient charge transport (**Figure 34**). For stability tests, the unencapsulated 4FPEA-based devices retained 93% of their original efficiency under ambient air with a humidity level  $60\pm5\%$  (**Figure 35a**). Furthermore, 4FPEA-based devices showed robust thermal stability by almost retaining their PCEs unchanged when annealed continuously for 500 h at  $55^\circ\text{C}$  in a nitrogen atmosphere (**Figure 35c**).

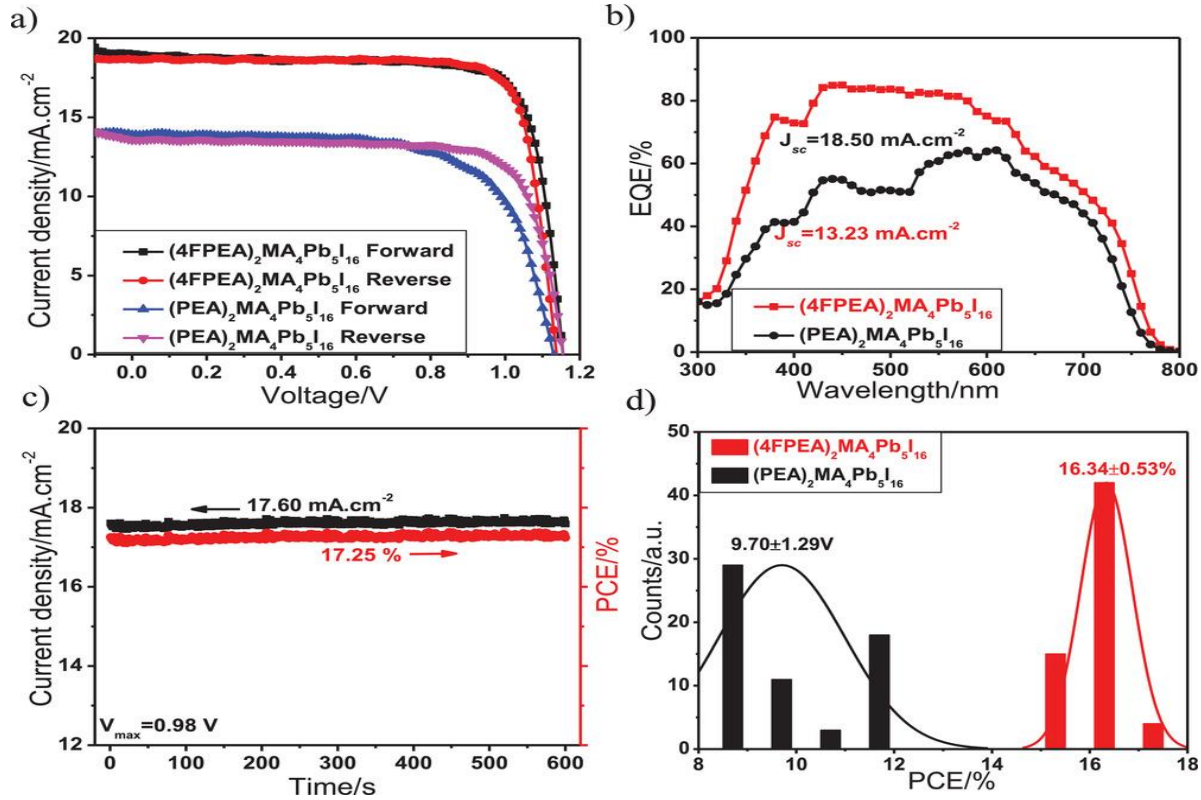


**Figure 33.** a) Current density-voltage curves measured under AM1.5G irradiation and b) IPCE spectra of the optimized devices based on  $(\text{PEA})_2\text{MA}_4\text{Pb}_5\text{I}_{16}$  and  $(4\text{FPEA})_2(\text{MA})_4\text{Pb}_5\text{I}_{16}$  perovskites. c) Stabilized photocurrent output of the champion  $(4\text{FPEA})_2(\text{MA})_4\text{Pb}_5\text{I}_{16}$  device and d) PCE histograms fitted with gaussian distributions. Reprinted with permission from ref.<sup>75</sup>. Copyright © 2019 WILEY-YCH Verlag GmbH & Co. KGaA, Weinheim.

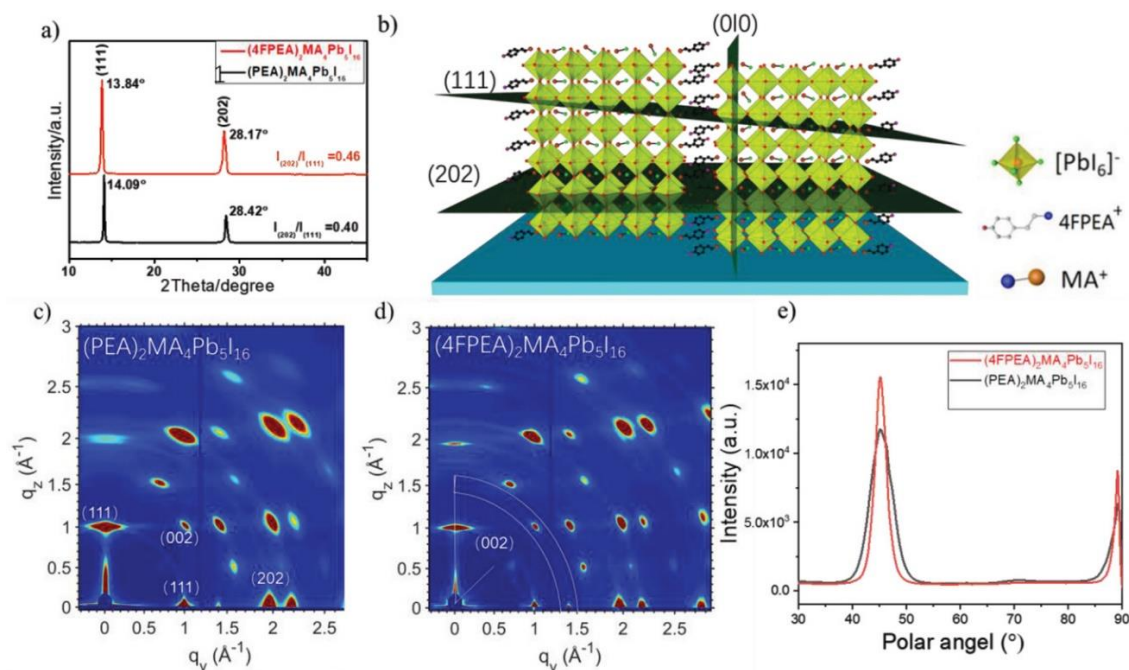


**Figure 34.** a) X-ray diffraction patterns of  $(\text{PEA})_2\text{MA}_4\text{Pb}_5\text{I}_{16}$  and  $(4\text{FPEA})_2\text{MA}_4\text{Pb}_5\text{I}_{16}$  films. b) Schematic illustration of the (111) and (020) orientations of  $(4\text{FPEA})_2\text{MA}_4\text{Pb}_5\text{I}_{16}$  perovskite crystal. 2D GIWAXs of c)  $(\text{PEA})_2\text{MA}_4\text{Pb}_5\text{I}_{16}$  and d)  $(4\text{FPEA})_2(\text{MA})_4\text{Pb}_5\text{I}_{16}$ . e) Polar angle spectrum at the peak of (002). Reprinted with permission from ref.<sup>75</sup>. Copyright © 2019 WILEY-YCH Verlag GmbH & Co. KGaA, Weinheim.

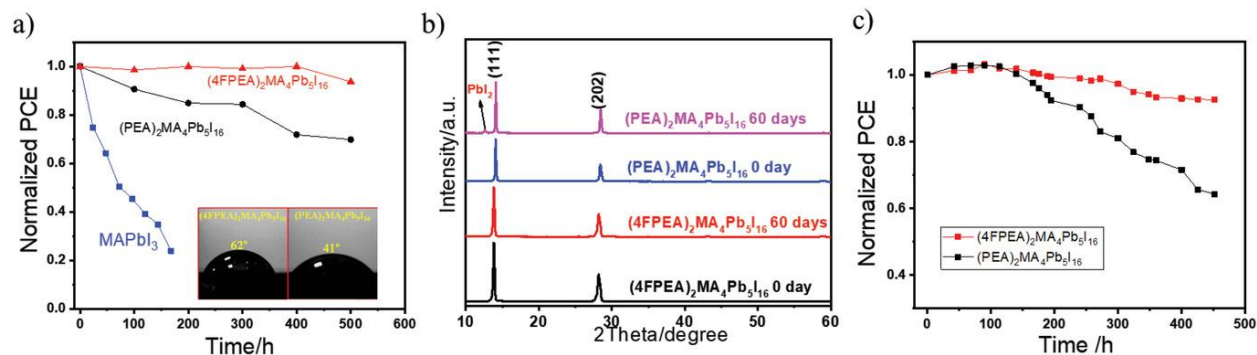


**Figure 35.** a) Stability tests of unsealed devices based on  $(\text{PEA})_2\text{MA}_4\text{Pb}_5\text{I}_{16}$  and  $(4\text{FPEA})_2\text{MA}_4\text{Pb}_5\text{I}_{16}$  stored under air atmosphere with a humidity of  $60 \pm 5\%$  (inset: contact angle measurements). b) XRD patterns of perovskite films stored in air over 60 days. c) Thermal stability of devices upon  $55^\circ\text{C}$  annealing under an inert  $\text{N}_2$  atmosphere. Reprinted with permission from ref.<sup>75</sup>. Copyright © 2019 WILEY-YCH Verlag GmbH & Co. KGaA, Weinheim.

Chaudhary and co-workers incorporated organic ligand 1-naphthylammonium iodide (NMAI) into MAPbI<sub>3</sub> to form a mixed dimensional (NMA)<sub>2</sub>(MA)<sub>n-1</sub>Pb<sub>n</sub>I<sub>3n+1</sub> perovskite crystal structure.<sup>76</sup> The NMA<sup>+</sup> organic spacer suppressed ion-migration by inhibiting the diffusion of MA<sup>+</sup> ions during device operation which act as non-radiative recombination centres. The champion device (n=60) exhibited a high PCE value of 17% mainly due to improvements in V<sub>oc</sub> (1.0V) and FF (78%) with negligible hysteresis. The increase in V<sub>oc</sub> is related to the passivation of defects by the organic spacer which acts as a blocking layer for ion-migration. The thermal stability of the encapsulated champion device (n=60) was tested at elevated temperature of 85°C and it showed enhanced improvement of the device thermal stability by retaining 70% of its initial efficiency after 360 hours compared to the 3D device which dropped to 25% of its initial PCE under the same testing conditions.

Recently, Ansari et al. employed azetidinium lead iodide (AzPbI<sub>3</sub>) as a quasi-3D layer on top of the primary 3D perovskite film.<sup>77</sup> This buffer layer between the 3D perovskite and hole transport layer (HTL) resulted in passivating surface and grain boundaries defects. Using Kelvin probe force microscopy (KPFM), it was found out AzPbI<sub>3</sub> has a higher work function than the 3D reference film due to the formation of an electric field by Az cations as a result of surface dipoles. This electric field enhanced charge carrier extraction to the HTL by repelling negative electrons and attracting holes. Therefore, non-radiative recombination centres were suppressed at the perovskite/HTL interface and high V<sub>oc</sub> values were achieved. The champion device (5mg/ml) achieved a remarkable PCE value of 22.03%, a high V<sub>oc</sub> of 1.18 V, J<sub>sc</sub> of 24.55 mA/cm<sup>2</sup> and FF of 79% with negligible hysteresis. The unencapsulated champion device retained over 85% of its initial efficiency in a nitrogen atmosphere under 1 sun illumination at a constant load of 200 Ω at 52°C for over 1000 h, whereas the reference device maintained 47% of its original efficiency under the same conditions.

#### 4. Research aims

Among the many reported defect-passivation techniques, applying surface treatments to perovskite thin films have been found to mitigate efficiently non-radiative pathways and improve their optoelectronic properties.<sup>48,62</sup> Tailoring 3D perovskite materials through compositional engineering using a large organic cation with a low dimensionality as surface treatment, has led to impressive device performances and long-term operational stabilities.<sup>78,79</sup> In particular, recent studies on guanidinium ( $\text{GA}=\text{CH}_6\text{N}_3^+$ ) additives have shown promising results in reducing defect densities and achieving optimal performance.<sup>80–84</sup> Guanidinium iodide (GAI) is a relatively large organic compound composed of three amino groups ( $-\text{NH}_2$ ) with an ionic radius of  $\sim 278$  nm that has been proposed to form low-dimensional perovskites when reacted with excess  $\text{PbI}_2$  present on the 3D perovskite film surface.<sup>85–87</sup> The amino groups are proposed to strengthen the hydrogen-bond formation between the metal halide framework and A-site cation which would help to maintain the structure stability. Compounds with amino groups have been implicated in passivating surface defects (i.e., point defects) and defective grain boundaries.<sup>88,89</sup> Chavan *et al.* demonstrated highly efficient mixed-cation  $\text{Cs}_x\text{FA}_{1-x}\text{PbI}_3$  perovskite films through post-treatment deposition of GAI, delivering a stabilized power output of 19.73% with an enhanced  $V_{\text{OC}}$  value of 1.17 V.<sup>90</sup> It is worth mentioning that the careful doping of GAI into mixed-cation mixed-halide perovskite precursor  $\text{Cs}_{0.05}(\text{MA}_{0.17}\text{FA}_{0.83})_{0.95}\text{Pb}(\text{I}_{0.83}\text{Br}_{0.17})_3$  resulted in prolonged carrier lifetimes and lower trap densities.<sup>80</sup> These studies promise Guanidinium-cation based perovskite devices as an attractive candidate for efficient PSCs. However, a comprehensive investigation into the effect of GAI treatment on the optoelectronic properties of halide perovskite films is yet to be performed. In this work, the impact of a GAI surface treatment on the structural and photophysical properties of triple-cation  $\text{CsMAFA}$  perovskite films was analysed. The results suggest that a low-concentration treatment with GAI enhances the  $\text{CsMAFA}$  perovskite crystallinity, homogenizes the PL intensity, and improves the device performance. While, on the other hand, excess GAI yields low degree of crystallization leading to poor device performance.

## 5. Methodology

### 5.1. Device and materials fabrication methods

Unless otherwise specified, all materials were purchased from Greatcell Solar Materials, Alfa Aesar and Sigma-Aldrich and used as received without any further purification. Formamidinium iodide (FAI), methylammonium bromide (MABr) and guanidinium iodide (GAI) were purchased from Greatcell Solar Materials, lead iodide ( $\text{PbI}_2$ ) and lead bromide ( $\text{PbBr}_2$ ) were purchased from Alfa Aesar, cesium iodide (CsI), dimethylformamide (DMF), dimethylsulphoxide (DMSO), chlorobenzene (CBZ) and iso-propanol (IPA) were purchased from Sigma-Aldrich. Spiro-OMeTAD was purchased from Luminescence Technology Corporation. Fluorine-doped tin oxide (FTO) glass substrates of 8  $\Omega/\text{sq}$  sheet resistance were purchased from Zhuhai Kaivo Optoelectronic technology corporation.

FTO-coated glass substrates were cleaned by ultrasonication in 2% (volume ratio) Hellmanex aqueous solution, de-ionized water, ethanol and iso-propanol in sequence (20 min each) followed by a UV plasma cleaner treatment for 10 min.

A compact  $\text{TiO}_2$  blocking layer (65 nm thickness) was deposited onto FTO substrates with an automatic spray pyrolysis system using a titanium diisopropoxide bis(acetylacetonate) solution dissolved in anhydrous iso-propanol (1:19, v/v). The substrates were sintered on a hot plate at 500 °C for 20 min and left to cool down to room temperature.

Then, 80  $\mu\text{L}$  of diluted  $\text{TiO}_2$  paste in ethanol (1:6 weight ratio) was deposited on the compact  $\text{TiO}_2$  layer by spin-coating at 4000 rpm at a ramping speed of 2000 rpm for 20 s followed by drying of each substrate at 100 °C for 10 min then sintering at 500 °C for 30 min in air. The substrates were treated again with a UV plasma cleaner for 10 min and transferred immediately to a  $\text{N}_2$ -filled glovebox for perovskite deposition.

For the  $\text{Cs}_{0.07}\text{FA}_{0.79}\text{MA}_{0.14}\text{Pb}(\text{I}_{0.83}\text{Br}_{0.17})_3$  ("CsMAFA") perovskite film fabrication, the perovskite precursor solution was prepared in a  $\text{N}_2$ -filled glovebox by mixing 1.12M  $\text{PbI}_2$ , 1.1M FAI, 0.19M MABr and 0.2M  $\text{PbBr}_2$  powders in 1mL of DMF and DMSO (4:1 v/v) with a final concentration of 1.4M. The solution contains 3 mole % excess  $\text{PbI}_2$ . 34  $\mu\text{L}$  of CsI dissolved in DMSO (1.5 M) was then added to the precursor solution. The perovskite precursor was left to stir overnight until fully dissolved. The CsMAFA film was prepared by spin coating 50  $\mu\text{L}$  of the CsMAFA precursor solution onto the substrates using a two-step program at 1000 rpm with a ramping speed of 1000 rpm for 10 s and then, 6000 rpm with a ramping speed of 6000 rpm for 20 s. 200  $\mu\text{L}$  of CBZ was poured onto the substrate 5 s prior to the end of the second step. The substrates were then annealed at 100°C for 30 mins.

After cooling, 35  $\mu\text{L}$  of solution of GAI dissolved in IPA at different concentrations was deposited at 5000 rpm with a ramping speed of 5000 rpm for 30 s.



For the hole transport layer stock solution, 72.5 mg of spiro-OMeTAD was dissolved in CBZ, followed by the addition of 28.8  $\mu\text{L}$  tBP and 17.5  $\mu\text{L}$  of LiTFSi (300 mg/ml) in Acetonitrile (ACN) was added. The film was spin coated onto the GAI/CsMAFA film at a ramping speed of 4000 with an acceleration of 4000 rpm for 20 s.

Finally, the device fabrication was completed by depositing 80 nm thin layer of Au electrode using thermal evaporation.

To enable correlation between experiments, Au fiducial markers were prepared according to the modified procedure reported by Jone et al.<sup>91</sup>. The Au markers were suspended in chlorobenzene and spin-coated at 1000 rpm with a ramping speed of 1000 rpm for 60s. This resulted in the formation of triangular shaped markers that are a few micrometres in size, and the measurements were taken away from these nanoparticles for correlation between experiments.

## **5.2. Device characterizations**

### **5.2.1 Current-Voltage (J-V) Characteristics**

J-V curves were measured using a Keithley 2400 source meter. The devices were illuminated by an Oriel solar simulator equipped with a Xenon lamp source (100  $\text{mw}/\text{cm}^2$ ) and an AM1.5G filter. A non-reflective metal mask of aperture 0.16  $\text{cm}^2$  was used to define the irradiation area.

### **5.2.2 Ultra-violet visible (UV-Vis) spectra**

UV-Vis spectra were obtained using a Perkin Elmer Lambda 950 spectrophotometer fitted with an integrating sphere. The perovskite films were spin-coated onto Plain glass before measurement. The UV-Vis spectra were measured using a quartz cuvette that can be fully sealed. The UV-Vis spectra were measured by Dr. Anthony Chesman.

### **5.2.3 Photoluminescence (PL) and time-resolved PL measurements**

Spectral and PL decay measurements were performed using an Edinburgh Instruments Ltd. FLSP920 time-correlated single-photon counting (TCSPC) spectrometer. A 466 nm pulsed diode laser excitation source (EPL-475, Edinburgh Instruments Ltd.) with ca 100 ps pulse width and a peak laser-pulse excitation fluence of ca 0.2  $\text{nJ}/\text{cm}^2$ , operating at 20 kHz, was used as the excitation source. Emission was measured using a grating monochromator. The PL spectra was measured using a sufficiently low repetition rate to allow the PL to decay to negligibly low levels between consecutive pulses. Very low excitation fluences (0.2  $\text{nJ}/\text{cm}^2$ ) were used for the PL decay measurements to specifically probe the extent of non-radiative recombination at traps/defects in pristine perovskite layers (slow decay component), as well as rates of charge-transfer between perovskite and charge-transport layers in bi/multi-layer systems (fast decay component). These results cannot be readily extrapolated to PL decay behaviour at the much higher fluences equivalent to 1-sun where the decay kinetics is much more complex due to bi-molecular

recombination, Auger recombination etc. Samples consisted of films coated on plain glass substrate, with excitation incidence and emitted PL measured on the coated side of the samples. The PL measurements were done by Dr. Andrew Scully.

#### 5.2.4 Contact Angle measurements

Contact angle measurements were conducted using OCA 20 from dataphysics equipped with high quality optics to ensure high precision when displaying the drop, to accurately measure the contact angle. 2 $\mu$ L of milk q water was used for the measurements.

#### 5.2.5 X-ray diffraction analysis (XRD)

XRD measurements was carried out with a Bruker D8 Advance Diffractometer using Cu K $\alpha$  X-ray tube operated at 40 kV and 40 mA.

#### 5.2.6 Scanning electron microscopy (SEM) micrographs

SEM micrographs were obtained using a FEI Nova NanoSEM 450 FEG microscope at 3kV accelerating voltage and acquired with a Through-Lens Detector (TLD). The samples were transferred via inert gas transfer chamber. The dwell time for image acquisition was 20  $\mu$ s per probe pixel.

#### 5.2.7 Confocal PL spectroscopy and imaging measurements

Confocal PL measurements were performed on an inverted microscope (Nikon Eclipses Ti2 microscope) with a Kymera detector (mode: 328i). The excitation light is generated by a mercury lamp with a 488 nm long pass filter for the confocal PL imaging and time-dependent PL spectra. The confocal data were acquired by Dr. Wenxin Mao.



## 6. Results and Discussion

### 6.1. Structural analysis of the GAI-treated PSCs

In the present study, a mixed-cation mixed-halide  $\text{Cs}_{0.07}\text{FA}_{0.79}\text{MA}_{0.14}\text{Pb}(\text{I}_{0.83}\text{Br}_{0.17})_3$  perovskite (referred to as CsMAFA; FA; formamidium; MA, methylammonium; Cs, cesium) was employed as the baseline perovskite composition. The films were prepared using a single-step deposition method<sup>92</sup> (**Figure 36a**), followed by the introduction of different concentrations of GAI dissolved in IPA solvent acting as a surface treatment: 2 mg/ml (GAI-2), 10 mg/ml (GAI-10), 20 mg/ml (GAI-20), 30 mg/ml (GAI-30) and 40 mg/ml (GAI-40). GAI is a relatively large organic compound composed of three amino groups ( $-\text{NH}_2$ ) with an ionic radius of  $\sim 278$  nm; the amino group is proposed to strengthen the hydrogen-bond formation with the undercoordinated iodine species of the perovskite film, which would help to passivate surface defects and defective grain boundaries.<sup>93,88</sup>

XRD measurements were performed on the perovskite films to study the formed phases and film crystallinity induced upon GAI treatment (**Figure 36b**). The typical 001, 011, 111 and 002 perovskite peaks corresponding to the metrically cubic phase of mixed-cation mixed-halide composition were present in all the films (note that due to the nominally irrational stoichiometry, the structure cannot have a cubic space group).<sup>94</sup> The CsMAFA perovskite film shows a hexagonal  $\text{PbI}_2$  peak at  $12.646^\circ$  and this was expected since the precursor solution contains a 3 mole % excess  $\text{PbI}_2$ . For all the GAI-treated films, the  $12.646^\circ$  peak disappears, and a new peak just to the right of it was observed. The values for this new peak were  $12.712^\circ$ ,  $12.959^\circ$ ,  $12.972^\circ$ ,  $12.979^\circ$  and  $12.979^\circ$  for GAI-2, GAI-10, GAI-20, GAI-30, and GAI-40, respectively. This peak shift is large and cannot be attributed to pure  $\text{PbI}_2$  since there are no polytypes of hexagonal  $\text{PbI}_2$  that can generate an XRD peak at these higher angles.<sup>95</sup> Moreover, the possibility that this peak can be assigned to a lead-halide ( $\text{PbI}_x\text{Br}_{100-x}$  or  $\text{PbBr}_2$ ) phase was considered, as demonstrated in **Figure 36d**, however, the spectra was not consistent with the shifted peak and additionally was excluded for two reasons: first, more iodide ions are added upon GAI treatment which would result in a peak shift to the left of  $\text{PbI}_2$  peak instead of the right and second, it is not chemically plausible that the reaction of GAI with excess  $\text{PbI}_2$  would lead to the appearance of a  $\text{PbBr}_2$  or  $\text{PbI}_x\text{Br}_{100-x}$  phase.

In a further effort to identify the phases associated with this shifted peak and all the other peaks in the XRD spectra of the GAI treated CsMAFA that are not found in the pure CsMAFA, XRD spectra of several compositions that could possibly form were analyzed such as  $(\text{FAPbI}_3)_x(\text{GA}_2\text{PbI}_4)_{100-x}$  (hereafter called “FAGA” phases),  $\text{PbI}_x\text{Br}_{100-x}$  and  $\text{GAPb}(\text{I}_x\text{Br}_{100-x})_3$  as shown in **Figure 36(c-e)**. These films were synthesized using the same solvents and processes for the CsMAFA and GAI-treated films.

The rationale for analyzing FAGA phases is because the CsMAFA perovskite system is mostly composed of FA therefore it is highly probably that GAI will react with FA if GAI is

incorporated into the CsMAFA perovskite lattice. Indeed, the exact composition may be slightly different, incorporating Cs, MA and Br, but the XRD of the FAGA phases is useful as a starting reference. At  $x=70$  ((FAPbI<sub>3</sub>)<sub>70</sub>(GA<sub>2</sub>PbI<sub>4</sub>)<sub>30</sub>), a peak at 12.692° starts to appear and then it shifts gradually to the right with more GAI incorporation relative to FA till it reaches 12.999 for  $x=10$  ((FAPbI<sub>3</sub>)<sub>10</sub>(GA<sub>2</sub>PbI<sub>4</sub>)<sub>90</sub>) similar to the observed trend for the GAI-treated CsMAFA films. **Table 1** highlights all the values for the peak angles for the different FAGA compositions. Therefore, this “shifting” peak might be associated with a FAGA phase, shifting with increasing GAI.

The XRD spectra of GAPb(I<sub>x</sub>Br<sub>100-x</sub>)<sub>3</sub> was observed as well and no peaks between 12° and 14° were found across all compositions that could match the observed peaks in this range, suggesting this phase is not formed.

Furthermore, after comparing the XRD patterns of the GAI-treated films with the pattern of  $\delta$ -FAPbI<sub>3</sub> (at  $x=100$ ), and observing the presence of the two  $\delta$ -FAPbI<sub>3</sub> peaks at 11.5° and 25.5° for all the GAI-treated samples, these two peaks can be attributed to  $\delta$ -FAPbI<sub>3</sub>.

Meanwhile, at higher GAI concentrations (GAI-30 and GAI-40), a low-angle diffraction peak consistent with (FAPbI<sub>3</sub>)<sub>x</sub>(GA<sub>2</sub>PbI<sub>4</sub>)<sub>100-x</sub> phases (for  $x=0$  to 50) was observed at 6.5°. GAI-40 also exhibits some additional low intensity peaks that we have not been able to identify from the studied (FAPbI<sub>3</sub>)<sub>x</sub>(GA<sub>2</sub>PbI<sub>4</sub>)<sub>100-x</sub> or other patterns. Others have suggested these are consistent with the key characteristic peaks of GA<sub>2</sub>PbI<sub>4</sub>.<sup>96,97</sup> These results suggest that the introduction of GAI induces the formation of different (FAPbI<sub>3</sub>)<sub>x</sub>(GA<sub>2</sub>PbI<sub>4</sub>)<sub>100-x</sub> (or closely related) phases, with the specific phase ( $x$ ) depending on the GAI concentration, implying the reaction of GAI with the CsMAFA perovskite lattice.

All the peak values for the CsMAFA, GAI-treated and (FAPbI<sub>3</sub>)<sub>x</sub>(GA<sub>2</sub>PbI<sub>4</sub>)<sub>100-x</sub> films are provided in **Table 2** and **Table 3**, respectively.

The full width at half-maximum (FWHM) of the 001 perovskite peak was analyzed to determine the crystallinity of the perovskite phase (**Figure 36d**). The GAI-10 film has the sharpest diffraction peak with the smallest FWHM in comparison to the other films, which implies enhanced ordering of the perovskite crystal lattice for this exact GAI concentration.

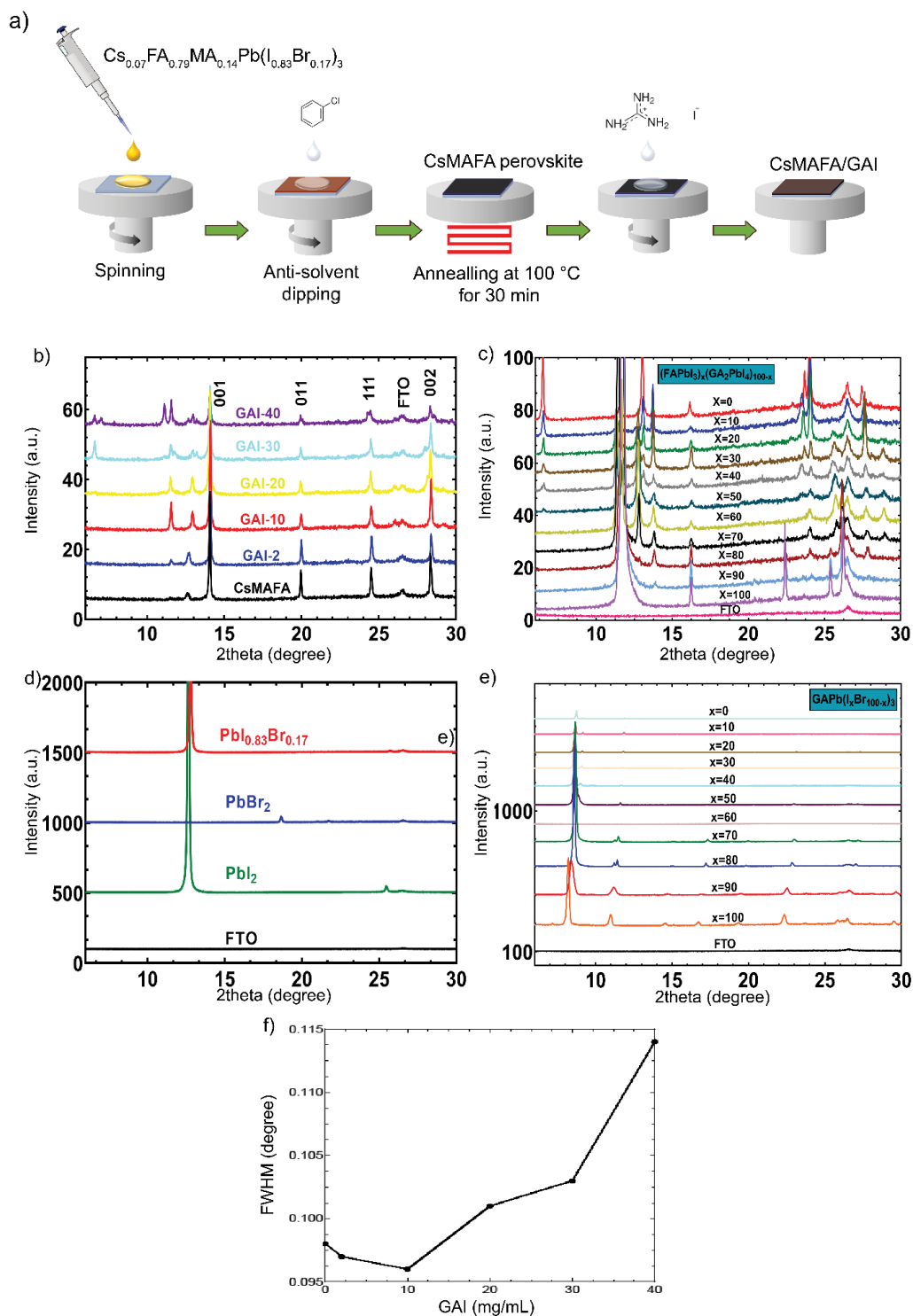


**Figure 36.** a) Schematic diagram of the perovskite film fabrication, b) XRD patterns for the CsMAFA and GAI-treated films, c) XRD spectra for the different  $\text{FAPbI}_3$  and  $\text{GA}_2\text{PbI}_4$  compositions, d) XRD spectra for Pb-halides, e) XRD spectra for  $\text{GAPb}(\text{I}_x\text{Br}_{100-x})_3$  and f) FWHM of the 001 perovskite peak at  $14.1^\circ$ .

**Table 1.** Angles of the ~12.6-12.9 degree peak as a function of different concentrations of  $(\text{FAPbI}_3)_x(\text{GA}_2\text{PbI}_4)_{100-x}$ .

<b>X</b>	<b>Peak shift values in degrees</b>
10	12.999
20	12.979
30	12.938
40	12.897
50	12.835
60	12.815
70	12.692
80	No peak
90	No peak
100	No peak

**Table 2.** Peak position in degrees for the CsMAFA and GAI-treated films.

<b>GAI (mg/ml)</b>	<b>Peak position in degrees</b>
0	12.646, 14.005, 19.891, 24.712, 28.281, 26.532 (FTO)
2	11.523, 12.712, 14.005, 19.891, 24.712, 26.532 (FTO), 28.301
10	11.420, 12.959, 14.004, 19.889, 24.556, 26.111, 26.532 (FTO), 28.444
20	11.222, 11.420, 12.972, 14.003, 19.889, 24.444, 26.000, 26.532 (FTO), 28.333
30	6.5, 11.111, 11.420, 12.979, 13.333, 14.001, 19.889, 24.333, 26.000, 26.532 (FTO), 28.222
40	6.5, 7.000, 11.000, 11.420, 12.979, 13.000, 14.000, 19.889, 24.333, 26.111, 26.532 (FTO), 28.111

**Table 3.** Peak position in degrees for various concentrations of  $(\text{FAPbI}_3)_x(\text{GA}_2\text{PbI}_4)_{100-x}$ .

X	Peak position in degrees
0	6.532, 11.444, 13.000, 13.778, 16.111, 23.556, 24.000, 26.532 (FTO), 27.556
10	6.532, 11.444, 12.667, 12.999, 13.778, 16.111, 23.556, 24.000, 26.532 (FTO), 27.667
20	6.519, 11.326, 11.571, 12.671, 12.979, 13.730, 16.215, 23.589, 24.078, 25.504, 26.532 (FTO), 27.582
30	6.497, 11.315, 11.596, 12.938, 13.122, 13.724, 16.254, 23.642, 24.084, 25.649, 26.532 (FTO), 27.657, 28.902
40	6.457, 11.275, 11.676, 12.847, 13.162, 13.724, 16.254, 23.481, 24.084, 25.529, 26.532 (FTO), 27.737, 28.902
50	6.416, 11.275, 11.717, 12.835, 13.485, 16.294, 23.481, 24.084, 25.649, 26.131, 26.532 (FTO), 27.737, 28.902
60	11.355, 11.676, 12.815, 13.764, 16.254, 24.003, 25.730, 26.131, 26.532 (FTO), 27.737, 28.902
70	11.413, 11.700, 12.692, 13.789, 16.206, 23.974, 25.776, 26.145, 26.532 (FTO), 27.743, 28.931
80	11.754, 13.803, 16.236, 22.424, 24.046, 25.412, 26.137, 26.532 (FTO), 27.802
90	11.780, 13.902, 16.236, 22.389, 24.171, 25.402, 26.208, 26.532 (FTO)
100	11.780, 16.236, 22.432, 25.402, 26.251, 26.532 (FTO)

With a closer inspection at the 001 and 002 perovskite peaks, a peak shift towards lower angles was observed (**Figure 37**). According to Bragg's law, a lower angle shifted peak confirms the expansion of the unit cell, contributing to larger d-spacings, which in this instance could be due to the incorporation of either guanidium or iodide ions.

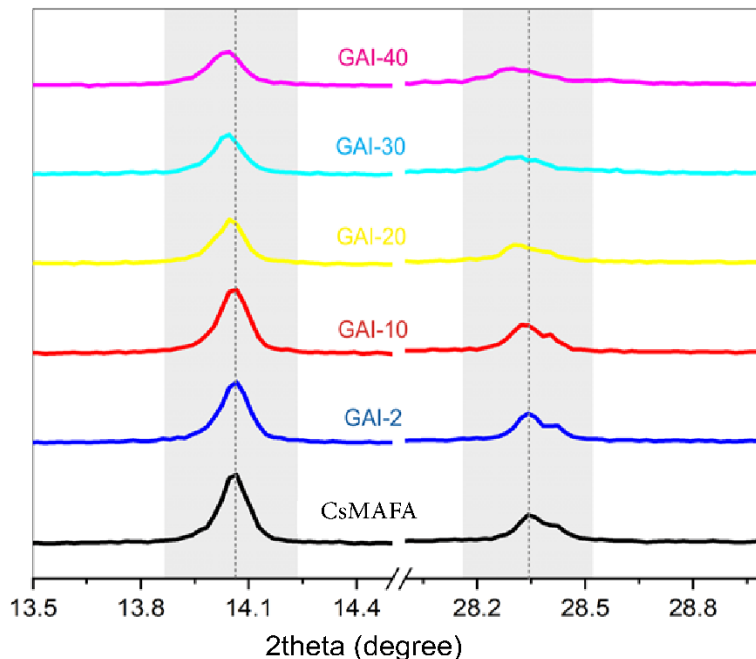


**Figure 37.** Zoomed-in XRD patterns for the 001 and 002 perovskite peaks.

## 6.2. The impact of GAI treatment on the photophysical properties of the perovskite films

Despite the exceptional PCEs reported for CsMAFA perovskite systems, they still suffer from substantial microscale variations in terms of luminescence efficiency.<sup>38,42</sup> In order to further investigate the variations in the PL intensities at the micron scale, confocal PL microscopy was used to map the luminescence intensities of the untreated and GAI-10 treated films (

**Figure 38b**). The PL sample was marked with Au fiducial markers to allow the exact area to be scanned before and after deposition of the GAI passivation layer (**Inset**

**Figure 38b and e**). As shown in

**Figure 38a**, the confocal PL mapping highlights the spatial luminescence heterogeneity featuring dark regions for the reference CsMAFA film. Some hypotheses for these dark defective spots are as follows: 1) iodide vacancies (undercoordinated  $\text{Pb}^{+2}$  and  $\text{Pb}^0$  defects) formed upon thermal annealing due to the volatility of organic components.<sup>100,101</sup> 2)  $\text{PbI}_2$  crystals present on the film surface arising during film growth and crystallization.<sup>91</sup> 3) different crystal facets with different density of trap states.<sup>102</sup> 4) phase impurities existing at the grains' interfaces as reported by Doherty *et al.*<sup>94</sup>. However, upon the introduction of GAI-10 surface treatment, we obtained homogeneous PL intensities over the entire film and no dark defective regions were observed (

**Figure 38d**). Our interpretation is that GAI induces a homogeneous crystallization phase for the CsMAFA film leading to uniformity in the PL emission. Furthermore, since  $\text{PbI}_2$  is a wide band-gap photoactive material ( $\sim 2.4$  eV) with a strong PL emission at 513 nm and taking into consideration the emission range of the fluorescence mapping is

between 510 nm to 900 nm.<sup>103,104</sup> Therefore, we speculate that the dark spots are most likely  $\text{PbI}_2$  crystals since GAI is expected to react with  $\text{PbI}_2$  particles to form different GAI phases. The associated PL signals were taken before and after each fluorescence image, and we observe no shift in the PL peak ensuring the absence of halide segregation due to the low bromide content (

**Figure 38c and f).** These non-luminescent defects impact not only the device performance by promoting non-radiative recombination of charge-carriers but also degrade the long-term operational stability.<sup>105</sup> Therefore, resolving micro-scale inhomogeneities and achieving uniform optoelectronic properties is paramount for efficient device operation, a common view among researchers studying monocrystalline semiconductor materials.<sup>106,107</sup>

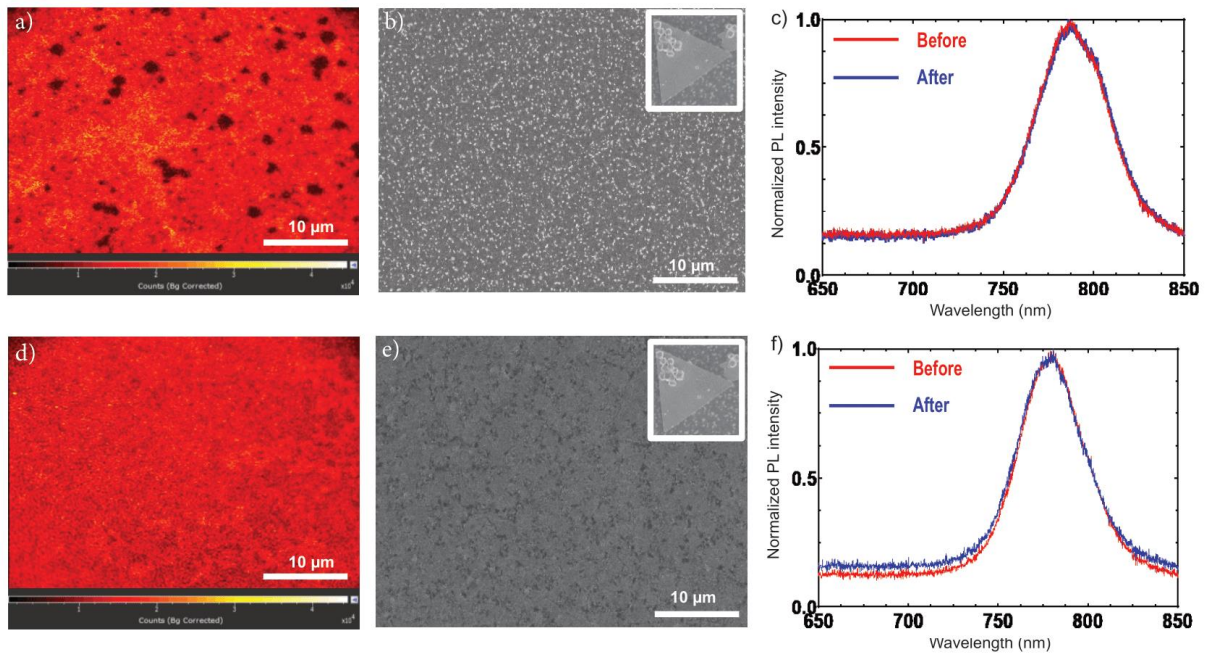


**Figure 38.** Confocal PL mapping for the reference and GAI-10 films marked with Au fiducial markers as shown in the corresponding SEM images: a & b) Fluorescence and SEM micrograph of the CsMAFA film, d & e) Fluorescence and SEM micrograph of the GAI-10 film c & f) Normalized PL spectra for the films before and after each fluorescence mapping. The laser excitation wavelength is 488 nm and the emission range is between 510 to 900 nm.

**Figure 39** shows the evolution of the confocal PL spectra as a function of time for both the CsMAFA and GAI-10 treated films. The CsMAFA film shows a reduced PL intensity over different time intervals compared to the treated film and started to display a shoulder at 795 nm (as marked by the arrow) suggesting the occurrence of halide segregation at 50s.<sup>108,109</sup> Notably, there could exist a small unpronounced shoulder at

t=1s, however, it becomes clearly visible at t=50s. This phase segregation could be attributed to an iodide rich domain since it starts to appear at longer wavelengths. Whereas the GAI-10 treated film exhibited stronger and sharper PL intensities over time confirming enhanced radiative quality as well as suppression of halide-migration. A possible explanation for this behaviour is that upon continuous illumination, the amine group of GAI fills the trap states (i.e. undercoordinated iodide species) by the passivation of surface and grain boundaries defect sites, thereby yielding higher PL peak over time. It also correlates with  $V_{OC}$  improvements at the device level in which higher radiative efficiency leads to larger quasi-fermi level splitting in the bandgap.<sup>110,111</sup> These results indicate the GAI treatment provided enhanced photophysical properties and lower defect densities.

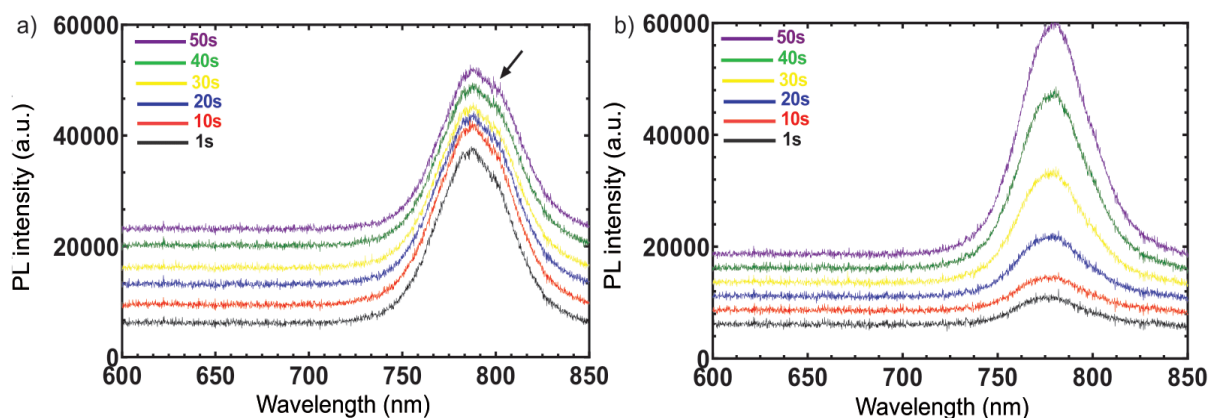


**Figure 39.** Time-dependent confocal PL spectra of the perovskite films: a) CsMAFA and b) GAI-10. The arrow highlights the rise of a segregated PL peak for the CsMAFA film.

### 6.3. Opto-electronic and morphological characterization of the perovskite films

In

**Figure 40**, the effect of different concentrations of GAI treatment on the optical properties of the perovskite films was investigated. UV-Vis spectroscopy was performed to study the optical absorption spectra of the films (

**Figure 40a**). The reference and GAI-2 films have an absorption onset at 787 nm (1.58 eV) indicating the band gap of the bulk perovskite is not noticeably affected at this low concentration of GAI. However, the higher concentrations of GAI-modified films were slightly red-shifted, indicating a reduction in the band gap. This redshift may be related to the introduction of iodide-rich perovskite phases with more GAI incorporation into the perovskite lattice. It is worth noting that the absorption intensity was significantly reduced, especially in the wavelength region from 600 to 750 nm at GAI-20, GAI-30 and GAI-40, while the reference, GAI-2 and GAI-10 films have a high absorption capacity over the entire visible spectrum. To unravel the effect of the GAI treatment on the emissive properties of the films, PL measurements were carried out on plain glass substrates using a laser with an excitation wavelength of 466 nm (



**Figure 40b).** It can be clearly seen that the PL intensity gradually increases with more GAI content. These improved PL features infer the excellent radiative quality of the treated films. It also demonstrates the suppression of defects and promotion of radiative charge recombination.

TRPL was used to characterize the charge carrier dynamics of the perovskite films with and without GAI surface treatment. The PL decay curves are shown in

**Figure 40c** and the data were fitted using a bi-exponential decay function:

$$I(t) = A_1 \exp(-t/\tau_1) + A_2 \exp(-t/\tau_2)$$

The PL decay kinetics comprises a fast ( $\tau_1$ ) and a slow ( $\tau_2$ ) component.<sup>112,113</sup> The fast decay component relates to non-radiative recombination, while the slow decay component attributes to radiative recombination of charge carriers.<sup>114</sup> From the TRPL data, the weighted average lifetime values of the films increase dramatically with the treatment of GAI from 0.11  $\mu$ s for the control film to 0.12, 1.39, 3.66, 4.99 and 5.24  $\mu$ s for GAI-2, GAI-10, GAI-20, GAI-30 and GAI-40 respectively. The prolonged lifetimes indicate the reduction of trap states upon GAI treatment.

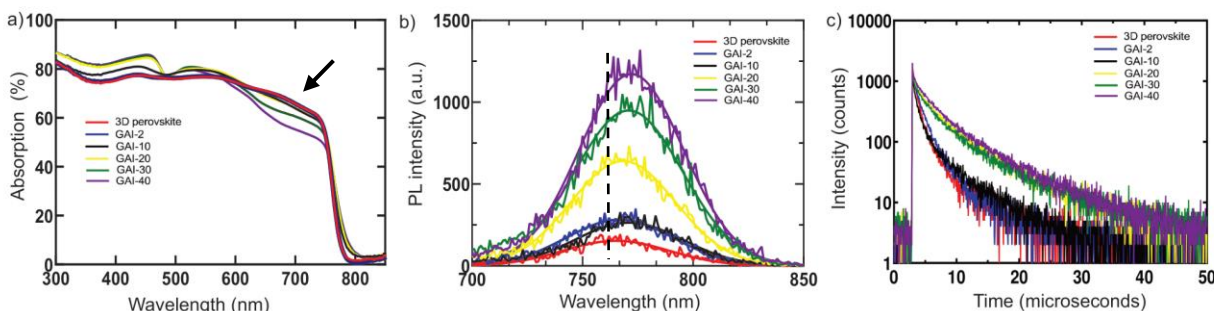


**Figure 40.** Characterization of the perovskite films: a) UV-Vis absorption (the arrow highlights the reduced absorption intensity for higher GAI concentrations), b) Steady-state PL spectra, c) TRPL decay curves of the perovskite films.

The morphology of the films was examined using scanning electron microscopy (SEM) as shown in

**Figure 41.** The CsMAFA film exhibits a compact, dense and pin-hole free morphology distributed homogeneously among the substrate with average grain dimensions of 200 – 250 nm (

**Figure 41a).** There exist small bright grains which are attributed to unreacted-PbI<sub>2</sub> on top of the film.<sup>115,116</sup> To elucidate the role of the solvent on the CsMAFA film surface, the perovskite film was treated with neat IPA (

**Figure 41b).** The resulting morphology suggests that the neat solvent on its own did not modify the film surface and remained unchanged. When the CsMAFA film was treated with GAI-2 and GAI-10, GAI started to react with the excess  $\text{PbI}_2$  demonstrated by the reduction in the density of bright grains, and the average grain sizes increased to 300 and 400 nm (

**Figure 41c and d).** Larger grains mean fewer grain boundaries, which is beneficial for charge transport in devices. GAI-10 also appears to have a slightly smoother surface than the other prepared films. When the concentration of GAI is further increased to 20, 30 and 40 mg/ml, the grains reduce again in size featuring plate-like structures and the surface appears rougher (GAI-30) as shown in

**Figure 41(e-g),** respectively.

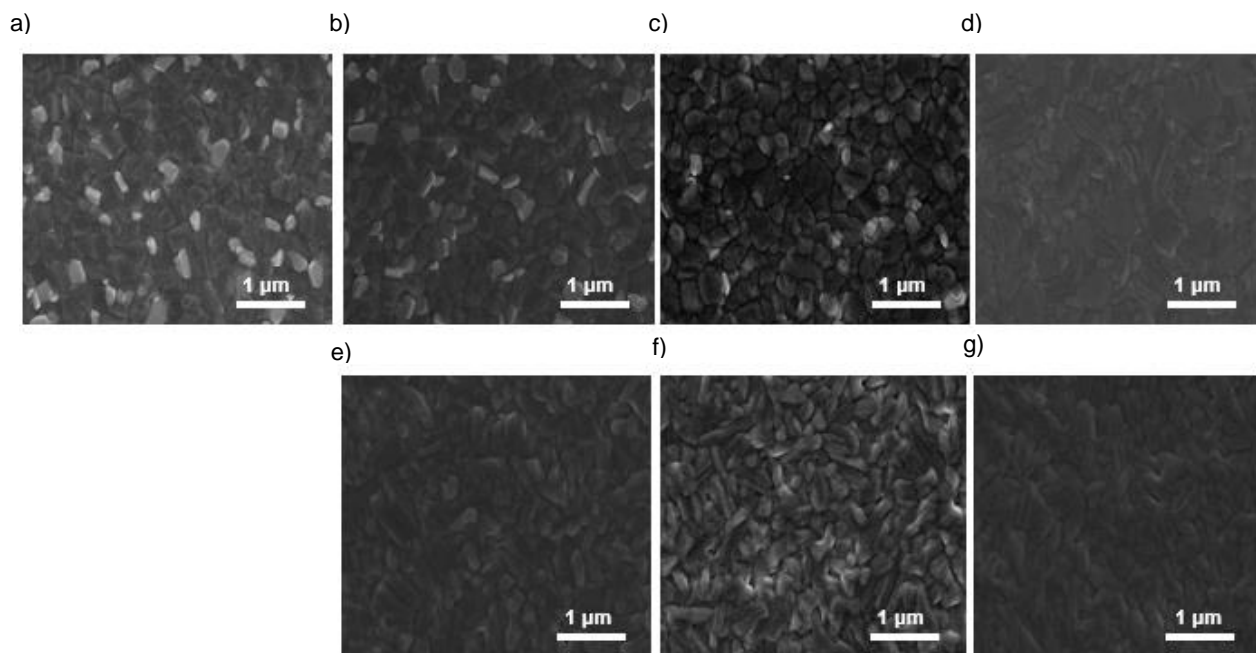


**Figure 41.** SEM micrographs of the perovskite films: a) CsMAFA, b) CsMAFA/IPA, c) GAI-2, d) GAI-10, e) GAI-20, f) GAI-30 and g) GAI-40.

#### 6.4. Resulting device performance of the GAI-treated PSCs

The elimination of the heterogeneous PL features with GAI-10 surface treatment was a motivation to investigate whether this homogenization would translate to improvements in device performance. The fabricated PSCs were based on an n-i-p architecture containing FTO/c-TiO<sub>2</sub>/m-TiO<sub>2</sub>/CsMAFA perovskite/GAI/Spiro-OMeTAD/Au as shown in **Figure 42a**. The effect of GAI-treatment on the J-V hysteresis phenomenon was examined as shown in **Figure 42b**. It was found that all the GAI-passivated films exhibit less hysteresis between the forward and reverse scans than the CsMAFA device, which could indicate the suppression of ion migration upon GAI treatment. However, the

hysteresis is a complex dynamical behaviour dependent on many factors such as scan rate/direction, ion-mobilities, device architecture and preconditioning ..etc, and these different factors cannot be easily isolated here.<sup>117</sup> Interestingly, a switch from normal hysteresis behavior (positive hysteresis values) for low GAI concentrations (2 and 10 mg/ml) to inverted hysteresis (negative hysteresis values) in high GAI concentrations (20, 30 and 40 mg/ml) was observed, which could be due to screening the built-in electric field by the large amount of positive ions accumulating the interface (

**Figure 43).** Normal hysteresis is often related to the migration of halide ions forming segregated iodide- or bromide-rich domains.<sup>118</sup> One of the possible explanations for the switch from normal to inverted hysteresis could be that the introduction of relatively higher amounts of positive ions at high GAI concentrations might result in their accumulation at the interface, screening the built-in electric field. This would lead to the creation of an opposing 'unfavourable' electric field at the interface that acts as an energetic barrier to charge extraction. The presence of S-shaped J-V curves also indicate the impairment of charge carrier collection efficiency at higher concentrations of GAI.<sup>119,120</sup>

The photovoltaic performance of the resulting PSCs was investigated under standard AM1.5G solar illumination at ambient conditions, and the device parameters were summarized in **(Figure 42(c-f))**. The best performance was achieved for GAI-10 devices; for these devices, the improved performance is mostly driven by an increase in  $V_{oc}$  and FF, with reproducible values of  $1.15 \pm 0.2$  V and  $75 \pm 2$  %, respectively, denoting an enhanced defect-passivation. These devices also yielded the highest PCE value of  $18 \pm 0.3$  %, while the CsMAFA devices delivered  $16 \pm 0.4$  % PCE. For the  $J_{sc}$  values, the CsMAFA film, GAI-2 and GAI-10 exhibited similar values of  $22 \pm 0.1$  mA/cm<sup>2</sup>. For GAI content beyond 10 mg/ml, the  $J_{sc}$  and fill factor values drop dramatically, limiting the overall device performance. This may arise from an increase in the charge transport series resistance as a result of increasing the concentration of this passivation treatment which has lower conductivity.<sup>61</sup>

These results show that a small amount of GAI can improve the film quality and suppress defects, while a larger amount degrades the device performance. They also demonstrate that the achieved homogenization of the PL intensities resulted in efficient device output. Additionally, these results highlight the importance for the need to precisely control the concentration of GAI treatment to obtain the desired device performance.

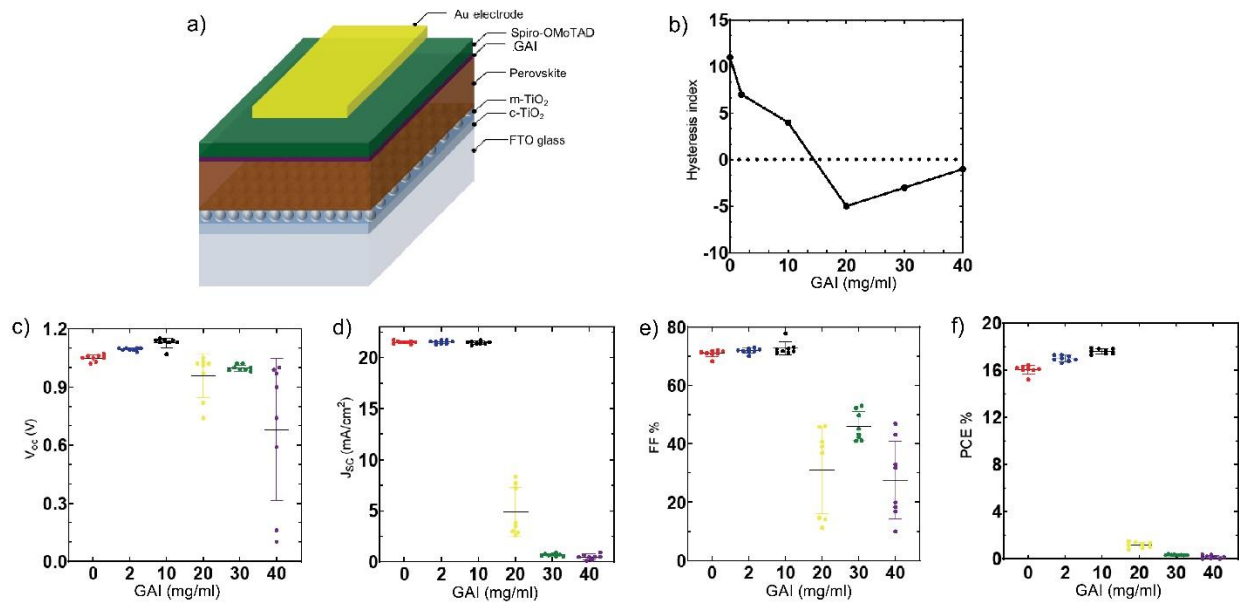


**Figure 42.** a) Schematic illustration of the employed planar device architecture, b) Hysteresis indices as a function of GAI concentrations, Statistical distribution of photovoltaic parameters: b)  $V_{OC}$ , c)  $J_{SC}$ , d) FF, and e) PCE for the devices made with CsMAFA perovskite and those modified with GAI.

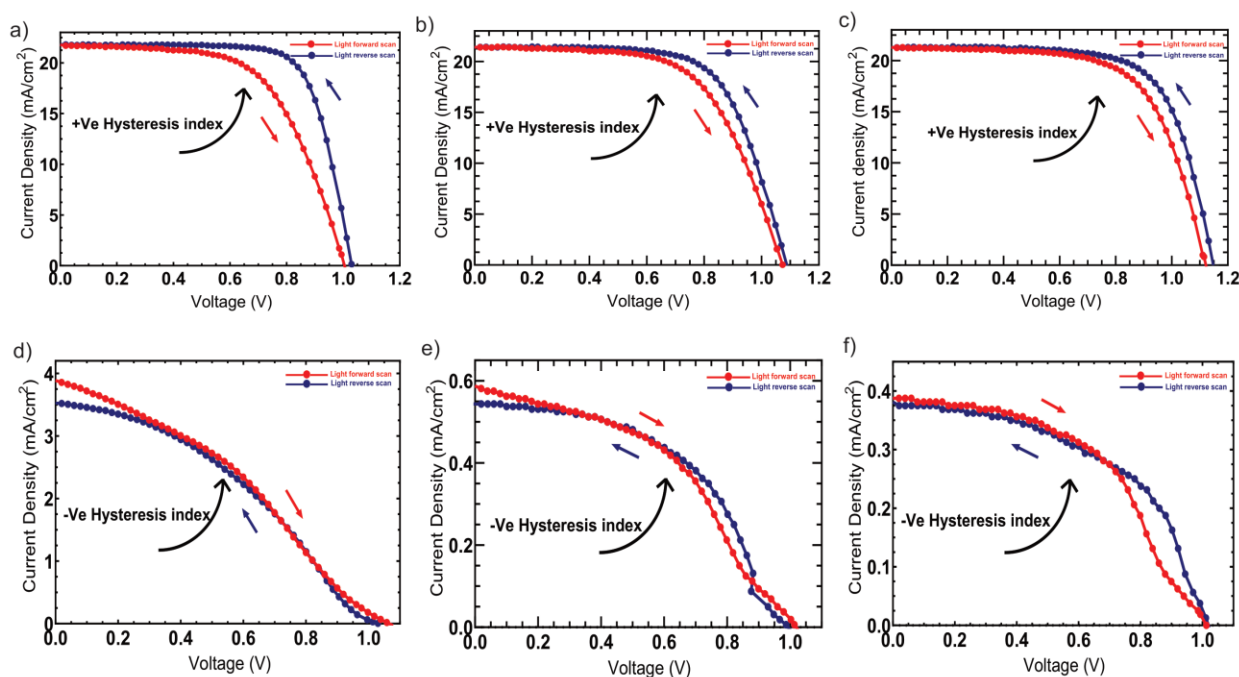


**Figure 43.** J-V curves at a scan rate of 0.1 V/s for all the devices featuring the hysteresis behavior: a) CsMAFA, b) GAI-2, c) GAI-10, d) GAI-20, e) GAI-30 and f) GAI-40.

The representative SEM cross section images of the full devices are presented in

**Figure 44**, showing the thickness of the individual layers. It visualizes unchanged perovskite thickness of around 450 nm for the CsMAFA and GAI-treated films.

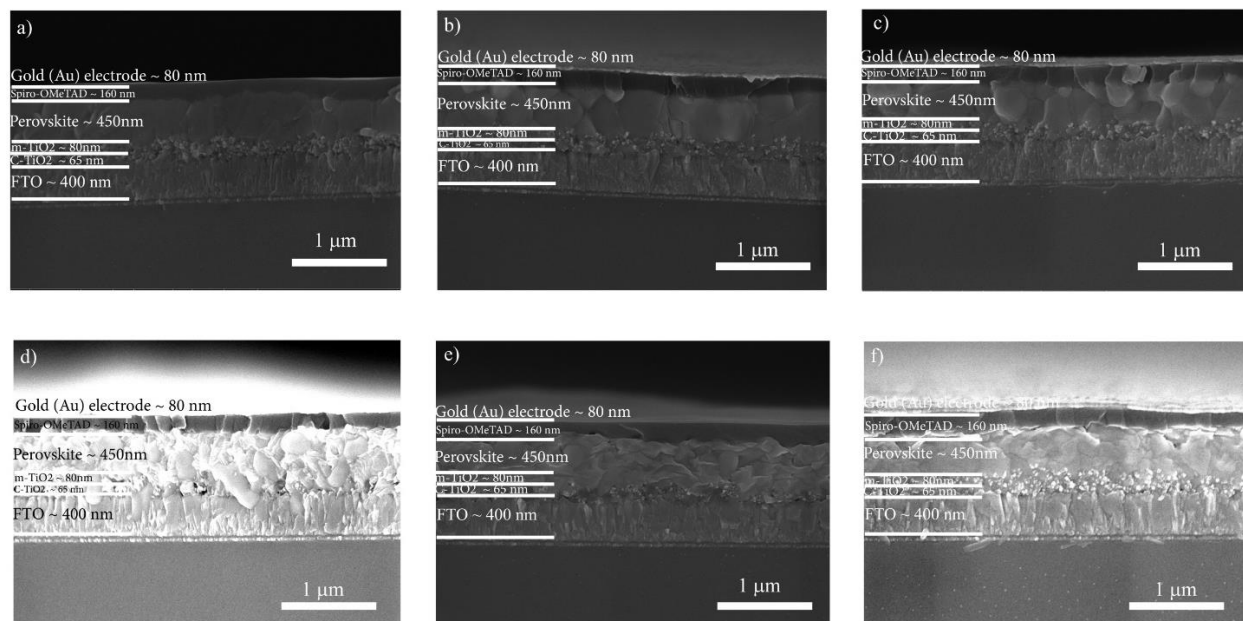


**Figure 44.** Cross-sectional SEM images for the fully assembled devices based on CsMAFA and GAI-treated films: a) CsMAFA, b) GAI-2, c) GAI-10, d) GAI-20, e) GAI-30 and f) GAI-40.

## 6.5. The detrimental effect of excess GAI on the device performance

To test the hypothesis that low conductivity of the passivation layer limits the device performance at higher GAI concentrations, an IPA cleaning step was introduced to remove any excess GAI at the surface of the CsMAFA perovskite film. The corresponding device performance metrics are shown in

**Figure 45.** The low-GAI treated devices (GAI-2 and GAI-10) did not experience any change in their performance upon the IPA washing step. However, the high-GAI treated devices (GAI-20, GAI-30 and GAI-40) displayed significant improvement in all the device performance metrics, specifically, in the  $J_{sc}$  values upon the removal of the excess unreacted GAI. These results suggest that excess GAI and/or  $(FAPbI_3)_x(GA_2PbI_4)_{100-x}$  phases, such as  $GA_2PbI_4$ , act as insulating layers that inhibit charge extraction, thereby leading to poor device performance.

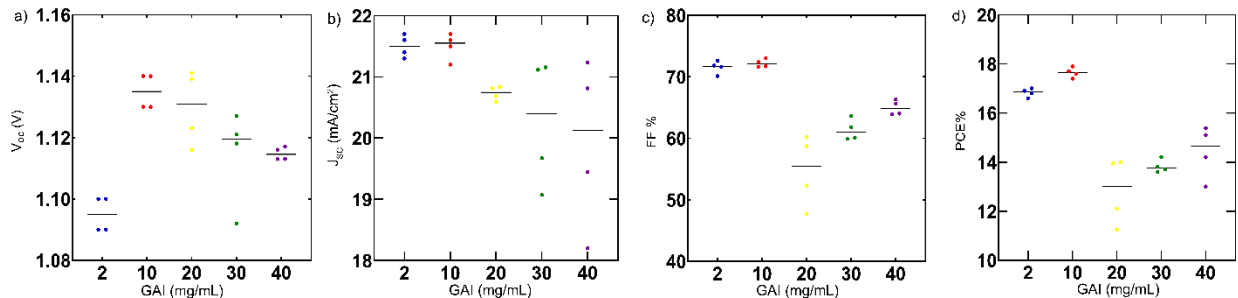


**Figure 45.** Photovoltaic properties of the resulting IPA washed devices: a)  $V_{oc}$ , b)  $J_{sc}$ , c) FF, and d) PCE.

### 6.6. Hydrophobic nature of the perovskite films

Finally, contact-angle measurements were performed to assess the hydrophobic nature of the films upon treatment with GAI (

**Figure 46).** As expected, the GAI-treated samples are less hydrophobic than the control film due to the hydrophilic amine groups of  $GA^+$  that tend to attract water and easily form hydrogen bonds. It is clearly demonstrated that with increasing GAI concentration, the films become more hydrophilic, with GAI-40 showing the lowest contact-angle of 35.6°. The CsMAFA film exhibited the most hydrophobic nature with 72.9°.

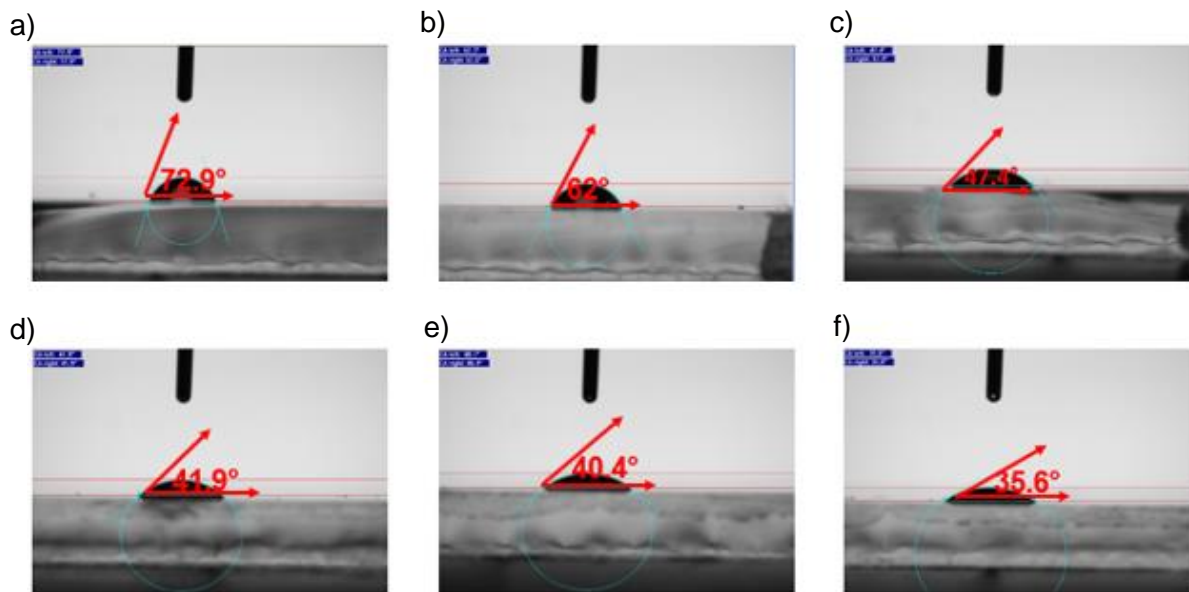


**Figure 46.** Contact-angle measurements for the different perovskite films: a) CsMAFA, b) GAI-2, c) GAI-10, d) GAI-20, e) GAI-30 and f) GAI-40.

## 7. Conclusion and Future Outlook

This study explored the effect of applying different concentrations of GAI as a surface treatment to CsMAFA perovskite film. Low concentrations of GAI lead to excellent optoelectronics properties, enhanced perovskite crystallinity, thereby demonstrating devices with outstanding photovoltaic properties, particularly in  $V_{OC}$  and FF compared to the CsMAFA reference devices. While higher GAI concentrations greater than 10 mg/ml induced additional crystal phases, which are thought to be closely related to  $(FAPbI_3)_x(GA_2PbI_4)_{100-x}$  (for  $x=0$  to 50) in addition to the introduction of excess unreacted GAI which resulted in poor device performance. It is clear that the precise control of interface treatments is vital for optimal structure-properties and device output. In addition, treatment with the optimized GAI-10 solution resolves micro-scale PL inhomogeneities in CsMAFA perovskite films, which could be correlated to the improved device performance and lowered hysteresis at the device level. This validates the general consensus that device performance improves upon homogenization of optoelectronic properties. Consequently, this work opens a new path to investigating the micro-structural degradation pathways of perovskite thin films by targeting the use of controlled passivation treatments and growth strategies for the elimination of optoelectronic-inhomogeneities and thus, pushing the efficiency more towards the theoretical limit. In doing so, the objective would be to reveal the underlying structural defects and chemical phases that are limiting performance and device stability in addition to causing structure-property heterogeneities with a view to engineering halide-perovskite devices that operate efficiently. Further studies targeting the assessment of the device stability are critical for correlating improvements in device performance, photophysical and optoelectronics properties to the operational lifetime of these devices.

## 8. References

1. Parmesan, C. & Yohe, G. A globally coherent fingerprint of climate change impacts across natural systems. *Nature* **421**, 37–42 (2003).
2. Hughes, T. P. *et al.* Climate Change, Human Impacts, and the Resilience of Coral Reefs. *Science* (80-. ). **301**, 929 LP – 933 (2003).
3. Bedford, D. & Cook, J. Agnotology, Scientific Consensus, and the Teaching and Learning of Climate Change: A Response to Legates, Soon and Briggs. *Sci. Educ.* **22**, 2019–2030 (2013).
4. Solomon, S., Plattner, G.-K., Knutti, R. & Friedlingstein, P. Irreversible climate change due to carbon dioxide emissions. *Proc. Natl. Acad. Sci.* **106**, 1704 LP – 1709 (2009).
5. Sandells, M. & Flocco, D. Land ice. in *Introduction to the Physics of the Cryosphere* 4–16 (Morgan & Claypool Publishers, 2014). doi:10.1088/bk978-1-6270-5303-7ch4.
6. Seyboth, K. *et al.* Renewables 2016 global status report. *REN21 Paris, Fr.* (2016).
7. Obama, B. The irreversible momentum of clean energy. *Science* (80-. ). **355**, 126 LP – 129 (2017).
8. Saliba, M. *et al.* Promises and challenges of perovskite solar cells. **744**, 739–744 (2017).
9. Baikie, T. *et al.* Synthesis and crystal chemistry of the hybrid perovskite (CH<sub>3</sub>NH<sub>3</sub>)PbI<sub>3</sub> for solid-state sensitised solar cell applications. *J. Mater. Chem. A* **1**, 5628–5641 (2013).
10. Grätzel, M. The light and shade of perovskite solar cells. *Nat. Mater.* **13**, 838–842 (2014).
11. Bach, U. Perovskite solar cells: Brighter pieces of the puzzle. *Nat. Chem.* **7**, 616–617 (2015).
12. Kojima, A., Teshima, K., Shirai, Y. & Miyasaka, T. Organometal Halide Perovskites as Visible-Light Sensitizers for Photovoltaic Cells. *J. Am. Chem. Soc.* **131**, 6050–6051 (2009).
13. Green, M. A., Ho-Baillie, A. & Snaith, H. J. The emergence of perovskite solar cells. *Nat. Photonics* **8**, 506–514 (2014).
14. best-research-cell-efficiencies.20200104.pdf.
15. Farooq, A. *et al.* Spectral Dependence of Degradation under Ultraviolet Light in Perovskite Solar Cells. *ACS Appl. Mater. Interfaces* **10**, 21985–21990 (2018).
16. Razera, R. A. Z. *et al.* Instability of p–i–n perovskite solar cells under reverse bias. *J. Mater. Chem. A* **8**, 242–250 (2020).
17. Yang, J. *et al.* Oxygen- and Water-Induced Energetics Degradation in Organometal Halide Perovskites. *ACS Appl. Mater. Interfaces* **10**, 16225–16230 (2018).



18. Salado, M. *et al.* Impact of moisture on efficiency-determining electronic processes in perovskite solar cells. *J. Mater. Chem. A* **5**, 10917–10927 (2017).
19. Domanski, K. *et al.* Not All That Glitters Is Gold: Metal-Migration-Induced Degradation in Perovskite Solar Cells. *ACS Nano* **10**, 6306–6314 (2016).
20. Manser, J. S., Saidaminov, M. I., Christians, J. A., Bakr, O. M. & Kamat, P. V. Making and Breaking of Lead Halide Perovskites. *Acc. Chem. Res.* **49**, 330–338 (2016).
21. Stranks, S. D. *et al.* Electron-Hole Diffusion Lengths Exceeding 1 Micrometer in an Organometal Trihalide Perovskite Absorber. *Science (80-. )*. **342**, 341 LP – 344 (2013).
22. Stoumpos, C. C., Malliakas, C. D. & Kanatzidis, M. G. Semiconducting Tin and Lead Iodide Perovskites with Organic Cations: Phase Transitions, High Mobilities, and Near-Infrared Photoluminescent Properties. *Inorg. Chem.* **52**, 9019–9038 (2013).
23. Stranks, S. D. *et al.* Recombination Kinetics in Organic-Inorganic Perovskites: Excitons, Free Charge, and Subgap States. *Phys. Rev. Appl.* **2**, 34007 (2014).
24. Hutter, E. M., Eperon, G. E., Stranks, S. D. & Savenije, T. J. Charge Carriers in Planar and Meso-Structured Organic-Inorganic Perovskites: Mobilities, Lifetimes, and Concentrations of Trap States. *J. Phys. Chem. Lett.* **6**, 3082–3090 (2015).
25. Yamada, Y., Endo, M., Wakamiya, A. & Kanemitsu, Y. Spontaneous Defect Annihilation in CH<sub>3</sub>NH<sub>3</sub>PbI<sub>3</sub> Thin Films at Room Temperature Revealed by Time-Resolved Photoluminescence Spectroscopy. *J. Phys. Chem. Lett.* **6**, 482–486 (2015).
26. Yavari, M. *et al.* How far does the defect tolerance of lead-halide perovskites range? The example of Bi impurities introducing efficient recombination centers. *J. Mater. Chem. A* **7**, 23838–23853 (2019).
27. Mitzi, D. B. Synthesis, Structure, and Properties of Organic-Inorganic Perovskites and Related Materials. in *Progress in Inorganic Chemistry* 1–121 (John Wiley & Sons, Ltd, 2007). doi:10.1002/9780470166499.ch1.
28. Ponseca, C. S. *et al.* Organometal Halide Perovskite Solar Cell Materials Rationalized: Ultrafast Charge Generation, High and Microsecond-Long Balanced Mobilities, and Slow Recombination. *J. Am. Chem. Soc.* **136**, 5189–5192 (2014).
29. Bella, F. *et al.* Improving efficiency and stability of perovskite solar cells with photocurable fluoropolymers. *Science (80-. )*. **354**, 203 LP – 206 (2016).
30. Lee, M. M., Teuscher, J., Miyasaka, T., Murakami, T. N. & Snaith, H. J. Efficient Hybrid Solar Cells Based on Meso-Superstructured Organometal Halide Perovskites. *Science (80-. )*. **338**, 643 LP – 647 (2012).
31. Kim, H.-S. *et al.* Lead Iodide Perovskite Sensitized All-Solid-State Submicron Thin Film Mesoscopic Solar Cell with Efficiency Exceeding 9%. *Sci. Rep.* **2**, 591 (2012).

32. Anaraki, E. H. *et al.* Highly efficient and stable planar perovskite solar cells by solution-processed tin oxide. *Energy Environ. Sci.* **9**, 3128–3134 (2016).
33. Correa Baena, J. P. *et al.* Highly efficient planar perovskite solar cells through band alignment engineering. *Energy Environ. Sci.* **8**, 2928–2934 (2015).
34. Luo, D. *et al.* Enhanced photovoltage for inverted planar heterojunction perovskite solar cells. *Science (80-. )*. **360**, 1442 LP – 1446 (2018).
35. Zheng, X. *et al.* Defect passivation in hybrid perovskite solar cells using quaternary ammonium halide anions and cations. *Nat. Energy* **2**, 17102 (2017).
36. Zheng, X. *et al.* Managing grains and interfaces via ligand anchoring enables 22.3%-efficiency inverted perovskite solar cells. *Nat. Energy* **5**, 131–140 (2020).
37. Cho, H. *et al.* Overcoming the electroluminescence efficiency limitations of perovskite light-emitting diodes. *Science (80-. )*. **350**, 1222 LP – 1225 (2015).
38. Adhikari, N. *et al.* Interfacial Study To Suppress Charge Carrier Recombination for High Efficiency Perovskite Solar Cells. *ACS Appl. Mater. Interfaces* **7**, 26445–26454 (2015).
39. Correa-Baena, J.-P. *et al.* Identifying and suppressing interfacial recombination to achieve high open-circuit voltage in perovskite solar cells. *Energy Environ. Sci.* **10**, 1207–1212 (2017).
40. Castro-Méndez, A.-F., Hidalgo, J. & Correa-Baena, J.-P. The Role of Grain Boundaries in Perovskite Solar Cells. *Adv. Energy Mater.* **9**, 1901489 (2019).
41. Tress, W. Perovskite Solar Cells on the Way to Their Radiative Efficiency Limit – Insights Into a Success Story of High Open-Circuit Voltage and Low Recombination. *Adv. Energy Mater.* **7**, 1602358 (2017).
42. Snaith, H. J. *et al.* Anomalous Hysteresis in Perovskite Solar Cells. *J. Phys. Chem. Lett.* **5**, 1511–1515 (2014).
43. Meloni, S. *et al.* Ionic polarization-induced current–voltage hysteresis in CH<sub>3</sub>NH<sub>3</sub>PbX<sub>3</sub> perovskite solar cells. *Nat. Commun.* **7**, 10334 (2016).
44. Rothmann, M. U., Li, W., Etheridge, J. & Cheng, Y. Microstructural Characterisations of Perovskite Solar Cells – From Grains to Interfaces : Techniques , Features , and Challenges. **1700912**, 1–17 (2017).
45. Beznosikov, B. V & Aleksandrov, K. S. Perovskite-like crystals of the Ruddlesden-Popper series. *Crystallogr. Reports* **45**, 792–798 (2000).
46. Ruddlesden, S. N. & Popper, P. The compound Sr<sub>3</sub>Ti<sub>2</sub>O<sub>7</sub> and its structure. *Acta Crystallogr.* **11**, 54–55 (1958).
47. Cheng, Z. & Lin, J. Layered organic–inorganic hybrid perovskites: structure{,} optical properties{,} film preparation{,} patterning and templating engineering. *CrystEngComm* **12**, 2646–2662 (2010).
48. Krishna, A., Gottis, S., Nazeeruddin, M. K. & Sauvage, F. Mixed Dimensional 2D/3D Hybrid Perovskite Absorbers: The Future of Perovskite Solar Cells? *Adv. Funct. Mater.* **29**, 1806482 (2019).

49. Schileo, G. & Grancini, G. Halide perovskites: current issues and new strategies to push material and device stability. *J. Phys. Energy* **2**, 21005 (2020).
50. Travis, W., Glover, E. N. K., Bronstein, H., Scanlon, D. O. & Palgrave, R. G. On the application of the tolerance factor to inorganic and hybrid halide perovskites: a revised system. *Chem. Sci.* **7**, 4548–4556 (2016).
51. Correa-Baena, J.-P. *et al.* Promises and challenges of perovskite solar cells. *Science* (80-. ). **358**, 739 LP – 744 (2017).
52. Egger, D. A., Rappe, A. M. & Kronik, L. Hybrid Organic–Inorganic Perovskites on the Move. *Acc. Chem. Res.* **49**, 573–581 (2016).
53. Era, M., Morimoto, S., Tsutsui, T. & Saito, S. Organic-inorganic heterostructure electroluminescent device using a layered perovskite semiconductor (C<sub>6</sub>H<sub>5</sub>C<sub>2</sub>H<sub>4</sub>NH<sub>3</sub>)<sub>2</sub>PbI<sub>4</sub>. *Appl. Phys. Lett.* **65**, 676–678 (1994).
54. Hattori, T., Taira, T., Era, M., Tsutsui, T. & Saito, S. Highly efficient electroluminescence from a heterostructure device combined with emissive layered-perovskite and an electron-transporting organic compound. *Chem. Phys. Lett.* **254**, 103–108 (1996).
55. Jagielski, J., Kumar, S., Yu, W.-Y. & Shih, C.-J. Layer-controlled two-dimensional perovskites: synthesis and optoelectronics. *J. Mater. Chem. C* **5**, 5610–5627 (2017).
56. Zhou, N. *et al.* The Spacer Cations Interplay for Efficient and Stable Layered 2D Perovskite Solar Cells. *Adv. Energy Mater.* **10**, 1901566 (2020).
57. Bouduban, M. E. F. *et al.* Crystal Orientation Drives the Interface Physics at Two/Three-Dimensional Hybrid Perovskites. *J. Phys. Chem. Lett.* **10**, 5713–5720 (2019).
58. Koh, T. M. *et al.* Nanostructuring Mixed-Dimensional Perovskites: A Route Toward Tunable, Efficient Photovoltaics. *Adv. Mater.* **28**, 3653–3661 (2016).
59. Smith, I. C., Hoke, E. T., Solis-Ibarra, D., McGehee, M. D. & Karunadasa, H. I. A Layered Hybrid Perovskite Solar-Cell Absorber with Enhanced Moisture Stability. *Angew. Chemie Int. Ed.* **53**, 11232–11235 (2014).
60. Quan, L. N. *et al.* Ligand-Stabilized Reduced-Dimensionality Perovskites. *J. Am. Chem. Soc.* **138**, 2649–2655 (2016).
61. Cao, D. H., Stoumpos, C. C., Farha, O. K., Hupp, J. T. & Kanatzidis, M. G. 2D Homologous Perovskites as Light-Absorbing Materials for Solar Cell Applications. *J. Am. Chem. Soc.* **137**, 7843–7850 (2015).
62. Grancini, G. & Nazeeruddin, M. K. Dimensional tailoring of hybrid perovskites for photovoltaics. *Nat. Rev. Mater.* **4**, 4–22 (2019).
63. Cho, Y. *et al.* Mixed 3D–2D Passivation Treatment for Mixed-Cation Lead Mixed-Halide Perovskite Solar Cells for Higher Efficiency and Better Stability. *Adv. Energy Mater.* **8**, 1–10 (2018).
64. Alanazi, A. Q. *et al.* Atomic-Level Microstructure of Efficient Formamidinium-

- Based Perovskite Solar Cells Stabilized by 5-Ammonium Valeric Acid Iodide Revealed by Multinuclear and Two-Dimensional Solid-State NMR. *J. Am. Chem. Soc.* **141**, 17659–17669 (2019).
65. Wang, Z. *et al.* Efficient ambient-air-stable solar cells with 2D–3D heterostructured butylammonium-caesium-formamidinium lead halide perovskites. *Nat. Energy* **2**, 17135 (2017).
  66. Grancini, G. *et al.* One-Year stable perovskite solar cells by 2D/3D interface engineering. *Nat. Commun.* **8**, 15684 (2017).
  67. Jodlowski, A. D. *et al.* Large guanidinium cation mixed with methylammonium in lead iodide perovskites for 19% efficient solar cells. *Nat. Energy* **2**, 972–979 (2017).
  68. Ma, C. *et al.* 2D/3D perovskite hybrids as moisture-tolerant and efficient light absorbers for solar cells. *Nanoscale* **8**, 18309–18314 (2016).
  69. Lin, Y. *et al.* Enhanced Thermal Stability in Perovskite Solar Cells by Assembling 2D/3D Stacking Structures. *J. Phys. Chem. Lett.* **9**, 654–658 (2018).
  70. Lin, Y. *et al.* Suppressed Ion Migration in Low-Dimensional Perovskites. *ACS Energy Lett.* **2**, 1571–1572 (2017).
  71. Huang, Z. *et al.* Suppressed Ion Migration in Reduced-Dimensional Perovskites Improves Operating Stability. *ACS Energy Lett.* **4**, 1521–1527 (2019).
  72. Li, P. *et al.* Low-Dimensional Perovskites with Diammonium and Monoammonium Alternant Cations for High-Performance Photovoltaics. *Adv. Mater.* **31**, 1901966 (2019).
  73. Zheng, H. *et al.* Self-Additive Low-Dimensional Ruddlesden–Popper Perovskite by the Incorporation of Glycine Hydrochloride for High-Performance and Stable Solar Cells. *Adv. Funct. Mater.* **30**, 2000034 (2020).
  74. Liu, G. *et al.* Interface passivation treatment by halogenated low-dimensional perovskites for high-performance and stable perovskite photovoltaics. *Nano Energy* **73**, 104753 (2020).
  75. Shi, J. *et al.* Fluorinated Low-Dimensional Ruddlesden–Popper Perovskite Solar Cells with over 17% Power Conversion Efficiency and Improved Stability. *Adv. Mater.* **31**, 1901673 (2019).
  76. Chaudhary, B. *et al.* Mixed-Dimensional Naphthylmethylammonium-Methylammonium Lead Iodide Perovskites with Improved Thermal Stability. *Sci. Rep.* **10**, 429 (2020).
  77. Shi, J. *et al.* Fluorinated Low-Dimensional Ruddlesden – Popper Perovskite Solar Cells with over 17 % Power Conversion Efficiency and Improved Stability. **1901673**, 1–10 (2019).
  78. Kim, H. *et al.* Optimal Interfacial Engineering with Different Length of Alkylammonium Halide for Efficient and Stable Perovskite Solar Cells. *Adv. Energy Mater.* **9**, 1902740 (2019).

79. Akin, S. *et al.* New Strategies for Defect Passivation in High-Efficiency Perovskite Solar Cells. *Adv. Energy Mater.* **10**, 1903090 (2020).
80. Alharbi, E. A. *et al.* Perovskite Solar Cells Yielding Reproducible Photovoltage of 1.20 V. *Res. (Washington, D.C.)* **2019**, 8474698 (2019).
81. De Marco, N. *et al.* Guanidinium: A Route to Enhanced Carrier Lifetime and Open-Circuit Voltage in Hybrid Perovskite Solar Cells. *Nano Lett.* **16**, 1009–1016 (2016).
82. Giorgi, G., Fujisawa, J.-I., Segawa, H. & Yamashita, K. Organic–Inorganic Hybrid Lead Iodide Perovskite Featuring Zero Dipole Moment Guanidinium Cations: A Theoretical Analysis. *J. Phys. Chem. C* **119**, 4694–4701 (2015).
83. Zhang, W., Xiong, J., Li, J. & Daoud, W. A. Guanidinium induced phase separated perovskite layer for efficient and highly stable solar cells. *J. Mater. Chem. A* **7**, 9486–9496 (2019).
84. Wu, S. *et al.* Efficient large guanidinium mixed perovskite solar cells with enhanced photovoltage and low energy losses. *Chem. Commun.* **55**, 4315–4318 (2019).
85. Szafranski, M. Investigation of phase instabilities in guanidinium halogenoplumbates(II). *Thermochim. Acta* **307**, 177–183 (1997).
86. Kieslich, G., Sun, S. & Cheetham, A. K. Solid-state principles applied to organic–inorganic perovskites: new tricks for an old dog. *Chem. Sci.* **5**, 4712–4715 (2014).
87. Szafranski, M. & Katrusiak, A. Phase transitions in the layered structure of diguanidinium tetraiodoplumbate. *Phys. Rev. B* **61**, 1026–1035 (2000).
88. Wu, W.-Q. *et al.* Bilateral alkylamine for suppressing charge recombination and improving stability in blade-coated perovskite solar cells. *Sci. Adv.* **5**, (2019).
89. Yang, S. *et al.* Tailoring Passivation Molecular Structures for Extremely Small Open-Circuit Voltage Loss in Perovskite Solar Cells. *J. Am. Chem. Soc.* **141**, 5781–5787 (2019).
90. Chavan, R. D., Prochowicz, D., Tavakoli, M. M., Yadav, P. & Hong, C. K. Surface Treatment of Perovskite Layer with Guanidinium Iodide Leads to Enhanced Moisture Stability and Improved Efficiency of Perovskite Solar Cells. *Adv. Mater. Interfaces* **7**, 2000105 (2020).
91. Jones, T. W. *et al.* Lattice strain causes non-radiative losses in halide perovskites. *Energy Environ. Sci.* **12**, 596–606 (2019).
92. Jeon, N. J. *et al.* Solvent engineering for high-performance inorganic–organic hybrid perovskite solar cells. *Nat. Mater.* **13**, 897–903 (2014).
93. Graydon, O. Guanidinium benefit. *Nat. Photonics* **10**, 145 (2016).
94. Doherty, T. A. S. *et al.* Performance-limiting nanoscale trap clusters at grain junctions in halide perovskites. **580**, (2020).
95. Beckmann, P. A. A review of polytypism in lead iodide. *Cryst. Res. Technol.* **45**, 455–460 (2010).

96. Nazarenko, O. *et al.* Guanidinium-Formamidinium Lead Iodide: A Layered Perovskite-Related Compound with Red Luminescence at Room Temperature. *J. Am. Chem. Soc.* **140**, 3850–3853 (2018).
97. Sutaño, A. A. *et al.* Dynamical evolution of the 2D/3D interface: a hidden driver behind perovskite solar cell instability. *J. Mater. Chem. A* **8**, 2343–2348 (2020).
98. Saliba, M. *et al.* Cesium-containing triple cation perovskite solar cells: improved stability, reproducibility and high efficiency. *Energy Environ. Sci.* **9**, 1989–1997 (2016).
99. Tennyson, E. M., Doherty, T. A. S. & Stranks, S. D. Heterogeneity at multiple length scales in halide perovskite semiconductors. *Nat. Rev. Mater.* **4**, 573–587 (2019).
100. Wu, Z. *et al.* Highly Efficient Perovskite Solar Cells Enabled by Multiple Ligand Passivation. *Adv. Energy Mater.* **10**, 1903696 (2020).
101. deQuilettes, D. W. *et al.* Photo-induced halide redistribution in organic–inorganic perovskite films. *Nat. Commun.* **7**, 11683 (2016).
102. Eperon, G. E. & Ginger, D. S. Perovskite solar cells: Different facets of performance. *Nat. Energy* **1**, 16109 (2016).
103. Thanh, L. C., Depeursinge, C., Levy, F. & Mooser, E. The band gap excitons in PbI<sub>2</sub>. *J. Phys. Chem. Solids* **36**, 699–702 (1975).
104. Zhong, M. *et al.* Large-scale 2D PbI<sub>2</sub> monolayers: experimental realization and their indirect band-gap related properties. *Nanoscale* **9**, 3736–3741 (2017).
105. Tumen-Ulzii, G. *et al.* Detrimental Effect of Unreacted PbI(2) on the Long-Term Stability of Perovskite Solar Cells. *Adv. Mater.* **32**, e1905035 (2020).
106. Grancini, G. *et al.* CH<sub>3</sub>NH<sub>3</sub>PbI<sub>3</sub> perovskite single crystals: surface photophysics and their interaction with the environment. *Chem. Sci.* **6**, 7305–7310 (2015).
107. Huang, J., Shao, Y. & Dong, Q. Organometal Trihalide Perovskite Single Crystals: A Next Wave of Materials for 25% Efficiency Photovoltaics and Applications Beyond? *J. Phys. Chem. Lett.* **6**, 3218–3227 (2015).
108. Gratia, P. *et al.* Intrinsic Halide Segregation at Nanometer Scale Determines the High Efficiency of Mixed Cation/Mixed Halide Perovskite Solar Cells. *J. Am. Chem. Soc.* **138**, 15821–15824 (2016).
109. Knight, A. J. *et al.* Electronic Traps and Phase Segregation in Lead Mixed-Halide Perovskite. *ACS Energy Lett.* **4**, 75–84 (2019).
110. Wolff, C. M., Caprioglio, P., Stolterfoht, M. & Neher, D. Nonradiative Recombination in Perovskite Solar Cells: The Role of Interfaces. *Adv. Mater.* **31**, 1902762 (2019).
111. Stolterfoht, M. *et al.* Visualization and suppression of interfacial recombination for high-efficiency large-area pin perovskite solar cells. *Nat. Energy* **3**, 847–854 (2018).
112. Chen, Q. *et al.* Controllable self-induced passivation of hybrid lead iodide

- perovskites toward high performance solar cells. *Nano Lett.* **14**, 4158–4163 (2014).
113. Dong, Q. *et al.* Solar cells. Electron-hole diffusion lengths > 175  $\mu\text{m}$  in solution-grown  $\text{CH}_3\text{NH}_3\text{PbI}_3$  single crystals. *Science* **347**, 967–970 (2015).
  114. Agiorgousis, M. L., Sun, Y.-Y., Zeng, H. & Zhang, S. Strong Covalency-Induced Recombination Centers in Perovskite Solar Cell Material  $\text{CH}_3\text{NH}_3\text{PbI}_3$ . *J. Am. Chem. Soc.* **136**, 14570–14575 (2014).
  115. Du, T. *et al.* Formation{,} location and beneficial role of  $\text{PbI}_2$  in lead halide perovskite solar cells. *Sustain. Energy Fuels* **1**, 119–126 (2017).
  116. Cacovich, S. *et al.* Unveiling the Chemical Composition of Halide Perovskite Films Using Multivariate Statistical Analyses. *ACS Appl. Energy Mater.* **1**, 7174–7181 (2018).
  117. Tress, W. Hysteresis in J–V Characteristics. in *Hybrid Perovskite Solar Cells* 429–461 (John Wiley & Sons, Ltd, 2021). doi:<https://doi.org/10.1002/9783527825851.ch16>.
  118. Unger, E. L., Czudek, A., Kim, H.-S. & Tress, W. *Current-voltage analysis: lessons learned from hysteresis. Characterization Techniques for Perovskite Solar Cell Materials* (Elsevier Inc., 2020). doi:10.1016/b978-0-12-814727-6.00004-9.
  119. Ecker, B., Egelhaaf, H.-J., Steim, R., Parisi, J. & von Hauff, E. Understanding S-Shaped Current–Voltage Characteristics in Organic Solar Cells Containing a  $\text{TiO}_x$  Interlayer with Impedance Spectroscopy and Equivalent Circuit Analysis. *J. Phys. Chem. C* **116**, 16333–16337 (2012).
  120. Jacobs, D. A. *et al.* Hysteresis phenomena in perovskite solar cells: the many and varied effects of ionic accumulation. *Phys. Chem. Chem. Phys.* **19**, 3094–3103 (2017).